

https://dspace.org/

Slope Failure Prediction at Husab Open Pit Mine in Namibia

Thikusho, Christine Runguro

2023-12

University of the Witwatersrand, Johannesburg

https://hdl.handle.net/10539/38921

Thikusho, Christine Runguro. (2023). Slope Failure Prediction at Husab Open Pit Mine in Namibia. [Master's dissertation, University of the Witwatersrand, Johannesburg]. WIReDSpace. https://hdl.handle.net/10539/38921

Downloaded from a DSpace repository. https://dspace.org/

School of Mining Engineering



UNIVERSITY OF THE
WITWATERSRAND,
JOHANNESBURG

SLOPE FAILURE PREDICTION AT HUSAB OPEN PIT MINE IN NAMIBIA

Christine Runguro Thikusho

A research report submitted to the Faculty of Engineering and the Built Environment, University of the Witwatersrand, Johannesburg, in partial fulfilment of the requirements for the degree of Master of Science in Engineering.

Johannesburg, 2023

DECLARATION

I declare that this report is my own, unaided work. I have read the University Policy on Plagiarism and hereby confirm that no plagiarism exists in this report. I also confirm that there is no copying nor is there any copyright infringement. I willingly submit to any investigation in this regard by the School of Mining Engineering and I undertake to abide by the decision of any such investigation.



17 December 2023

_____ _____

Signature of Candidate Date

In memory of my father

Stefanus Mutjoviri Thikusho

ABSTRACT

The study is focused on Domain D at Husab Mine in Namibia. The purpose of the study was to improve prediction of pending slope failures for planar and wedge configurations. Planar and wedge failures are similar in that little strain is required to initiate failure. Slope monitoring systems such as ground based radars, interferometric synthetic aperture radar and prisms were reviewed from the available literature. The data from the mine's satellite monitoring data and the ground-based radar instruments was analysed. Slope prediction methods were used to back-analyse the failures, to determine if failure prediction times were possible. A case study was incorporated from the neighbouring Rössing Uranium mine, to supplement the data. The data utilised for the study was downloaded from the slope monitoring instruments on the mine i.e., the interferometric synthetic aperture radar, ground-based radar and tension crack data. The following slope failure predictive tools were investigated; the strain deformation approach; the inverse velocity method; the slope gradient method; the acceleration and velocity approach; and Displacement/Time plots. The back-analysis work done proves that the following slope failure predictive methods were able to predict failure at least 3 days before failure: velocity, cumulative displacement and inverse velocity. It appears that the Husab mine failure mechanism is not as brittle as previously assumed and failures are not necessarily instantaneous. Therefore, failures should be identified early, and the necessary risk mitigation measures implemented proactively. The ability of back analysing large volumes of stored data is important in the study of failure prediction.

ACKNOWLEDGMENTS

My research supervisor, Prof. Bryan Watson has been of great help through his guidance and mentorship throughout my studies. I will forever be grateful for his contribution to this work.

I am grateful to Husab Mine's management team, especially the Executive Vice President, Mr. Irvinne Simataa for approving the usage of the mine's data for the research work and granting permission to publish the data. Special thanks to the management of the Mineral Resources Department (Mr Gao Xiang) and the geotechnical team (Grantham Ockhuizen and the entire Geotech team) at the mine for all their effort that have greatly contributed to this work. I will forever be grateful to the mine for their financial contribution towards my studies.

The Neighbouring Rössing Uranium Mine entrusted me with their data to incorporate in this study. I am very much grateful to the Rössing mine team; Ms. Sophy Partenbach - Fick, Ms. Angela Kapapilo, Ms. Idalina Garoes and Ms. Petra Husland for facilitating the process.

Special thanks to my family (my mother, brothers and their spouses) for their unwavering support throughout my studies.

TABLE OF CONTENTS

DECLARATION i

ABSTRACT iii

ACKNOWLEDGMENTS iv

LIST OF FIGURES viii

LIST OF TABLES xiii

APPENDIX LIST OF TABLES xiii

LIST OF EQUATIONS xiii

LIST OF ABBREVIATIONS AND SYMBOLS xiv

1 INTRODUCTION 1

1.1 Introduction 1

1.2 Purpose of the Study 2

1.3 Research Background and Context 5

1.3.1 Findings of feasibility analysis 5

1.3.2 SRK Consulting 2018 7

1.3.3 Subsequent in-house geotechnical findings 8

1.4 Location of the Study Area 11

1.5 Regional and Local Geological Setting 13

1.6 Justification for Research 14

1.7 Problem Statement 15

1.8 Research Methods 15

1.9 Sources of Data 15

1.10 Structure of the Research Report 16

2 LITERATURE REVIEW 17

2.1 Introduction 17

2.2 Slope Configuration in Open Pit Mines 18
2.3 Contributing Factors to Open Pit Instability 19
2.4 Slope Failure Mechanisms 20
2.4.1 Plane failure 21
2.4.2 Wedge failure 23
2.4.3 Toppling failure 25
2.4.4 Summary 29
2.5 Slope Monitoring Methods 30
2.5.1 Visual inspections 30
2.5.2 Photogrammetry 30
2.5.3 Extensometers and inclinometers 31
2.5.4 Laser scanning (LiDAR) 32
2.5.5 InSAR 32
2.5.6 Robotic total stations: prism monitoring 33
2.5.7 Slope stability radars (SSR) 33
2.6 Methods to Predict Slope Failure 39
2.6.1 Introduction 39
2.6.2 Strain deformation approach to failure prediction 41
2.6.3 Inverse velocity method 45
2.6.4 Slope gradient method (SGM) 47
2.6.5 Acceleration and velocity approach 49
2.6.6 Displacement vs. time plots 50
2.7 Rock Mass Classification Systems 51
2.8 RQD 52
2.8.1 RMR – Bieniawski 1976 52
2.9 Chapter Summary 54
3 METHODOLOGY 56

3.1 Introduction 56
3.2 Data Collection 56
3.3 Data Analysis 57
3.4 Chapter Summary 57
4 ANALYSIS AND RESULTS 59
4.1 Introduction 59
4.1.1 Case study 1: 5 August 2018 failure 63
4.1.2 Case study 2: 30 November 2020 failure 77
4.1.3 Case study 3: 20 August 2021 failure 85
4.1.4 Case study 4: Rössing uranium mine 91
4.2 Chapter Summary 98
4.2.1 Case study 1: August 2018 failure 98
4.2.2 Case study 2: November 2020 failure 99
4.2.3 Case study 3: August 2021 failure 99
4.2.4 Case study 4: Rössing uranium mine 99
4.3 Discussion 100
5 CONCLUSIONS AND RECOMMENDATIONS 102
5.1 Introduction 102
5.2 Research Contributions 102
5.3 Research Limitations 103
5.3.1 Case study 1: 5 October 2018 failure 103
5.3.2 Case study 2: 30 November 2020 failure 103
5.3.3 Case study 3: August 2021 failure 103
5.3.4 Recommendations for future research work 103
REFERENCE LIST 104

LIST OF FIGURES

Figure 1-1: Structural Geotechnical Domains A – E of the Zone 1 pit..... 3

Figure 1-2: DJI Mavic Air 2 drone image of the Domain D slope, photograph taken on-site in August 2021 4

Figure 1-3: Probabilistic planar failure analysis 6

Figure 1-4: Probabilistic wedge failure analysis 7

Figure 1-5: Bench-scale failures that have occurred in Domain D between 2018 and 2020 9

Figure 1-6: Slope design changes Zone 1 Domain D, from 2017 to 2020 10

Figure 1-7: Locality of Husab Mine in relation to the neighbouring Rössing Mine 12

Figure 1-8: Regional setting of the Damara Orogenic Belt 13

Figure 2-1: A Schematic diagram of elements that make up a pit slope geometry 19

Figure 2-2: Schematic diagram of plane failure 22

Figure 2-3: Kinematic conditions for plane failure mode 23

Figure 2-4: Schematic diagram of wedge failure 24

Figure 2-5: Kinematic conditions for wedge failure mode 25

Figure 2-6: Schematic diagram of standard toppling failure 26

Figure 2-7: Flexural toppling failure 27

Figure 2-8: Blocky - flexural toppling failure 27

Figure 2-9: Kinematic conditions for flexural toppling failure 28

Figure 2-10: Reutech MSR series RAR radar, photograph taken at Husab Mine (Namibia) 36

Figure 2-11: IBIS-ArcSAR radar deployed in an open pit operation, photograph taken at Husab mine (Namibia) 38

Figure 2-12: Strain versus time behaviour of rock 40

Figure 2-13: Displacement versus Time schematic diagram for all stages of a moving slope 42

Figure 2-14: Schematic diagram of displacement time curve for pit slope failures 43

Figure 2-15: Highwall Strain % vs. Rock Mass Quality as a useful tool for slope failure prediction and highwall performance analysis 45

Figure 2-16: Inverse velocity versus time plot 46

Figure 2-17: A conceptual model representing predicted life expectancy as a function of time 48

Figure 2-18: Relationship between acceleration and velocity 50

Figure 2-19: Deformation vs. Time curve used for failure analysis prediction 51

Figure 4-1: Geological Cross-section across Geotechnical Domain 59

Figure 4-2: A photogrammetric 3D model created in Agisoft Metashape software, images taken with the DJI Mavic Air 2 Drone onsite 61

Figure 4-3: August 2021 failure taken with the DJI Mavic Air 2 Drone 62

Figure 4-4: Scanline mapping data of discontinuities mapped across the Domain D area, discontinuities are represented as discs 66

Figure 4-5: Kinematic analysis of discontinuities that contributed to the wedge failure 67

Figure 4-6: Kinematic analysis of discontinuities that contributed to planar sliding 68

Figure 4-7: Swedge analysis carried out in Rocscience Swedge software, FOS is 0.772 70

Figure 4-8: An example of metal pins installed in the ground for tension crack monitoring at the Husab Mine's Zone 2 pit-perimeter..... 72

Figure 4-9: Tension Crack measurements taken along Bench 7 crest, measurements taken between 11 July 2018 and 1 August 2018 73

Figure 4-10: Case Study 1 High Wall Strain vs. RMR plot for the Husab Mine data 76

Figure 4-11: Reutech Ground-based RAR, monitoring Geotechnical Domain D (Zone 1 Husab Mine)..... 78

Figure 4-12: Case Study 2 High Wall Strain vs. RMR plot for the Husab Mine data 80

Figure 4-13: Cumulative Displacement vs. Days before failure – November 2020 failure 81

Figure 4-14: Velocity Delta vs. Time – November 2020 Failure..... 83

Figure 4-15: Inverse velocity vs. Time - November 2020 failure..... 84

Figure 4-16: InSAR Cumulative displacement over the time period – August 2020 to August 2021 86

Figure 4-17: InSAR Average Velocity data before failure time – data from the time Period August 2020 to August 2021 87

Figure 4-18: InSAR Inverse velocity data for the Time period – August 2020 to August 2021 88

Figure 4-19: InSAR (Husab Mine Baseline Data - supported by SkyGeo). The horizontal deformation data was taken at the position of the black dot in the highlighted triangle..... 89

Figure 4-20: Case Study 3 High Wall Strain vs. RMR plot for the Husab Mine data 90

Figure 4-21: Failure in the Rössing Uranium Mine Open Pit – 31 July 2020..... 92

Figure 4-22: Cumulative Displacement data from 19 July 2018 to 19 July 2020 (Rössing Uranium Mine) 93

Figure 4-23: Case Study 3 High Wall Strain vs. RMR plot for the Rössing Mine data 94

Figure 4-24: Velocity data from 19 July 2018 to 19 July 2020 (Rössing Uranium Mine) 95

Figure 4-25: Inverse velocity data from 19 July 2018 to 19 July 2020 (Rössing Uranium Mine) 96

Figure 4-26: Slope gradient method applied to prism monitoring data from the Rössing Uranium Mine 97

Figure 4-27: Strain versus Time graph behaviour of rock, the November 2020 failure, Rössing mine failure and August 2018 failure are plotted based on their strain values at failure 101

LIST OF TABLES

Table 1-1: Surface deformation monitoring equipment utilised in open pit mines . 2

Table 1-2: Stratigraphy of the DOB 14

Table 2-1: Summary of conditions for Plane, wedge and Flexural topping failure mechanisms 29

Table 2-2: Summary of RAR and SAR 34

Table 2-3: Threshold strain levels for key stages of high wall stability 44

Table 2-4: Rock Mass Classes 53

Table 4-1: RMR analysis 63

Table 4-2: Strain (%) calculated for Cracks 1A and 2B, with the highest deformation 74

Table 4-3: Strain (%) calculated for the November 2020 failure 79

Table 4-4: Strain (%) calculated for the August 2021 failure 90

Table 4-5: Strain (%) calculated for the Rössing Uranium Mine failure (July 2020) 94

APPENDIX LIST OF TABLES

Appendix A: Scanline Mapping Data 114

Appendix B: Shear Box Test Results 115

Appendix C: Fresh Rock Geotechnical Parameters Part A 116

Appendix D: Fresh Rock Geotechnical Parameters Part B 117

Appendix E: 2017 study and Feasibility UCS lab test results (SRK Part A) 118

Appendix F: 2017 study and Feasibility UCS lab test results (SRK Part B) 119

Appendix G: 2017 study and Feasibility UCS lab test results (SRK Part C) 120

Appendix H: InSAR Monitoring Data (November 2020 Failure) 121

LIST OF EQUATIONS

Equation 2-1 44

Equation 2-2 46

Equation 2-3 49

Equation 2-4 49

Equation 2-5 52

Equation 2-6 52

Equation 2-7 53

LIST OF ABBREVIATIONS AND SYMBOLS

Abbreviation	Description
C	Cohesion
BSA	Bench Stack Angle
DOB	Damara Orogenic Belt
FOG	Fall of Ground
FOS	Factor of Safety
GBInSAR	Ground-Based Interferometric Synthetic Aperture Radar
GBSAR	Ground-Based Synthetic Aperture Radar
GCP	Ground Control Points
IDS	Ingegneria Dei Sistemi
InSAR	Interferometric Synthetic Aperture Radar
IRA	Inter Ramp Angle
LiDAR	Light Detection and Ranging
Ma	Mega annum (one million years)
MRMR	Mining Rock Mass Rating
MPa	Mega Pascal
MSR	Movement and Surveying Radar
OSA	Overall Slope Angle
RAR	Real Aperture Radar
RMR	Rock Mass Rating
RQD	Rock Quality Designation
SAR	Synthetic Aperture Radar
SBW	Spill Berm Width
SFM	Structure from Motion
SGM	Slope Gradient Method
SSR	Slope Stability Radar
TF	Failure Time
TFP	Predicted Failure Time
TLS	Terrestrial Laser Scanners
TOF	Time of Failure
UCS	Uniaxial Compressive Strength
VCP	Velocity Calculation Period
2D	Two Dimensional
3D	Three Dimensional

Symbol	Description
cm	Centimetre
du/dt	Displacement Rate
km	Kilometer
kPa	Kilo Pascal
m	Meter
m^3	Cubic Meter
mm	Millimeter
m/s^2	Meters Per Second Square
t	Time
ϕ	Friction Angle

1 INTRODUCTION

1.1 Introduction

Safe mining practice is necessary for the protection of mine employees from potential slope failure hazards, and it has financial benefits. Mine slopes are designed with higher levels of risk compared to permanent slopes in civil projects (Dick, 2013). Inherent geotechnical risks caused by geomechanical properties of the rock mass, slope geometries, geology, seismicity and structures should be managed. Slope deformation monitoring has become an essential part of managing such slope hazards (Dick, 2013).

Geotechnical engineers on open-pit mines analyse slope deformation data and slope failure prediction analyses to improve safety and optimise profitability. Such analyses allow for optimisation of slopes and thus improve production schedules and ore recovery (Dick, 2013).

Various types of slope monitoring equipment are utilised for background monitoring and critical monitoring. Background monitoring involves an overall assessment of the status of slope stability on a mine. Monitoring is assessed by establishing long term movement trends and slope movement direction (Dick, 2013). Areas identified as high risk through background monitoring, require critical monitoring (active). The purpose is to alert mine personnel of impending slope failures in real time (Little, 2005). Examples of background monitoring instrumentation are satellite radars (Interferometric Synthetic Aperture Radars - InSAR), laser and prism monitoring. Radars ground-based Real Aperture Radars (RAR) and Ground-based Synthetic Aperture Radars (SAR) are suitable for critical slope deformation monitoring. Considering the potential consequence of instabilities to mining operations, critical monitoring instrumentation requires higher precision and faster measurement updates (Dick, 2013). Monitoring instrumentation is grouped into two groups based on their wall coverage of the slope monitored; (1) point based and (2) area based. Table 1-1 provides

a summary of the common deformation monitoring equipment utilised in open pit mines.

Table 1-1: Surface deformation monitoring equipment utilised in open pit mines (Modified from Dick, 2013)

Instrument/Method	Wall Coverage		Monitoring Method	
	Point	Area	Background	Active
Visual Inspections		X		X
Photogrammetry		✕	✕	
Extensometers and Inclinometers	✕			✕
Laser scanning (LiDAR)	✕		✕	
Satellite InSAR		✕	✕	
Total Station: Prisms	✕		✕	
Ground based radar		✕		✕

1.2 Purpose of the Study

The study focuses on the Zone 1 pit of the Husab Mine (Figure 1-1), situated in Namibia. The pit is subdivided into five structural geotechnical domains (locally named as Domains A, B, C, D and E).

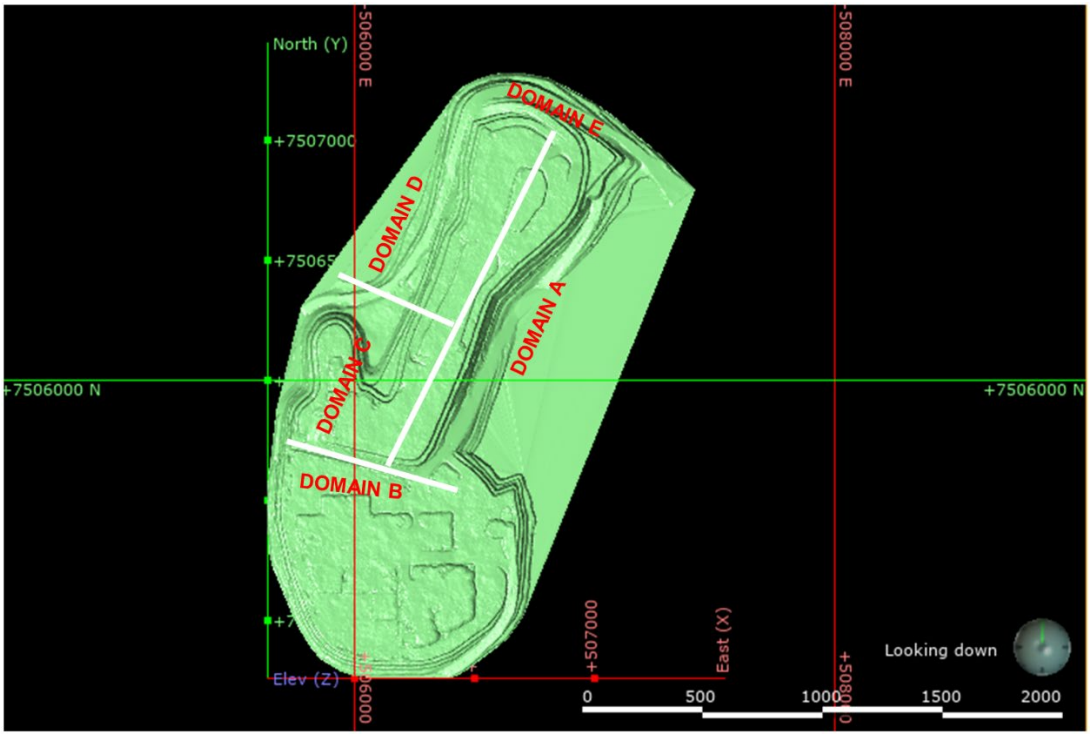


Figure 1-1: Structural Geotechnical Domains A – E of the Zone 1 pit

The structural domains were defined by SRK Consulting in 2018, based on a study of structural defect analysis derived from historic televiewer logs. Foliation data from exploration drill holes and scanline mapping data of exposed bench faces was collected by on-site geotechnical geologists. Domain D shown in Figure 1 - 1, which lies within the Rossing Formation, is the focus for this study, as there have been recurring bench-scale failures since 2018. The unfavourable orientation of foliation planes that are shallow to moderately dipping in this Domain, relative to the wall orientation, is a cause of concern and has contributed to planar and wedge failures. Figure 1 - 2 shows a drone flight image of Domain D slope indicating the locations of various bench-scale failures of August 2018, November 2020 and August 2021.

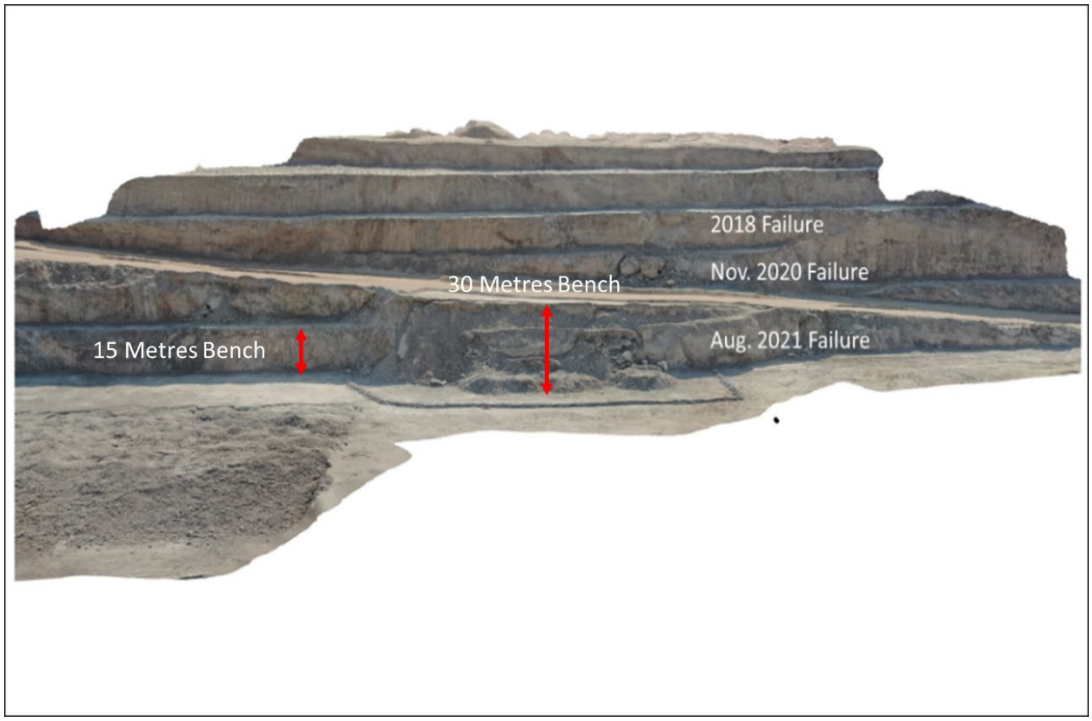


Figure 1-2: DJI Mavic Air 2 drone image of the Domain D slope, photograph taken on-site in August 2021

Due to these recurring bench-scale failures in Domain D, the mine has implemented slope monitoring systems, for early identification of areas of instability. This research work aims to contribute knowledge towards timeously predicting planar and wedge failures at Husab Mine.

The research work will involve the review of previous studies carried out (technical reports) and the utilisation of the mine's existing slope monitoring data to understand the deformation of the rock mass. In addition, the work will involve back analysis of previous slope failures that have occurred. A case study is incorporated from a neighbouring mine in a similar geological setting (Rössing Uranium Mine).

1.3 Research Background and Context

1.3.1 Findings of feasibility analysis

A high likelihood of planar and wedge failure for Slope Sector H (current Domain D) was determined by Golder Associates Africa (2010) during the feasibility stage for the Husab Project. The risk was defined by a 113° wall orientation or azimuth. All stability analyses were carried out in SLIDE 2, a Rocscience 2D limit equilibrium, slope stability software program (Rocscience, 2018). Stability analysis results were verified in Phase2, a finite element program (Rocscience, 2010) (Golder Associates Africa, 2010).

Figure 1- 3 and Figure 1- 4 show the probabilistic analysis for the various slope sectors in Zone 1, carried out by Golder Associates Africa (2010). Based on their analysis, planar and wedge failure was expected for bench faces with a dip angle greater than 80°.

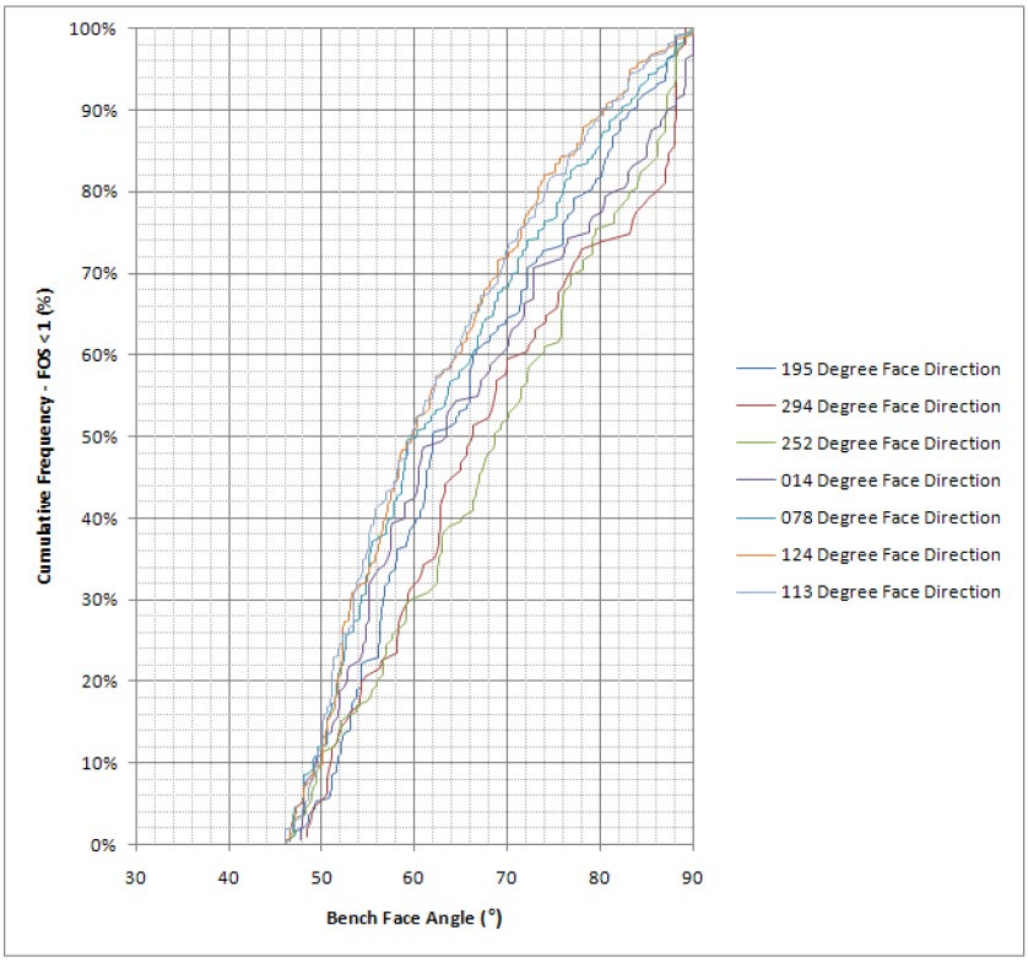


Figure 1-3: Probabilistic planar failure analysis (Golder Associates Africa, 2010)

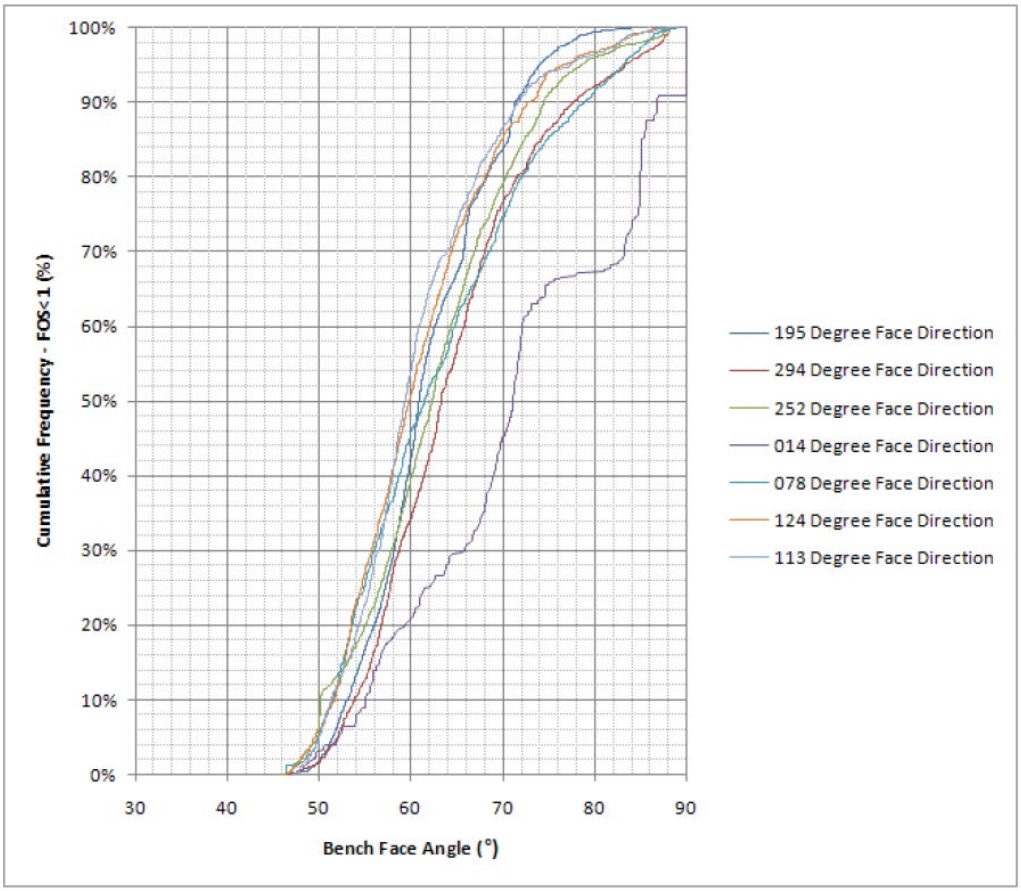


Figure 1-4: Probabilistic wedge failure analysis (Golder Associates Africa, 2010)

1.3.2 SRK Consulting 2018

Following the work carried out by Golder Associates Africa (2010) a geotechnical drilling programme was carried out in 2016 and 2017, under the management of SRK consulting. The aim of the exercise was to fill in the gaps from a previous drilling campaign. A geotechnical design review report was provided to Husab Mine in 2018 (Armstrong and Maduray, 2018). The stability analysis work carried out by SRK Consulting found the following:

- Planar failure is anticipated in Domain D for foliation dip angles greater than 32°; and

- Unstable wedges are expected to form for bench face angles greater than 60° and inter-ramp dip angles greater than 45° (Armstrong and Maduray, 2018).

1.3.3 Subsequent in-house geotechnical findings

Three significant bench-scale failures have occurred in Domain D to date. Kinematic analysis and limit equilibrium work carried out on these failures support the findings by Golder Associates Africa (2010) and SRK Consulting (Armstrong and Maduray, 2018). Site geotechnical geologists carry out scanline mapping of exposed bench faces for kinematic analysis each time a new face is exposed. Major structural features are modelled for stability and assessments of their influence on benches are made. Figure 1 - 5 shows bench-scale planar and wedge failures that have occurred in Domain D between 2018 and 2020, hence the subsequent pit slope design changes. Figure 1 - 6 shows a summary of slope design changes that were implemented from 2017 to 2020.



Figure 1-5: Bench-scale failures that have occurred in Domain D between 2018 and 2020 (Ockhuizen, 2020)

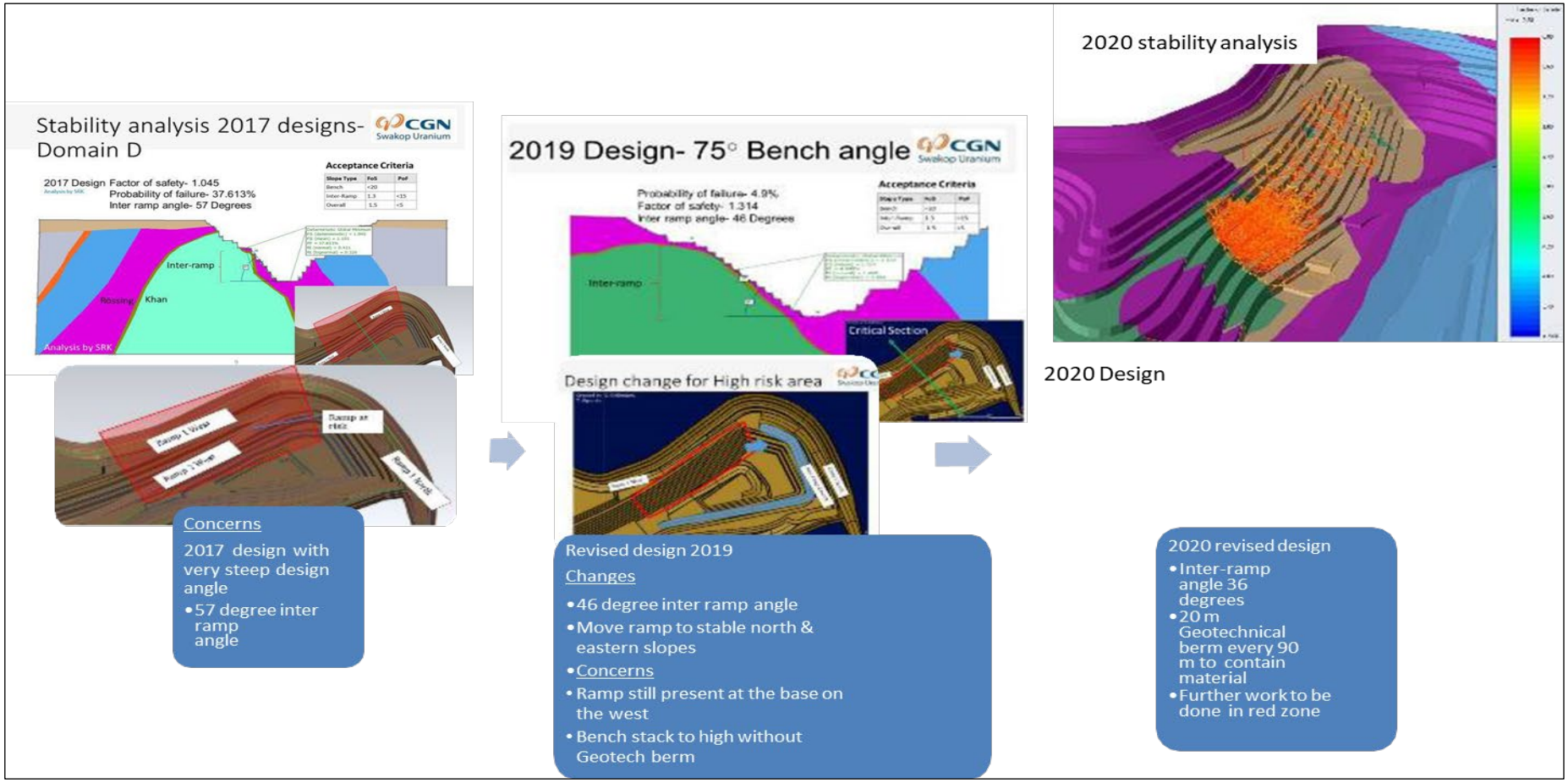


Figure 1-6: Slope design changes Zone 1 Domain D, from 2017 to 2020 (Ockhuizen, 2020)

From the work conducted on-site, the following conclusions have been drawn:

- Unfavourable geological features (foliation planes and major fault structures) have been mapped and are anticipated to continue to pit bottom. Hence, increasing the likelihood of bench-scale failures;
- Bench-scale failures, predominantly wedge and planar failures are predicted for Domain D, which agrees with the findings by Golder Associates Africa (2010) and SRK Consulting (Armstrong and Maduray, 2018); and
- Mining to foliation planes or dip slope mining is an option to reduce bench-scale failures.

1.4 Location of the Study Area

The Husab Mine is situated in Namibia in the Namib Desert, within the northern part of the Namib Naukluft National Park. The mine is located approximately 60 km northeast of the town of Swakopmund and 5 km south of the Rössing Uranium Mine (Inwood et al, 2011). Figure 1 - 7 shows the locality of the Husab Mine in relation to the neighbouring Rössing Uranium Mine.



Figure 1-7: Locality of Husab Mine in relation to the neighbouring Rössing Mine (Google Earth, 2023)

1.5 Regional and Local Geological Setting

The Damara Orogenic Belt (DOB) is a major Pan African mobile belt, comprising of Mesoproterozoic to earliest Palaeozoic rocks (Inwood et al, 2011). The orogenic belt extends from the Namibian coast towards the northeast, into Botswana and Zambia as shown in Figure 1 - 8.

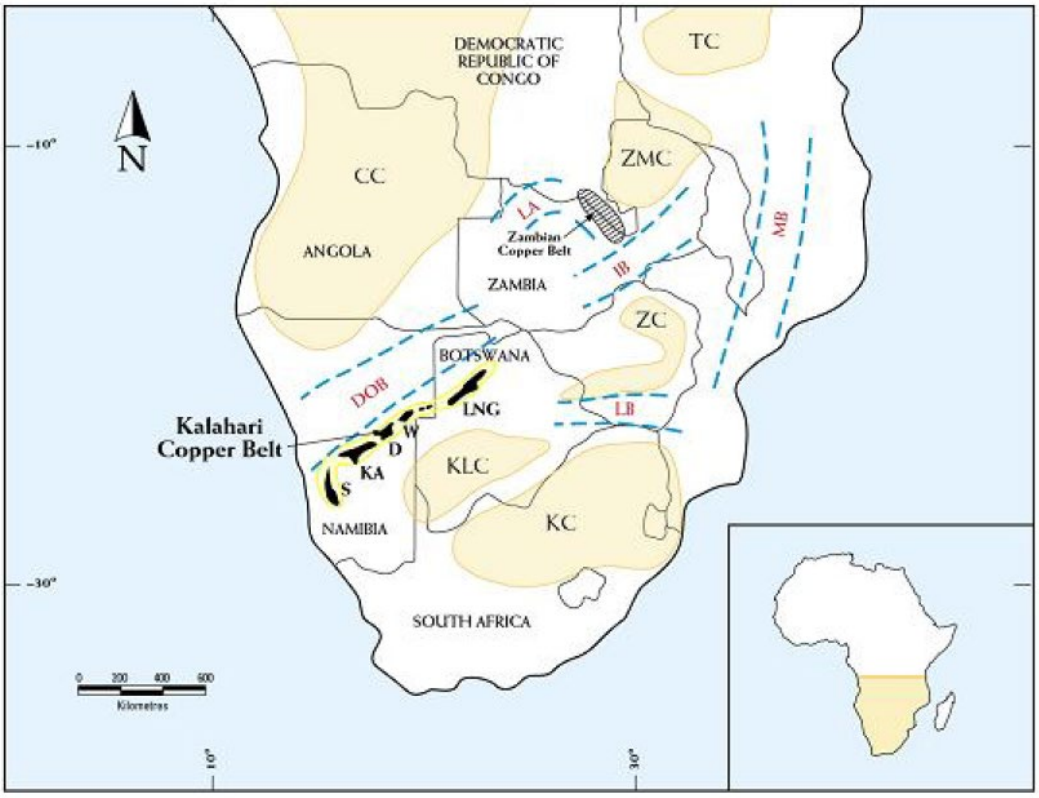


Figure 1-8: Regional setting of the Damara Orogenic Belt (Inwood et al, 2011)

The orogeny was initiated due to rifting between the Kaapvaal and Congo Cratons between 1000 Mega annum (Ma) and 900 Ma and ended at approximately 500 Ma during a period of major thrust faulting and granitoid intrusion. The Husab Mine lies within the Central Zone of the DOB, where mineralisation within the belt is structurally controlled and is associated with intrusions. The orogenic belt is comprised of three successions: the Nossib

Group, Lower Swakop Group and Upper Swakop Group (Inwood et al, 2011). Table 1 - 2 shows the stratigraphic column of the DOB.

Table 1-2: Stratigraphy of the DOB (Modified from Inwood et al., 2011)

Group	Sub-Group	Formation	Thickness	Lithology
Swakop	Khomas	Kuiseb	>3000	Pelitic and semi-pelitic schist and gneiss, migmatite, calc-silicate rock, quartzite. Thinkas-member: Pelitic and semi-pelitic schist, calc-silicate rock, marble and para-amphibolite.
		Karibib	1000	Marble, calc-silicate, pelitic and semi-pelitic schist and gneiss, biotite amphibolite schist, migmatite.
		Chuos	700	Diamictite, calc-silicate rock, pebbly schist, quartzite, ferruginous quartzite, migmatite.
	Discordance			
	Ugab	Rössing	200	Marble, pelitic schist and gneiss, biotite-hornblende and schist, migmatite, calc-silicate rock, quartzite, metaconglomerate.
	Discordance			
Nosib		Khan	1100	Migmatite, banded and mottled quartzo-feldspathic clinopyroxene-amphibolite gneiss, migmatite, pyroxene garnet gneiss, amphibolite, quartzite, metaconglomerate.
		Etusis	3000	Quartzite, metaconglomerate, pelitic and semi-pelitic schist and gneiss, migmatite, quartzofeldspathic clinopyroxene-amphibolite gneiss, calc-silicate rock, metaphyolite.

1.6 Justification for Research

Reviews on slope monitoring deformation data and monitoring equipment have not been made in Geotechnical Domain D. Restriction of personnel and equipment entrance to the pit after a blast is based on failure analyses carried out by site geotechnical geologists and the restriction hours are excessive.

Shorter entrance times after a blast will improve production. This research will analyse the instrumentation data to provide improved warning times of pending failures.

1.7 Problem Statement

Husab mine's geotechnical geologists rely on slope monitoring tools to guide mining operations. This practice has worked in safely guiding mining activities, thereby preventing injuries to personnel. However, the slope re-entrance times after blasting are conservative. In some instances, waiting periods have exceeded a shift (equivalent to 12 hours). During these times, site geotechnical geologists restrict access to areas of concern, hence, impacting production in the process. This research work aims to analyse the instrumentation data with the intent of providing improved warning time of pending failures.

1.8 Research Methods

The following methods were employed to analyse the monitored data:

- Strain Deformation approach (Brox & Newcomen, 2004);
- Inverse Velocity method (Rose & Hungr, 2007);
- Velocity approach (Federico et al., 2012);
- Slope Gradient Method (Mufundirwa et al., 2010); and
- Displacement vs. Time plots (Newcomen & Dick, 2016).

1.9 Sources of Data

The research report is based on slope monitoring data from the Husab Mine site (Geotechnical Domain D). In addition, a case study of a slope failure that occurred on the neighbouring Rössing Uranium mine is included to assess the validity of the various slope failure prediction methods. The following instruments were used in the assessments: tension crack meters, prism monitoring data

(Rössing Uranium Mine), ground based radar data (Reutech radar) and InSAR (satellite monitoring data).

1.10 Structure of the Research Report

The report is structured as follows:

- Chapter 1 outlines the purpose of the study and background;
- Chapter 2 provides a review of slope monitoring instruments employed at the mine, such as radars, prisms and InSAR, description of failure mechanisms and the causes of slope failures;
- Chapter 3 describes the methodology used to collect data. The data analysis method is also included in the chapter;
- Chapter 4 provides the results from the slope monitoring systems and interpretation of the results; and
- Chapter 5 provides the final conclusions and recommendations.

2 LITERATURE REVIEW

2.1 Introduction

Chapter 2 provides an overview of terms and naming conventions on the mine. The causes of slope failures in open pit mines are discussed and slope failure mechanisms are reviewed.

A review of current slope monitoring methods is provided:

- Visual inspections;
- Photogrammetry;
- Extensometers;
- Laser Scanning;
- InSAR;
- Prism Monitoring; and
- Ground-based RAR and the Ground-based Synthetic Aperture Radar (GBSAR).
- Slope failure predictive methods are reviewed.
- Strain Deformation Approach;
- Inverse Velocity;
- Slope Gradient Method (SGM);
- Velocity versus Time plots; and
- Displacement versus Time plots.

Finally, Rock Mass Classification Systems are reviewed:

- The Rock Quality Designation (RQD) developed by Deere in 1964; and
- The Bieniawski Rock Mass Rating System (RMR) developed by Bieniawski in 1976;

2.2 Slope Configuration in Open Pit Mines

Slope geometry in open pit mines is governed by the following factors:

- Rock mass quality;
- Rock mass strength;
- Size and shape of the orebody;
- Structural complexity (major faults, thrusts and shears); and
- Rock fabric (bedding and foliation planes) and equipment capabilities (Gibson et al., 2006).

Figure 2 - 1 provides a description of the terms and naming conventions used on the mine. In the figure, IRA refers to the Inter Ramp Angle measured from toe to toe, BSA refers to the Bench Stack Angle, measured from toe to the crest. OSA refers to the Overall Slope Angle. SBW refers to the spill berm width (Gibson et al., 2006).

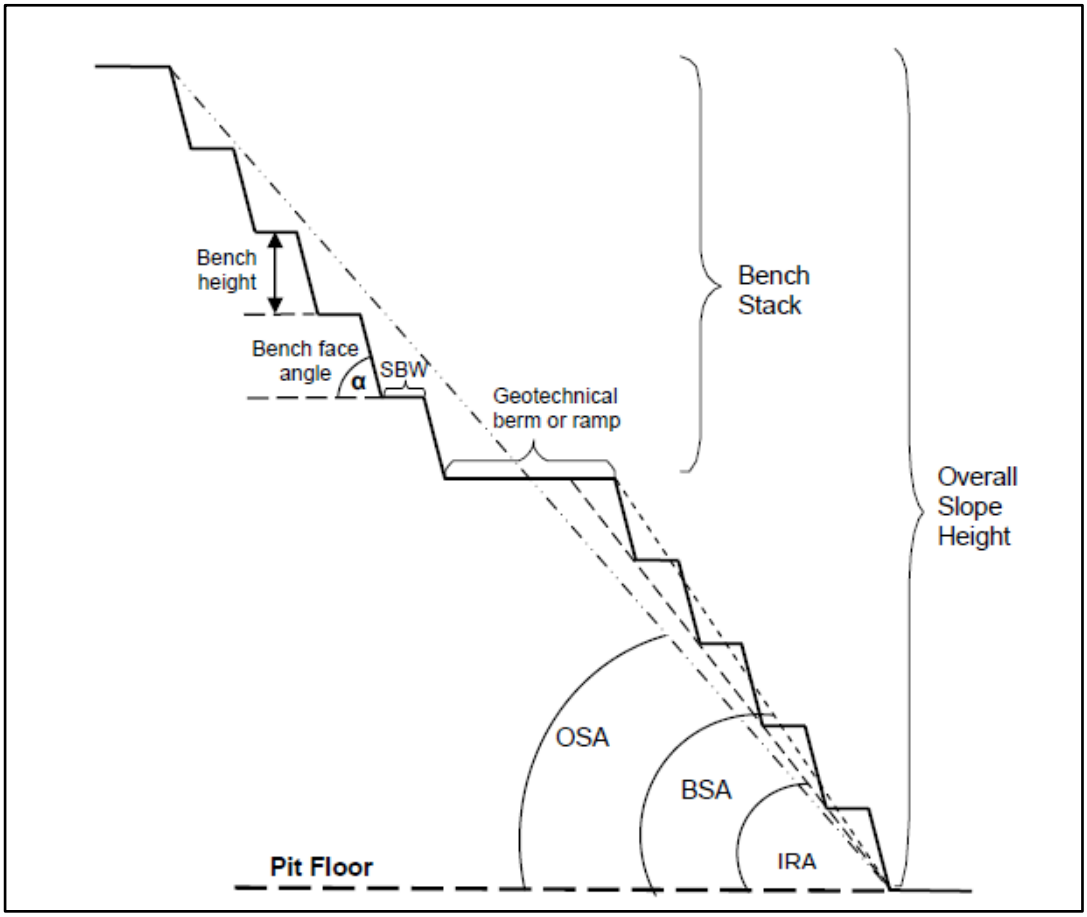


Figure 2-1: A Schematic diagram of elements that make up a pit slope geometry (Gibson et al., 2006)

2.3 Contributing Factors to Open Pit Instability

Mining induced stresses caused by excavation result in relaxation of the rock mass around the pit walls and increased stresses at the bottom of the pit. Such relaxation may cause the cohesion on discontinuity surfaces to be damaged or destroyed. Other factors such as the rock mass structures and their persistence, rock mass quality and strength, blasting practices, seismicity and the effect of ground water are all important factors contributing to slope failures (Gibson et al., 2006).

2.4 Slope Failure Mechanisms

Slope stability is an important aspect in open pit mining. It refers to any ground movement that could have devastating effects on people's lives or infrastructure (Kardani et al., 2021). Mining activities result in stress and strain changes in the rock mass surrounding the excavation. When the deformation exceeds critical limits, controlled by the rock strength, rock instability occurs (Kayesa, 2005).

The following factors are important in pit slope stability; geometry of the slope (high wall angle, overall pit depth and shape of the wall) concave or convex, rock mass quality (strength of the rock mass, structure and deformability), rock type and dynamic loading (Raghuvanshi, 2019).

Mining large volumes of rock during a mining cycle causes rapid unloading of the rock mass and stress relaxation. The extent of the relaxation is dependent on the rock mass quality. In addition to the above listed parameters, the following factors contribute to slope stability; nature and orientation of the rock mass jointing, the level of ground water pressure in the slope and blasting practices (Brox and Newcomen, 2004). The most common failure mechanisms are; plane, wedge and toppling failure.

Kinematic analysis is used to identify the likelihood of failure mechanism in a slope sector. The analysis is based on the following input parameters; (1) frictional shear strength along the discontinuity faces, (2) orientation of discontinuities and (3) slope geometry. The analysis method works by plotting the failure mechanisms of discontinuities on stereographic plots. Cohesion as an input parameter is not taken into account in the analysis method. The method is useful for assessing plane failure, wedge failure, circular failure and flexural toppling and block toppling (Farina et al., 2020). The descriptions of failure mechanisms that occur in hard rock conditions is provided below.

2.4.1 Plane failure

Plane failure mode is one of the most common failure mechanisms, predominantly occurring in sedimentary and meta-sedimentary rocks. Plane failure mode occurs when a major structural discontinuity daylights in an excavation or pit. The following conditions must be met for plane failure to occur (Raghuvanshi, 2019):

- The angle of the structural discontinuity must be less than the angle of the slope;
- The angle of the structural discontinuity must be greater than the friction angle of the discontinuity surface,
- The strike of the major discontinuity must be parallel to the slope face;
- The rock mass prone to sliding must be defined by release surfaces on either side or located on a convex slope; and
- A tension crack must be present at the upper portion of the slope.

Internal factors based on slope geometry that are drivers in slope stability are as follows;

- Inclination of the slope;
- Inclination of the upper slope face;
- Slope height;
- Azimuth and dip-angle of the failure plane;
- Tension cracks; and
- Well defined release surfaces on either side of the rock mass if the pit wall is not convex (Raghuvanshi, 2019).

Figure 2 - 2 shows a schematic diagram of plane failure. As described in the sections above, the sliding block is daylighting toward the excavation, therefore increasing the likelihood of sliding along the failure plane.

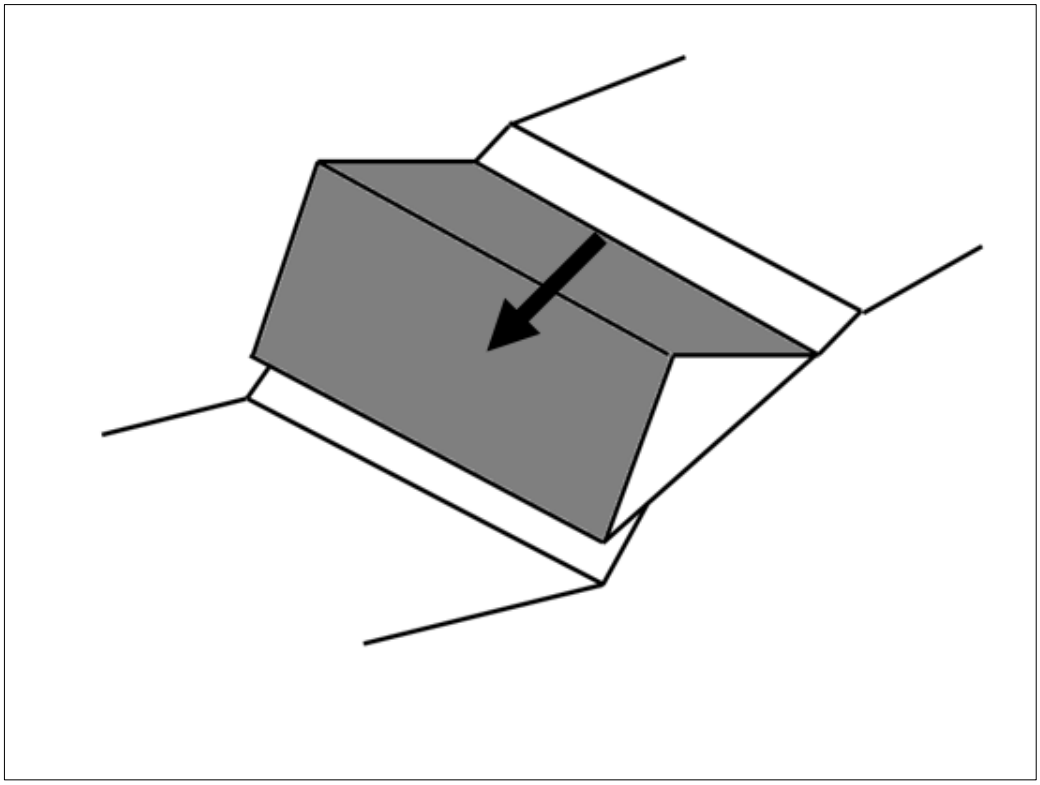


Figure 2-2: Schematic diagram of plane failure (Modified from Kolapo et al., 2022)

Figure 2 - 3 shows the kinematic conditions required for a planar failure to occur. The stereographic plot shows an area that has a high chance of planar sliding as the strike of the plane of weakness is within +/- 20° of the crest of the slope (Kolapo et al., 2022). The shear strength parameters of the discontinuity surfaces i.e. cohesion (C) and angle friction (φ) are resisting stress factors governing planar failure. The characteristics of discontinuities such as continuity of a failure surface, roughness along the failure surface and aperture are key contributing factors for planar failure mechanism (Raghuvanshi, 2019).

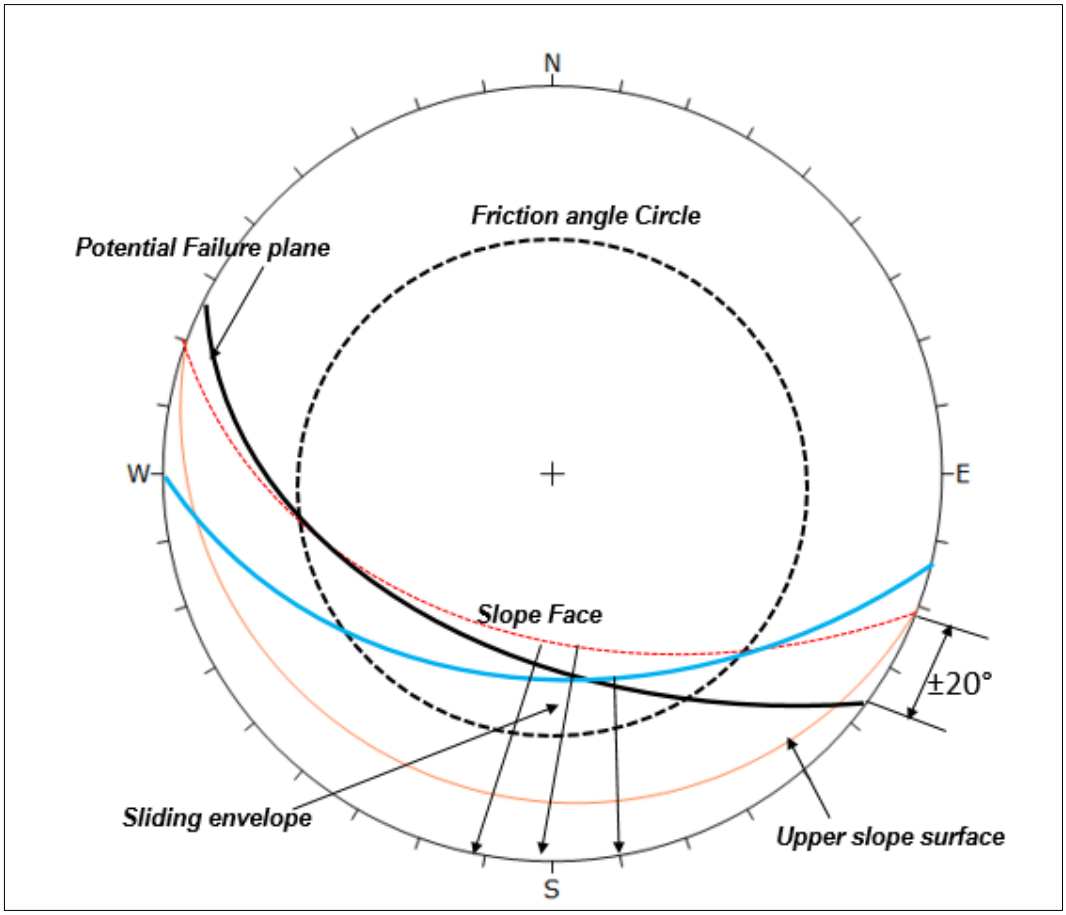


Figure 2-3: Kinematic conditions for plane failure mode (Modified from Raghuvanshi, 2019)

2.4.2 Wedge failure

Similar to planar failure, wedge failure is a common slope failure mechanism in pit slopes (Johari and Lari, 2016). Wedge failure mechanism involve tetrahedral – shaped blocks sliding on more than one discontinuity plane (Smith, 2016). The following kinematic conditions should be met for a wedge failure to occur (Park and West, 2001);

- The trend of the line of intersection should be parallel to the dip-direction of the slope face;
- The plunge of the line of intersection should be less than the dip of the slope face; and
- The angle of friction of the discontinuity surface should be less than the plunge of the line of intersection.

A schematic diagram for a potential unstable wedge is shown in Figure 2 - 4. The unstable block is defined on either side by discontinuities, therefore forming tetrahedral shaped blocks.

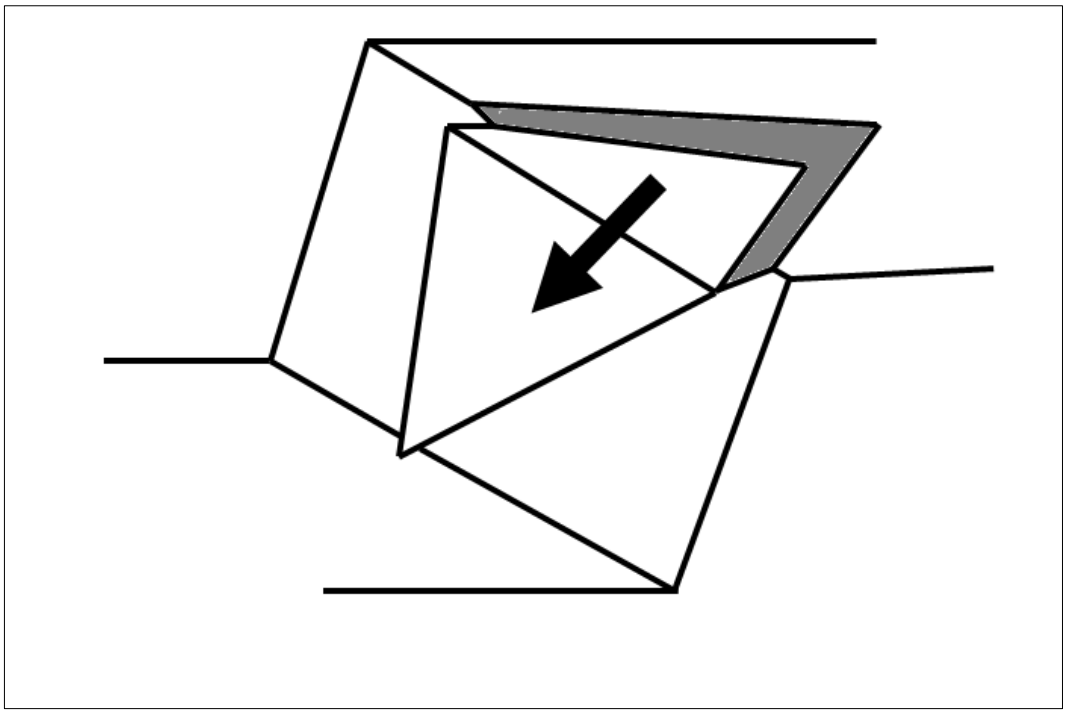


Figure 2-4: Schematic diagram of wedge failure (Modified from Kolapo et al., 2022)

Kinematic conditions for wedge failure in a rock mass slope are shown in Figure 2 - 5. The stereographic projection method is the most common method used to

identify potential wedge failure mechanism. The stereographic plot shows 5 potential intersections of discontinuities within the failure envelope that could potentially fail. Another method used for analysing wedge failure mechanism is Factor of Safety (FOS) through limit equilibrium analysis. A slope is considered stable if it has a FOS of greater than 2 (Park and West, 2001).

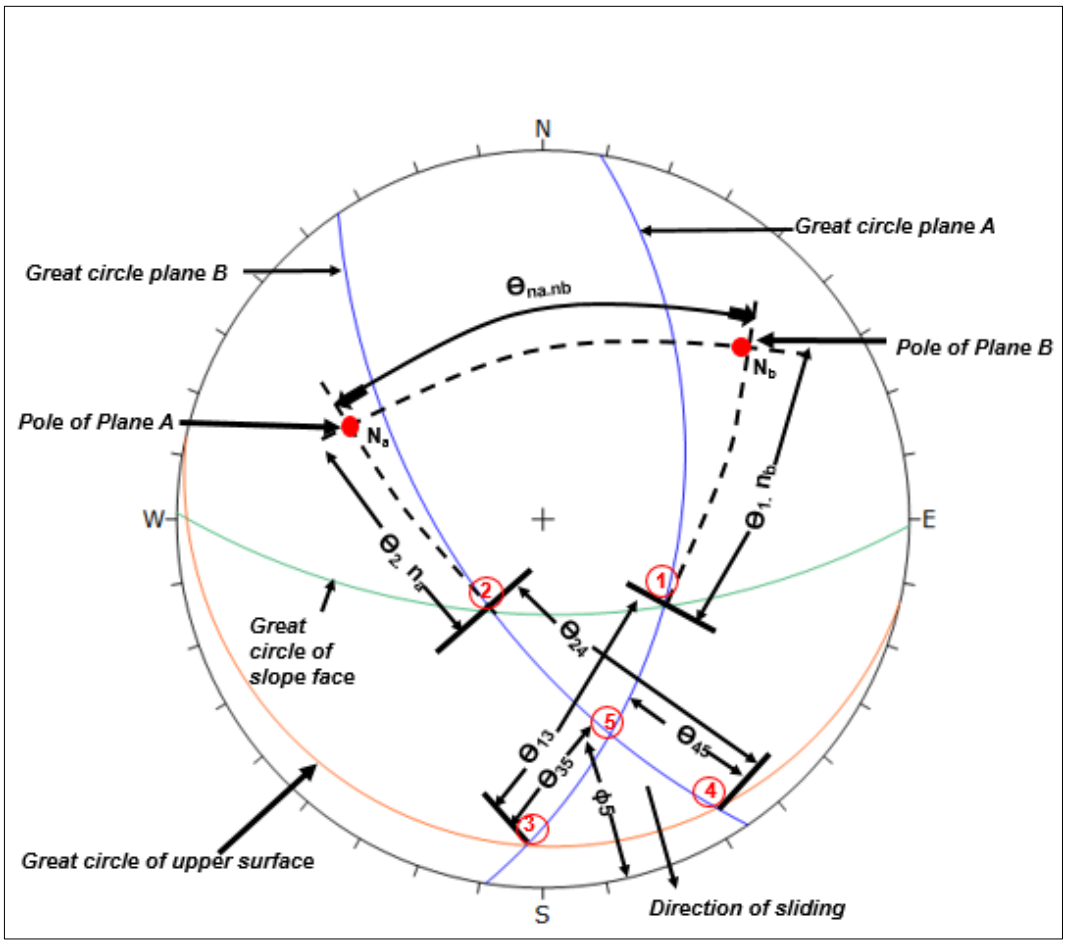


Figure 2-5: Kinematic conditions for wedge failure mode (Modified from Park and West, 2001)

2.4.3 Toppling failure

Toppling failure involves the rotation of rock columns or blocks of rock about a fixed axis. Two toppling failure mechanisms can occur:

- standard toppling; and
- flexural toppling.

If a block or blocks prone to toppling are detached from the rock mass, this phenomenon is referred to as standard toppling (Gui et al., 2023). If the blocks prone to topple are not detached from the rock mass, the failure mechanism is referred to as flexural toppling (Gui et al., 2023). In addition, flexural toppling occurs when the tensile stress in the rock mass exceeds the tensile strength of the rock units (Mohtarami et al., 2014).

The condition for toppling failure involves a set of steeply dipping discontinuities that form parallel or almost parallel to the slope (Mohtarami et al., 2014). A schematic diagram of toppling failure in rock masses is shown Figure 2 - 6. Figure 2 - 7 and Figure 2 - 8 show flexural toppling and blocky – flexural toppling failure. Figure 2-9 provides a representation of a stereographic plot showing the unstable area within the failure envelope (Lateral limits of +/- 20°).

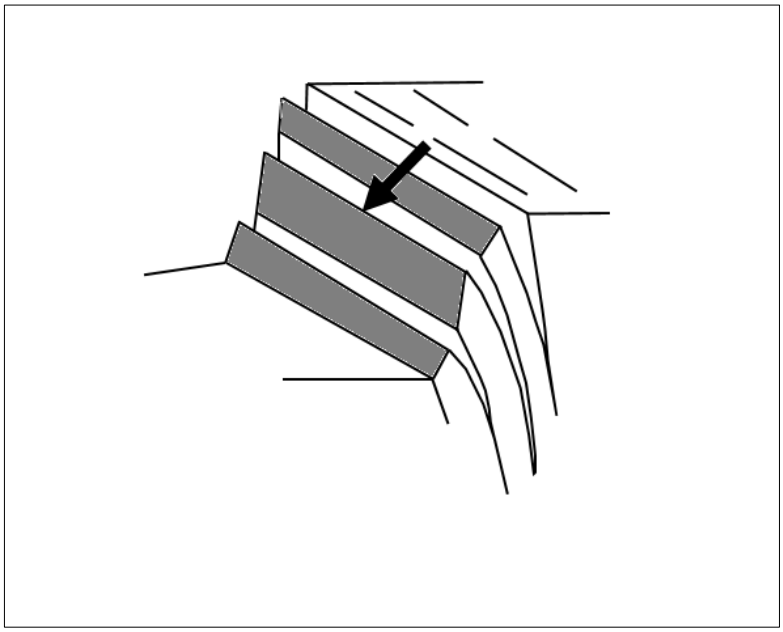


Figure 2-6: Schematic diagram of standard toppling failure (Modified from Gottlander, 2019)

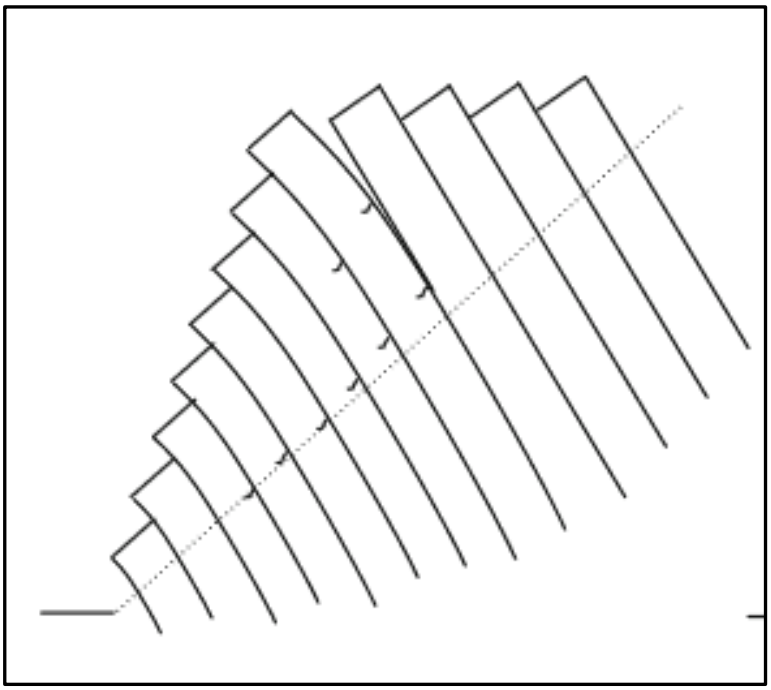


Figure 2-7: Flexural toppling failure (Adapted from Amini et al., 2012)

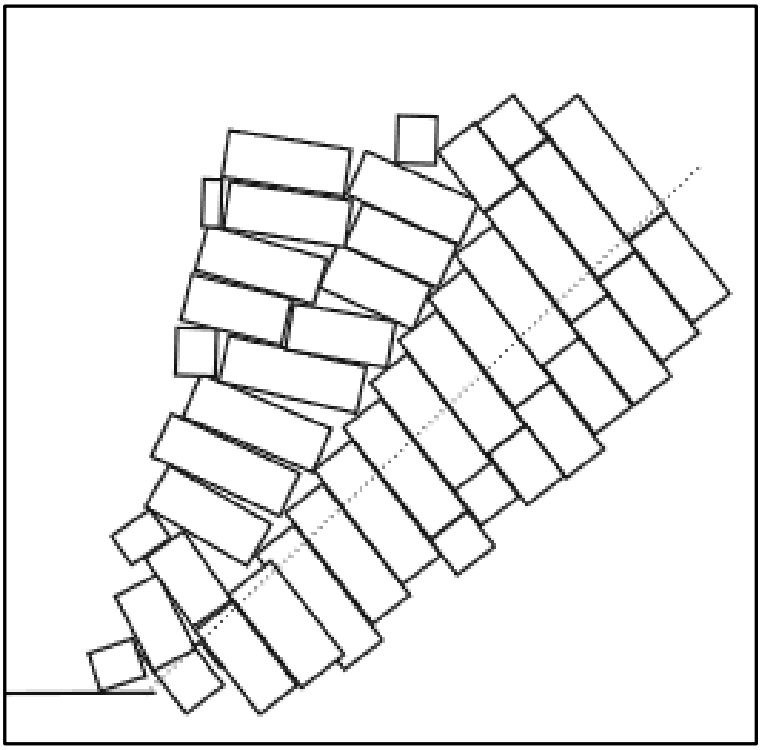


Figure 2-8: Blocky - flexural toppling failure (Adapted from Amini et al., 2012)

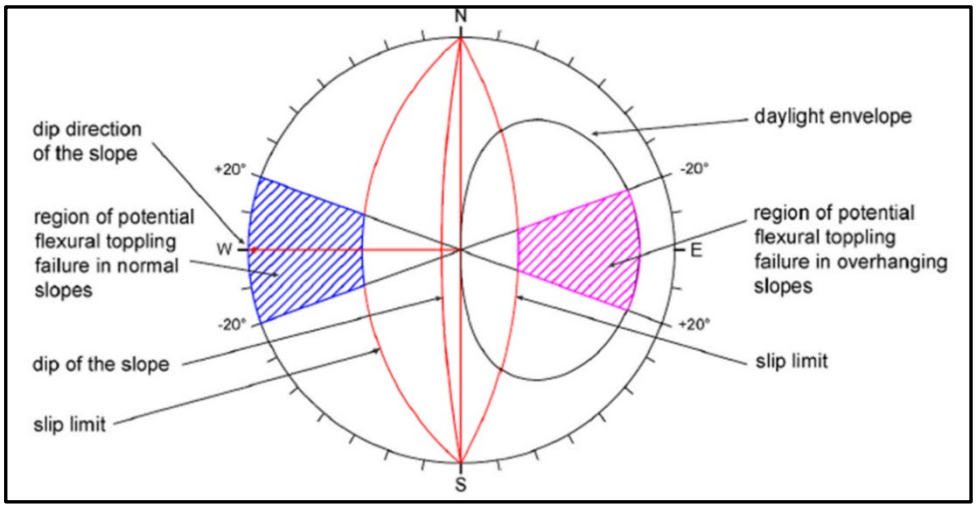


Figure 2-9: Kinematic conditions for flexural toppling failure (Adapted from Gigli et al., 2022)

2.4.4 Summary

A summary of all three common failure mechanisms in rock slopes i.e. planar, wedge and toppling is provided in Table 2 - 1. The discontinuities should be parallel to the slope orientation (within 10°).

Table 2-1: Summary of conditions for Plane, wedge and Flexural topping failure mechanisms (Modified from Farina et al., 2020)

Failure Mechanism	Condition for kinematic failure	
Planar Failure	$\alpha_d = \alpha_S \pm 20°$, where: α_d = Dip-direction of the discontinuity plane, α_s = Dip-direction of the bench face.	$\Phi < \beta_d < \beta_s$, Where Φ is friction angle, β_d is the dip of the discontinuity plane and β_s is the dip of the bench-face.
Wedge Failure	**Wedge on both planes:** If the dip-direction of the two planes lie outside the included angle between α_i* and α_s**. **Wedge on only one plane:** If the dip-direction of the one plane lies within the included angle between α_i* and α_s**, the wedge will slide on only that plane. Where α_i* is the dip-direction of the intersection and α_s** is the dip-direction of the bench face.	$\Phi < \beta_i < \beta_s$,
Flexural Toppling	$\alpha_d = \alpha_S \pm 10°$,	$(90° - \beta_s) + \Phi < \beta_d$;

2.5 Slope Monitoring Methods

Slope monitoring is a critical part of risk management in mining operations. The implementation of robust slope monitoring systems, enables geotechnical engineers to assess slope design performance, therefore making necessary slope design modifications, for slope optimisation. Slope monitoring programs are designed for the following purpose:

- Increase safety on operations, therefore minimising injuries to personnel and minimising damage to mining assets;
- Early identification of areas of instability, to allow for proactive implementation of remedial plans to minimise business risk; and
- Providing valuable geotechnical information, which can be used for slope design modification (Read and Stacey, 2009).

Slope monitoring methods employed in mining operations are discussed in the following sections.

2.5.1 Visual inspections

Visual inspections are an important component of slope monitoring. The process of conducting comprehensive visual inspections should involve field supervisors and all personnel working in proximity to high walls. Field personnel are required to report all geotechnical hazards to geotechnical engineers on site. Geotechnical staff are then required to carry out detailed inspections. The cracking of rock along pit crests should be marked on plans and physically in the field. Cracks give valuable information on the failure mechanisms and movement direction (Read and Stacey, 2009).

2.5.2 Photogrammetry

Digital photogrammetry is used in the application of determining 3-dimensional (3D) location of objects from two – dimensional (2D) images (Ortega et al., 2013). The technology greatly increases the turn-around time of geotechnical measurements. Modern technology is able to produce 3D photogrammetric

models, with high quality data that can be used to produce structural models for pit slope design (Read and Stacey, 2009).

Traditionally, structural data was collected manually with hand held compasses through scanline and window mapping techniques or walk-over surveys, however these techniques are labour intensive, requiring extensive field work, producing limited volumes of data. There are limitations to this approach in that certain areas may be inaccessible and there are safety concerns for field staff (Dey et al., 2021).

Walk-over surveys generally produce limited structural data and the data may have orientation bias. Limited dataset acquired through walk-over surveys may be inadequate for statistical evaluation of structural fabric, required for creation of structural models. However, these surveys provide a wealth of information on joint surfaces, which is not always possible from photogrammetry methods. Drone flights are an alternative, quick and reliable tool used in open pit mines to collect large volumes of structural data on multi-benches (Dey et al., 2021).

Three-dimensional overlapping images are subjected to an automated feature matching algorithm in software packages such as Metashape and Structure-From-Motion (SFM). The drone camera position, orientation of the camera and scene geometry are reconstructed simultaneously by automatically matching features in successive photographs. The output from the processed 2D images is a dense point cloud, digital elevation model and 3D photogrammetry-based model. Ground Control Points (GCP) of the area photographed are taken to re-orientate the model in a known coordinate system (Dey et al., 2021).

2.5.3 Extensometers and inclinometers

Extensometers form part of subsurface monitoring methods. They are usually installed in drill holes to measure rockmass deformation. Movement rates are measured along the axis of the borehole. The extensometers are installed with an anchored rod, where a measuring device is provided at the hole collar (Read and Stacey, 2009).

Inclinometers are a form of subsurface rockmass deformation monitoring method, measuring movement in directions perpendicular to the hole. There are two types of inclinometers; (1) portable probe and (2) and inclinometers that consist of more than one probe (Read and Stacey, 2009).

2.5.4 Laser scanning (LiDAR)

Light detection and ranging (LiDAR) use the application of terrestrial Laser scanning (TLS) typically for scanning of topography of inaccessible slopes, pit slope failures, waste dumps and stockpiles. Accuracies can be achieved up to a centimeter scale, with ranges of up to 6 kilometers, however the scan accuracy decreases with increasing distance. Due to the lower accuracy of the technology system compared to radars, it is not suitable for real time monitoring of critical slopes (Read and Stacey, 2009).

2.5.5 InSAR

InSAR emits radar waves from orbiting satellites to the earth to map ground deformation. The radar wave is then scattered back from the earth to the satellite. The technique works by comparing radar images taken at two different time frames, from similar positions in space and comparing their distance to the satellite (USGS, 2022).

Advanced technologies of satellite InSAR has increased monitoring frequency recently to six days, hence, better reliability in predicting slope failure in open pit mines. The ability of satellite systems to be able to monitor displacements above pit crests is a huge advantage to this type of technology. Integrating ground-based radars and satellite InSAR could be complementary in the early detection of slope failures (Carlá et al., 2018). The greatest advantage to this technology is its wide coverage and the ability to detect and measure previous deformation, which is not the case with terrestrial radars. In addition, the technology can monitor inaccessible areas where no monitoring exists such dumps, stockpiles, tailings and leach pads, making this technology a critical need in management of risks in mining operations (Taylor et al., 2016).

2.5.6 Robotic total stations: prism monitoring

Robotic prism monitoring provides important slope information. Prisms are generally installed on highwalls at regular spacings, and the frequency of measurements is determined by on-site geotechnical engineers. Prism monitoring is used for long term trend stability to identify areas where failure is most likely to occur. The requirement for instability prediction is the installation of critical slope monitoring tools and frequent high wall inspections by geotechnical staff on mines (Little, 2005).

2.5.7 Slope stability radars (SSR)

RAR and SAR

SSR have become very useful in detecting and measuring rock surface movement, thereby warning mining personnel timeously of impending slope failures. The ability to monitor pit slopes with sub-millimeter precision, makes the technology an attractive option in managing geotechnical risks. In recent years, various mining operations have implemented SSR as a hazard management plan, in mitigating slope failure risks (Shellam and Coggan, 2020).

New technologies associated with SSR allow for a wide coverage of slopes, and high precision slope monitoring data, hence, improving the understanding of geomechanics of slope deformation. SSR provides technical staff on mines with real-time, accurate and reliable deformation data that improves the understanding of failure mechanisms (Harries and Pritchett, 2009).

Terrestrial radars are widely preferred as slope monitoring tools in open pit mines because of the following functions:

- Ability to monitor deformation in specific areas; and
- Ability to measure areas of slope instability from a long distance (Zhou et al, 2020).

Terrestrial radars are subdivided into two categories (Zhou et al., 2020):

- RAR; and
- SAR.

Table 2 - 2 shows a summary of the main differences between RAR and SAR.

Table 2-2: Summary of RAR and SAR (Modified from Farina et al., 2009)

RAR e.g. Reutech Dish Radars	**SAR e.g. IDS radars**
The first type of slope monitoring system introduced on the market. Dish antenna radars. Operating range varying from 60 m to 4000 m.	Newly developed advanced radars, based on a small horn antenna. Therefore producing a wider beam for scanning.
A radar beam is illuminated over a small footprint area.	Higher spatial resolution longer scanning ranges (5000 m) and faster acquisition time.
Resolution at 1km distance is 8 m X 8 m.	Resolution at 1 km is 0.5 m X 4.3 m.
Submillimeter measurement accuracy approx 0.1 mm	Accuracy of 0.1 – 0.2 mm within 1 Km of the radar from the slope and accuracy of less than 1 mm, when the radar is stationed within 2-4km from the slope.

RAR: the reutech movement and surveying radar (MSR) series

RAR technology has gained popularity in the field of slope monitoring (Zhou et al., 2020). RAR works by transmitting high-frequency electromagnetic waves to the target position and recording the reflected electromagnetic waves from that position. In general, RAR has the following measurement parameters: measurement accuracy of 0.1 mm, monitoring distance of up to 4000 m, horizontal scanning range of 210° and a vertical scanning range of 90 m (Zhou et al., 2020).

Terrestrial radars are among the recent cutting edge technology for accurately predicting of slope failure (Carlá et al., 2018). However, these systems have their limitation in that unexpected failure may happen if deformation occurs above the pit, where there is poor monitoring coverage because of line-of-sight limitations. In such cases, mining operations could benefit greatly through applications of satellite InSAR technologies (Carlá et al., 2018).

The quality of the SSR deformation data is highly dependent on the following factors; sampling frequency, line-of-sight sensitivity and velocity calculation period (VCP) (Shellam and Coggan, 2020). The sampling frequency is a measure of the time it takes for the SSR to scan a slope and acquire data. Therefore, if the sampling frequency is longer than the acceleration of a moving target, failures may not be detected. This is characteristic of wedge and planar failures in brittle rock mass (Shellam and Coggan, 2020).

Line of sight from the SSR to the target slope determines the area and magnitude of the failure recorded by the system. For good quality data, it is critical that the SSR is positioned perpendicular to the slope (Shellam and Coggan, 2020).

VCP is a method used to calculate the rate of deformation, in the event of a failure; 1 hour, 5 hours and 24 hours - time window periods are generally used to determine velocity. Practitioners are cautioned against using shorter time

periods, as they introduce instantaneous velocity and noise, leading to frequent radar alarms. The usage of longer time periods is recommended, as it provides clean data for assessing deformation over a longer time period (Shellam and Coggan, 2020). Figure 2 -10 shows a RAR in use at Husab mine in Namibia.



Figure 2-10: Reutech MSR series RAR radar, photograph taken at Husab Mine (Namibia)

SAR

SAR technology initially introduced in the late 1980s has gained popularity over the years and has become very useful technology in monitoring mines and their surrounding areas. The high precision of the data increases confidence in the safety of mining excavations, therefore maximising production. There are two types of SAR systems; Ground – Based Synthentic Aperture Radars (GBInSAR) and the InSARs (Henschel et al., 2014).

GBInSAR

GBInSAR are used as cutting edge technology in landslides and open pit mines for critical monitoring purposes. GBInSAR radar systems are used to study rock mass deformation data, therefore adding significant value in operational safety and optimising production. The implementation of GBInSAR technology in open pit mines has the following advantages:

- Early detection of ground deformation, which allows for early prediction of failures;
- High measurement accuracy (0.1 mm); and
- Fast data acquisition of up to 40 seconds with a 360° scan and 20 seconds with a 180° scan (Leoni et al., 2015).

An example of the GBInSAR is the IDS (Ingegneria Dei Sistemi) IBIS system developed in 1980 (IDS GeoRadar, 2022). Figure 2 - 11 shows an example of an IDS GBInSAR radar utilised at Husab mine in Namibia.

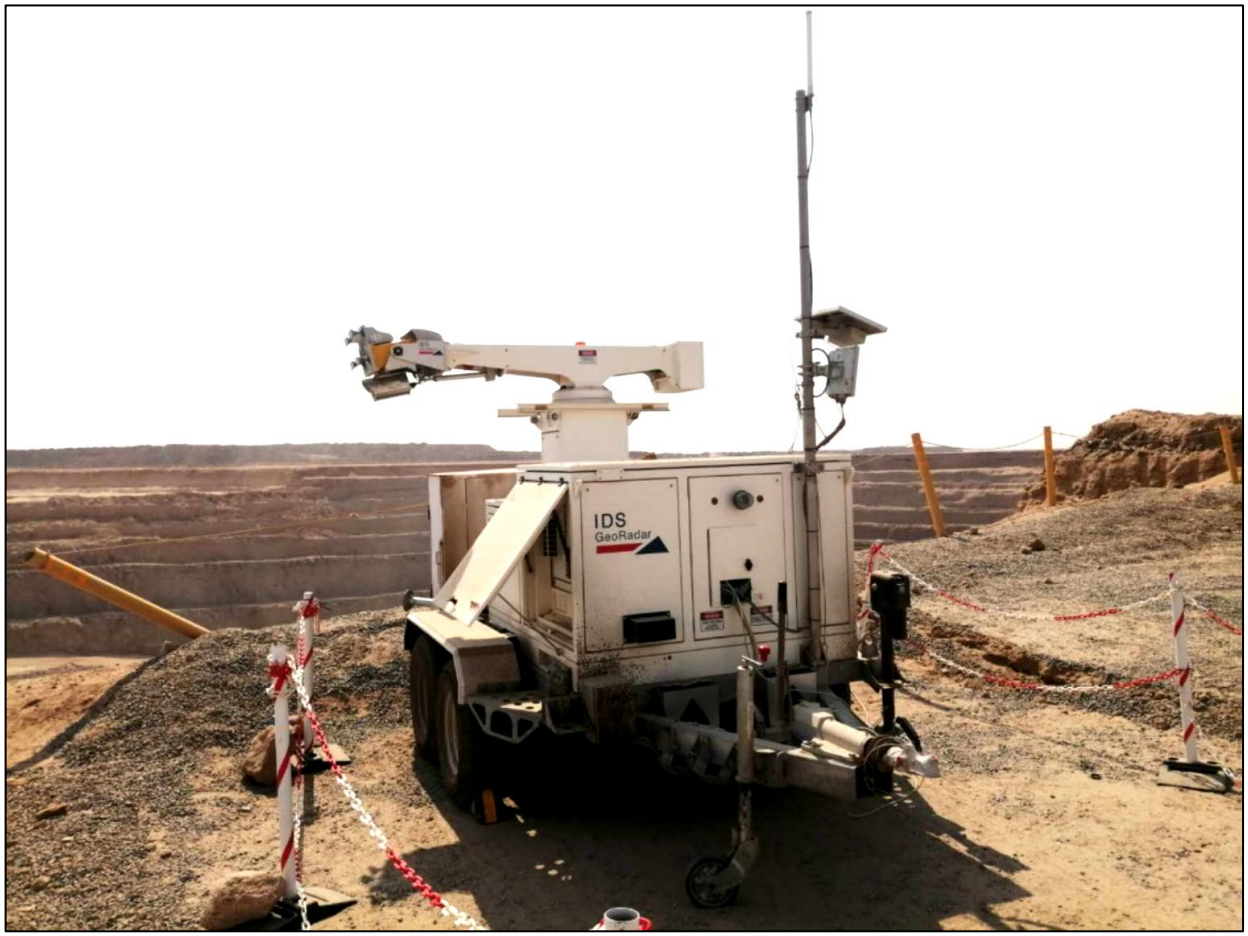


Figure 2-11: IBIS-ArcSAR radar deployed in an open pit operation, photograph taken at Husab mine (Namibia)

Additional functionalities of the GBSAR are as follows;

- High spatial resolution and the ability to detect small scale failures;
- Real time slope monitoring;
- Automated atmospheric corrections;
- Low power consumption; as the systems are built to function on additional energy sources such as wind, diesel and solar energy; and
- Real-time remote sensing of up to 5 km and accuracy of 0.1 mm (IDS GeoRadar, 2022).

InSAR

InSAR technology is useful in monitoring mines, tailings facilities and mine infrastructure. Current available satellites on the market i.e. RADARSAT-2, TerraSAR- X and Tandem-X have a precision of 1 mm, with a return of at least 6 days. Due to the dynamic condition of mines, in that active pits are constantly changing, the best technology for active monitoring is ground-based radars. Combining the usage of ground-based radars and satellite radars is an effective monitoring strategy in early detection of failures (Henschel et al., 2014).

2.6 Methods to Predict Slope Failure

2.6.1 Introduction

All pit slopes experience early stages of movement, termed “Initial Response”. This stage of movement includes elastic rebound, relaxation, and dilation of the rock mass (Sullivan, 2007). According to Sullivan (2007), pit slope failures go through four main stages of slope movement;

- Viscoelastic response;
- Creep;
- Cracking and dislocation; and

- Collapse or failure

Figure 2 - 12 shows the strain versus time behaviour of rock, which begins with elastic strain of the material, which then progress to creep with time and ultimately to collapse. There are three main pit slope failure patterns (Zavodni and Broadbent, 1980);

- Regressive;
- Progressive; and
- Transitional.

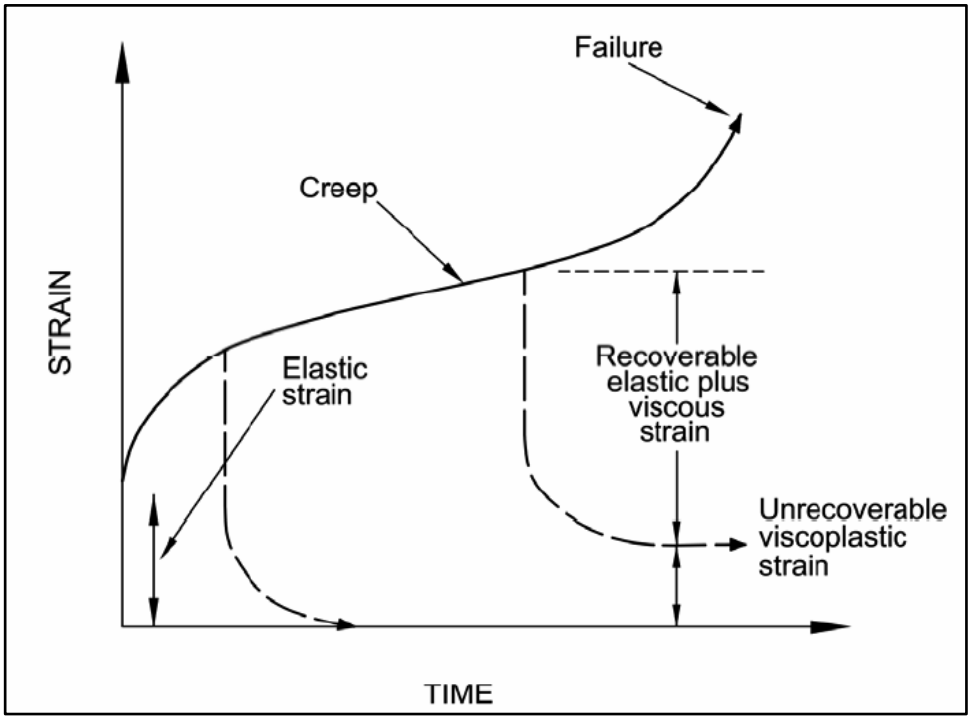


Figure 2-12: Strain versus time behaviour of rock (Adapted from Sullivan, 2007)

Regressive failure refers to a failing rock mass within a slope that re-stabilises as a result of the removal of the cause of the failure. The velocity in such circumstances remains constant, decelerates or slightly accelerates. Progressive failure state refers to the continuous increase in velocity within a

failing rock mass, up to the point of failure. Transitional failure is the change from regressive failure to progressive failure (Zavodni and Broadbent, 1980). When a progressive failure is identified, immediate actions can be implemented to minimise the geotechnical risk to the operation. Transitional type of failures begin as regressive, but with time, due to external factors, develop into progressive failures. Therefore, transitional type of failures can be avoided by applying timeous, extensive engineering, control, reconstruction and implementation of safety measures (Zavodni and Broadbent, 1980). When slope failures occur before the predicted or estimated time to failure, such predictions are unsafe to mining operations. Premature failures are a safety hazard. They can also potentially cause reputational damage to an operation and ultimately, the mining company. Timeous predictions give advanced warning such that losses are minimised in the event of a failure (Osasan and Stacey, 2014). Methods utilised to predict slope failure are discussed in the following sections.

2.6.2 Strain deformation approach to failure prediction

A good understanding of the deformation of slopes can be an effective way of predicting failure. Pre-failure deformation of a slope is associated with the creep phenomenon (Zhang et al., 2020). Deformation of rock mass subjected to creep can be subdivided into three stages (Figure 2 - 13).

- Primary creep;
- Secondary creep; and
- Accelerated creep.

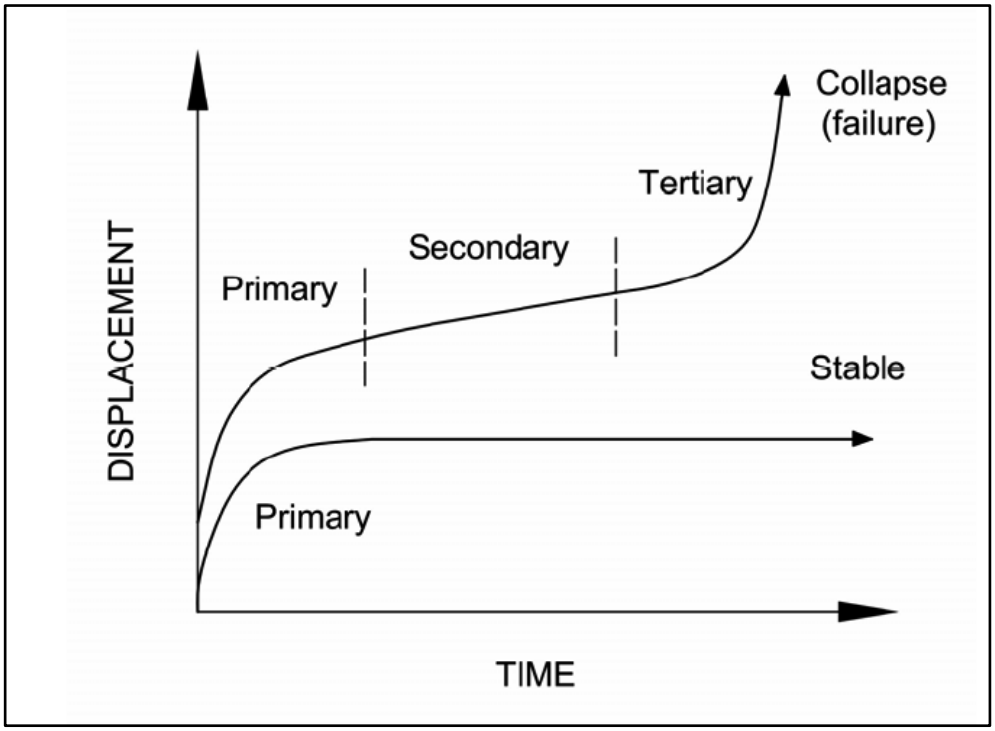


Figure 2-13: Displacement versus Time schematic diagram for all stages of a moving slope (Adapted from Sullivan, 2007)

Deformation time graphs of slopes often take the form of accelerated creep before failure. Hence, the third stage (accelerated creep) is often used to predict failure (Zhang et al., 2020). Figure 2 - 14 shows the displacement time curves for slope failures. Clear understanding of the movement curves can assist Geotechnical practitioners on mines in taking proactive remedial measures in minimising economic impact as a result of potential slope failures (Sullivan, 2007).

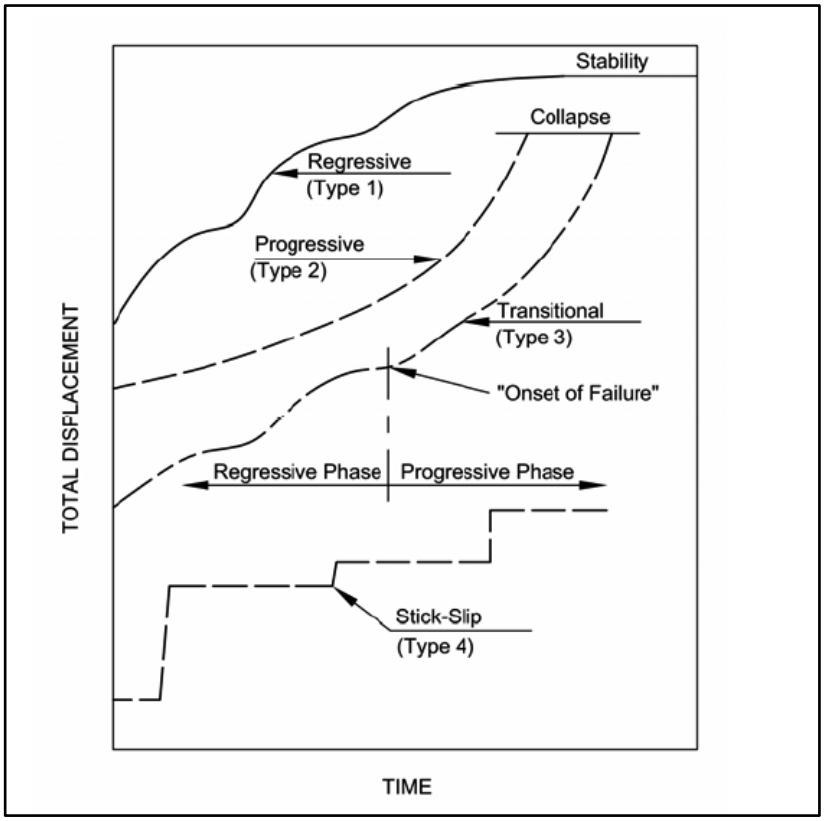


Figure 2-14: Schematic diagram of displacement time curve for pit slope failures (Adapted from Sullivan, 2007)

The use of strain measurements to predict failure has been historically applied in most South African underground mines. The advantages of the strain-based approach method is that it can be easily applied as it is simple technology, which can be used at the planning stage to determine suitable monitoring tools. Strain thresholds can be applied at the onset of slope monitoring, driven by anticipated failure mechanisms. The strain method approach has the following limitations to accurately determine a failure criterion (Newcomen and Dick, 2016):

- Slope monitoring implementation is required at the early stages of a mining project, which may be costly;
- Strain along a failure plane is not determined;
- Changes in the rockmass strength as more rock is exposed, could result in erroneous results; and

- The understanding of the failure mode of a pit slope is required to correctly predict strain to collapse.

The high wall strain empirical criteria was recommended by Brox and Newcomen (2004) as a good method that could be applied as a first check for pit slope stability assessment. Mine practitioners compare the predicted strain values from elastic stress-deformation models to actual measured deformation values from prism data to asses slope performance (Brox and Newcomen, 2004). Table 2-3 shows the threshold strain levels for the formation of tension cracks, progressive movement and imminent failure. The equation on how strain is calculated is given as follows:

$$High\ wall\ strain\ = \frac{Maximum\ high\ wall\ deformation}{Total\ highwall\ height} \qquad \textit{Equation 2-1}$$

Table 2-3: Threshold strain levels for key stages of high wall stability (Modified from Brox and Newcomen, 2004)

High Wall Stability Stage	Threshold Strain level %
Tension cracks	approx. 0.1
Progressive movement	approx. 0.6
Imminent failure/collapse	>1

Successful application of the strain-based criteria method requires a good understanding of the failure mechanism of the rock mass. Each failure mode has its own strain threshold criteria (Newcomen and Dick, 2016). According to Brox and Newcomen (2004), planar and wedge instability occur at low strain values in brittle rock masses. Planar instability happens when movement occurs along a single joint plane. Wedge instability is initiated when movement occurs along two well defined joint planes. The study carried out by Brox and Newcomen

(2004) further concluded that planar failure occurs at the lowest strain ranging between 0.03% and 0.06%. The wedge failure mode had a minimum strain of 0.2%. Figure 2 - 15 shows the High wall strain criteria as proposed by Brox and Newcomen (2004).

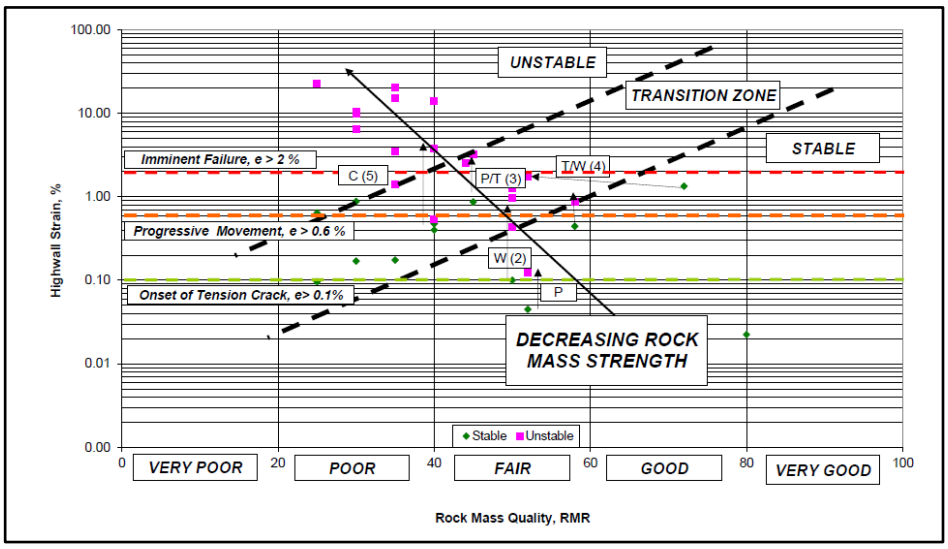


Figure 2-15: Highwall Strain % vs. Rock Mass Quality as a useful tool for slope failure prediction and highwall performance analysis (Adapted from Brox and Newcomen, 2004)

2.6.3 Inverse velocity method

The inverse velocity method was first introduced by Fukozono in 1985 (Rose and Hungr, 2007). The method was only first applied in 2001 for the prediction of three large scale failures (Rose and Hungr, 2007):

- The Betze – Post high slope failure that occurred in 2001 involving a 550 m high slope;
- Predictive analysis was carried out for a 465 m high slope of an undisclosed mine; and
- Slope failure prediction of a 120 m high slope of the Betze – Post pit.

The inverse velocity method is a useful tool for analysing slope monitoring data and determining potential failure time. This method works best when the rock mass failure condition has a ductile nature and has no external influence, such as blasting and loading activities contributing to the failure process (Rose and Hungr, 2007).

In situations where the failure mechanism is brittle or instantaneous in nature, it is often difficult to determine the time of failure. The accuracy of predicting slope failure time is achieved when the slope is approaching failure (Rose and Hungr, 2007). Figure 2 - 16 is a display of inverse velocity versus time plot, predominantly used in failure prediction analysis.

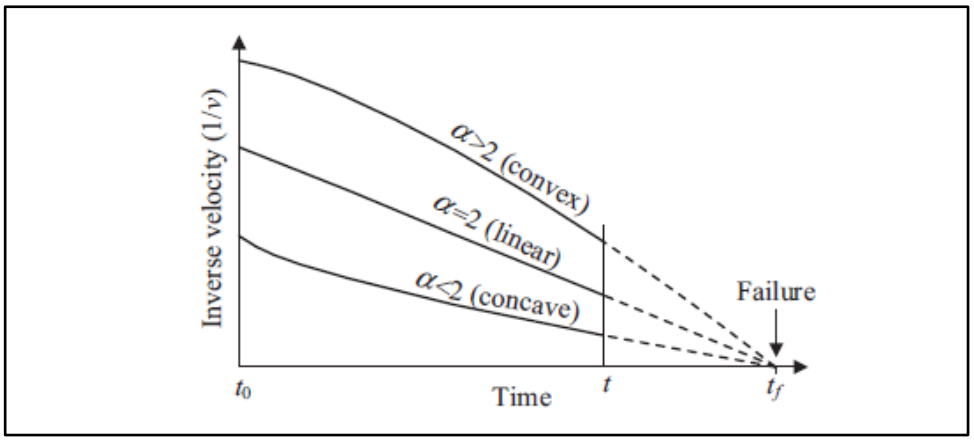


Figure 2-16: Inverse velocity versus time plot (Adapted from Osasan and Stacey, 2014)

The inverse velocity method requires filtering process to reduce the effect of instrument error. There are two main filtering methods to improve data quality as proposed by Rose and Hungr (2007), however only one method is presented here to calculate velocity. The equation for velocity calculation is as follows;

$$v_i = \frac{d_i - d_{i-n}}{t_i - t_{i-n}} \qquad \textit{Equation 2-2}$$

Where t_i and d_i represent the latest time and displacement for collected data. For improved data quality, instrument error can be minimised by implementing the following (Rose and Hungr, 2007):

- Diurnal effects can be reduced by measuring the slope at the same time of the day;
- Operator error can be reduced by ensuring the same operators work on the instrumentation; and
- Horizontal and vertical angular errors can be reduced by only using measurements taken in the line-of-sight, particularly for prism monitoring.

Rose and Hungr (2007) cautioned that the method should be used with other methods. These findings agree with the study carried out by Newcomen and Dick (2016), as they warned that the data requires a considerable amount of smoothing to get it to converge. The effectiveness of the method works best when a slope is close to the time of failure.

Rock masses that exhibit brittle behaviour are a concern as they provide little precursor deformation before failure. The variability of slope behaviour makes it a difficult task to predict a failure time Carlá et al. (2017). Furthermore, Carlá et al. (2017), concluded that slope monitoring programs and early warning systems should be designed to be site-specific to honour the slope characteristics and deformation behaviour of the rock mass.

2.6.4 Slope gradient method (SGM)

Mufundirwa et al. (2010) reviewed the inverse velocity method and developed the SGM method to predict life expectancy of failure events. The SGM method is based on a slope (gradient) to compute failure time. Two variables are used in the analysis; displacement and time. The displacement velocity multiplied by time is plotted on the y-axis and the displacement velocity is plotted on the x-axis. The gradient of the resultant graph determines the Time of Failure (TOF) (Shellam and Coggan, 2020).

Failure predictions were made using circumferential strain and axial strain from laboratory conditions of uniaxial compression and Brazilian tensile creep tests. A conceptualised model representing “safe” and “unsafe” predictions was proposed, as shown in Figure 2 - 17. If the predicted failure time (T_{fp}) is above line AB, then the prediction is unsafe, meaning failure may occur before the predicted time. If the predicted failure time T_{fp} is within the triangle AOB, then the prediction is safe. If the predicted failure time is below the line OB, then the prediction is meaningless (Mufundirwa et al. 2010).

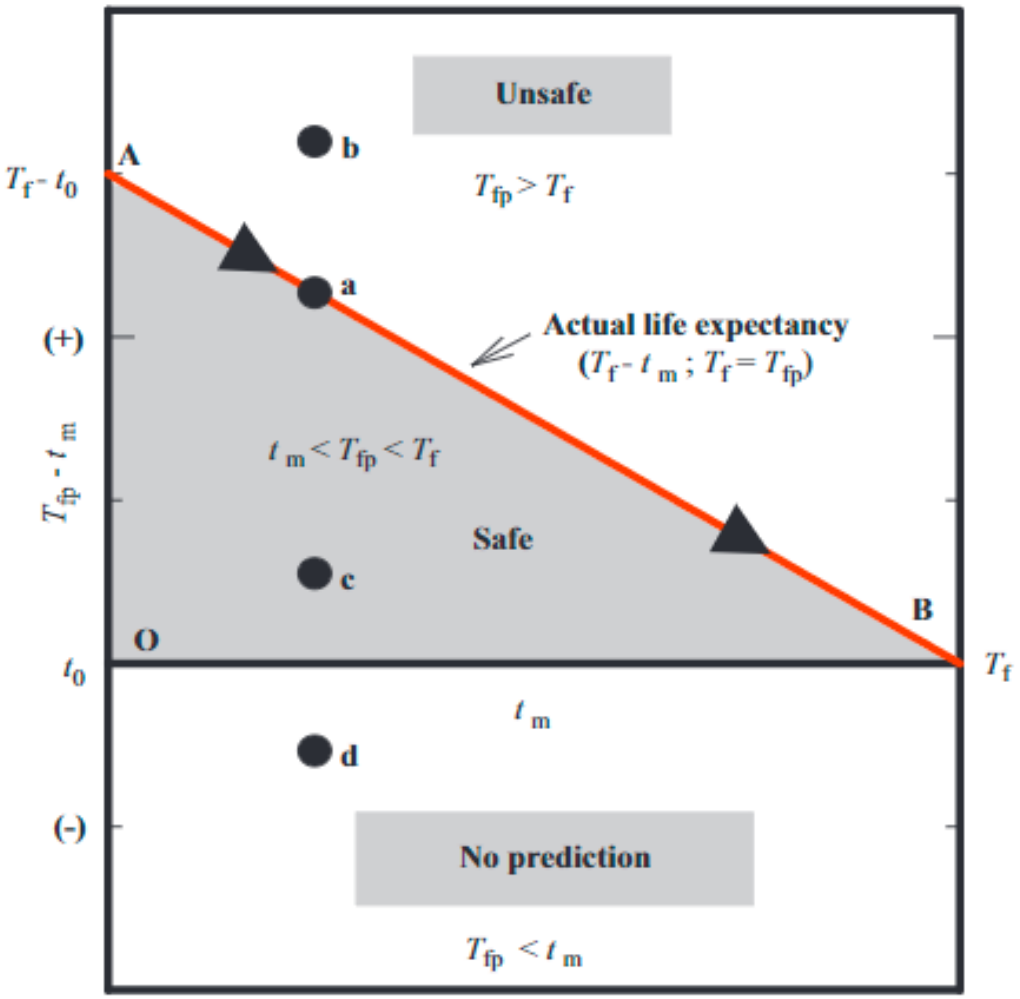


Figure 2-17: A conceptual model representing predicted life expectancy as a function of time (Adapted from Mufundirwa et al., 2010)

The research concluded that the SGM method gave safe predictions, and the inverse velocity method gave unsafe predictions of failure time for most case studies. The SGM method is based on the following equation;

$$t\left(\frac{du}{dt}\right) = T_f\left(\frac{du}{dt}\right) - B \qquad \textit{Equation 2-3}$$

Where t is the time, du/dt is the displacement rate, T_f is the failure time and B is a constant. The data filtering method for the SGM method is carried out by applying the following equation;

$$\left(du/_{dt}\right)_i = (u_i - u_{i-h}) \,/\, \left(t_i - t_{i_{-n}}\right) \qquad \textit{Equation 2-4}$$

(i= n+1, n+2,...m). Where (du/dt)i is the computed displacement rate, Um and tm are the time and displacement at the instant of prediction (Mufundirwa et al., 2010).

2.6.5 Acceleration and velocity approach

Federico et al. (2012) carried out a case study which incorporated 38 failures with various failure mechanisms. The authors proposed 'failure signatures' in relation to peak velocity and peak acceleration. It was suggested in the study that there is a close relationship between velocity and acceleration just prior to failure, as shown in Figure 2 - 18, in that, as acceleration increases, velocity also increases, which is evident in the dataset provided in Figure 2 - 18, with a good correlation of 0.89.

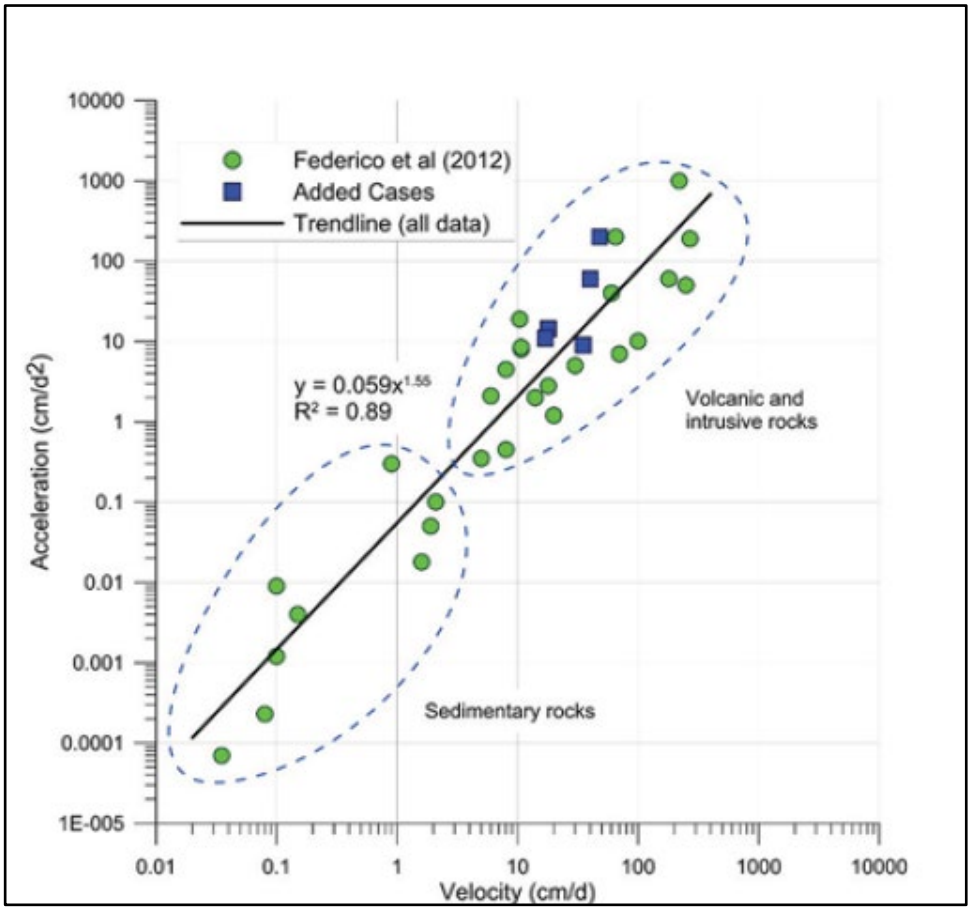


Figure 2-18: Relationship between acceleration and velocity (Adapted from Federico et al., 2012)

Carlá et al. (2017) made use of the acceleration and velocity method in their analysis of nine pit slope failures in brittle rock. The work concluded that planar failures, which tend to be small in volume, are characteristic of lower velocity and acceleration before failure, compared to complex failure mechanisms. It was concluded that additional work is required to confirm the usefulness of this predictive tool by adding more data points. Only the toppling failure mechanism did not conform to the expected trend.

2.6.6 Displacement vs. time plots

Displacement and Time are useful for failure analysis and prediction (Newcomen and Dick, 2016). However, Venter et al. (2013) cautioned on applying this method on its own, as it cannot be used to accurately predict slope

failure. Figure 2 - 19 shows the Deformation versus Time curve as a slope failure predictive method.

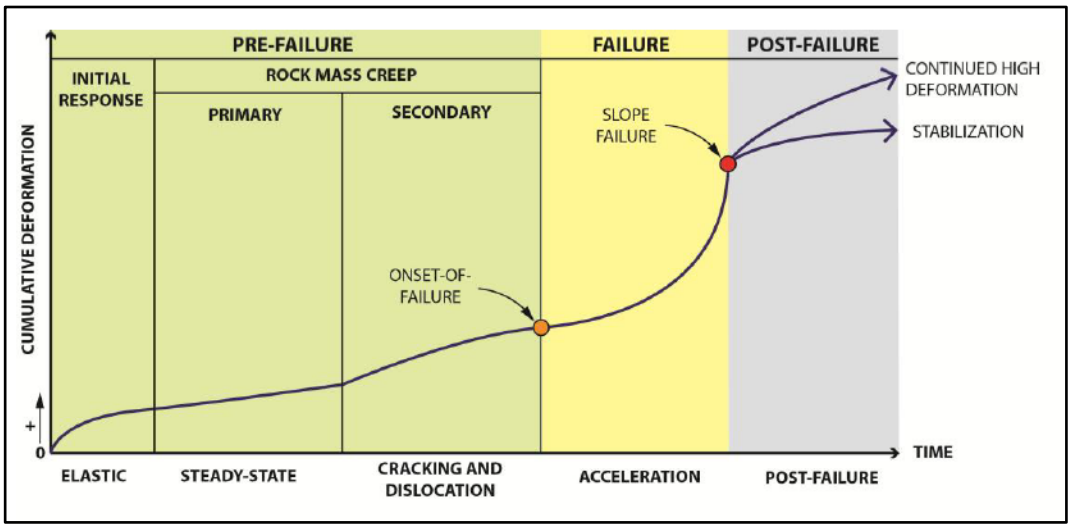


Figure 2-19: Deformation vs. Time curve used for failure analysis prediction (Adapted from Newcomen and Dick, 2016)

2.7 Rock Mass Classification Systems

Rock Mass Classification systems are a powerful tool for assessing ground conditions in mines and civil projects. The application of these tools can add significant value when used as a supplement to engineering design. The following classification systems are commonly applied in mining and civil projects (Tavakoli and Porter, 1994):

- The RQD system proposed by Deere in the 1960s (Zhang, 2016);
- The Rock Mass Quality System (Q – System) developed for application in empirical designs of tunnels and cavern reinforcement (Barton, 2002);
- The Bieniawski RMR has broad application in engineering such as mines, foundations, tunnels and slopes (Kundu et al., 2020); and
- The Mining Rock Mass Rating (MRMR), a useful tool in rock engineering for classification of rock mass competency (Jakubec and Laubscher, 2000).

The application of Rock Mass Classification systems is used to understand the behaviour and characteristics of rock masses (Tavakoli and Porter, 1994). Only the RMR (Kundu et al., 2020) system was used in the research described in this report.

2.8 RQD

The RQD system was initially developed by Deere in 1964 (Zhang, 2016). The RQD is a measure of the quality of the rock mass, applied in rock mass classification systems i.e. Q – System (Barton, 2002) and the RMR (Kundu et al, 2020). RQD is determined from drill hole core by measuring all pieces of core that are more than 10 cm in a run (length of the core run) and dividing that over the length of the core run, which is then expressed as a percentage.

$$RQD = (Total\ length\ of\ core \geq 10\ cm) / (Length\ of\ core\ run) \qquad \textit{Equation 2-5}$$

RQD can also be estimated from exposed rock surfaces by the number of joint planes per m^3 of rock. This is accomplished by determining the number of joint planes which cross a 2 m to 3 m length of tape held against a rock wall. The number of joint planes divided by the relevant sample length gives the number of joints per meter. This process must be repeated for all three directions. Jv is determined by the number of joints per m3, and RQD established from the equation (Palmström, 1982):

$$RQD = 115 - 3.3Jv \qquad \textit{Equation 2-6}$$

Where, Jv is the number of joints per m^3.

2.8.1 RMR – Bieniawski 1976

The RMR system is based on the addition of five key parameters;

- Strength of intact rock material;

- Drill Core quality (RQD);
- Condition of joints;
- Spacing of joints; and
- Ground water condition.

The RMR classification system is ranked on a scale of 0 to 100, where very poor rocks have low ratings (<20) and very good rocks have higher ratings (>80) as shown in Table 2-4 (Orr, 1992).

Table 2-4: Rock Mass Classes (Modified from Orr, 1992)

RMR Value	Class	Description
<20	V	Very poor rock
21 – 40	III	Poor rock
41 – 60	III	Fair rock
60 - 80	II	Good rock
>80	I	Very good rock

The correlation between the RMR and the Q system is given in the following equation;

$$RMR = 9InQ + 44$$ *Equation 2-7*

2.9 Chapter Summary

The geometry of pit slopes is governed by the following factors; rock mass quality, rock mass strength, size and shape of the ore body, structural complexity and rock fabric.

The causes of slope failures are variable ranging from:

- Mining induced stress;
- Tectonic stresses;
- Rock mass structure;
- Rock mass quality and strength;
- Blasting practices;
- Seismicity and the effect of pore water pressure on pit slopes.

The most common failure mechanisms in slopes containing hard rock are; plane failure, wedge failure and toppling failure.

- Plane failure occur when major structural discontinuities daylight toward an excavation;
- Wedge failure involve sliding of tetrahedral shaped blocks on more than one discontinuity plane; and
- Toppling failure involve steeply dipping discontinuities that form parallel or almost parallel to the slope.

Slope monitoring methods form an integral part of risk management in mining operations. The purpose of slope monitoring is to increase safety in mining operations, therefore reduce mining injuries to personnel and equipment damage. The following slope monitoring methods are employed in open pit operations;

- Visual inspections;
- Photogrammetry;

- Extensometers and Inclinometers;
- LiDAR;
- InSAR;
- Total Stations: Prism monitoring; and
- Slope Stability Radars: RAR and SAR.

Slope failure prediction is a very critical component for geotechnical engineers on mining operations. Safe prediction is important in ensuring mining is carried out in a safe manner. The following methods are used to predict failure;

- High Wall Strain Criterion;
- Inverse velocity method;
- Slope Gradient method;
- Acceleration and Velocity approach; and
- Displacement versus Time plots.

Rock Mass Classification systems are powerful tools used for assessing ground conditions in mines and civil projects. The following common rock mass classification systems are applied; RQD; and the Bieniawski RMR system.

3 METHODOLOGY

3.1 Introduction

The Husab Mine has implemented slope monitoring instrumentation to assess day to day pit slope stability. Prior to 2019, the mine had no slope monitoring systems in place, monitoring was primarily carried out through visual inspections and manual tension crack measurements.

Over the years the mine has implemented slope monitoring systems such as prism monitoring, primarily used as long term monitoring tools to identify potential areas of instability. Radars are used for monitoring critical areas of instability and InSAR monitoring to assess deformation for the entire project ranging from pit slopes to dumps and tailings facilities. The dataset used for this research was obtained from historic tension crack measurements, radar monitoring data and InSAR monitoring data source SkyGeo (a service provider to the mine). Prism monitoring data from the neighbouring Rössing Uranium Mine is incorporated in this research report as an additional case study.

3.2 Data Collection

Historic tension crack measurements were collected from an existing database. The high wall strain was then calculated for cracks closest to the failure. The strain deformation approach to assess high wall performance was applied for the first failure that occurred on the 5th of October 2018.

The database containing the information for the November 2020 failure was downloaded from the field radar computer. The following slope failure predictive methods were applied: Displacement versus Time plots, Velocity Versus Time plots and Inverse Velocity.

InSar monitoring data was downloaded from the SkyGeo website for a one-year period between August 2020 and August 2021. The following failure predictive

tools were applied to the dataset; Cumulative displacement versus Time plots, Velocity versus Time plots and Inverse Velocity.

Prism monitoring data of the Rössing Uranium Mine was obtained upon request, and a back–analysis of a slope-wall failure was carried out. Slope failure predictive methods were applied to the dataset such as Cumulative displacement versus Time plots, Velocity versus Time plots, Inverse Velocity and the Slope Gradient Method.

3.3 Data Analysis

The analysis was done using the following slope failure prediction methods;

- Strain deformation Approach;
- Inverse Velocity;
- Velocity;
- Cumulative Displacement; and
- The Slope Gradient Method.

3.4 Chapter Summary

The following slope monitoring systems have been implemented at Husab Mine:

- Prism Monitoring;
- Radar Monitoring of critical areas; and
- InSAR monitoring of the mining project, which include coverage of the two pit zones, dumps, tailings facilities and mining infrastructure.

Data was collected from the respective monitoring systems and in-house databases for the back-analysis work. The following methods were used for analysis work;

- High Wall strain criteria. Tension crack data was used for the analysis as there was no slope monitoring equipment at the time of failure (August 2018).
- The Reutech Radar data was used for the back-analysis of the November 2020 failure. The following slope failure predictive methods were used; velocity, inverse velocity and cumulative displacement.
- InSAR data was used for the back-analysis work of the August 2021 failure. The following slope failure predictive methods were used; velocity, cumulative displacement and inverse velocity.
- Prism monitoring data was sourced from the neighbouring Rössing Uranium mine. The following slope failure predictive methods were applied; high wall strain criteria, velocity, inverse velocity, cumulative displacement and SGM method.

4 ANALYSIS AND RESULTS

4.1 Introduction

Geotechnical Domain D is hosted within the Rossing Formation of the Swakop Group. The Formation is variable comprising of the following rock units; marble, pelitic schist and gneiss, biotite – hornblende, migmatite, calc-silicate, quartzite and metaconglomerate. The amphibole schist (Figure 4 - 1) is a 10 m thick weak friable layer bounded between the Khan and Rossing Formation. The exposure of this unit is believed to have contributed to bench-scale failures in Domain D.

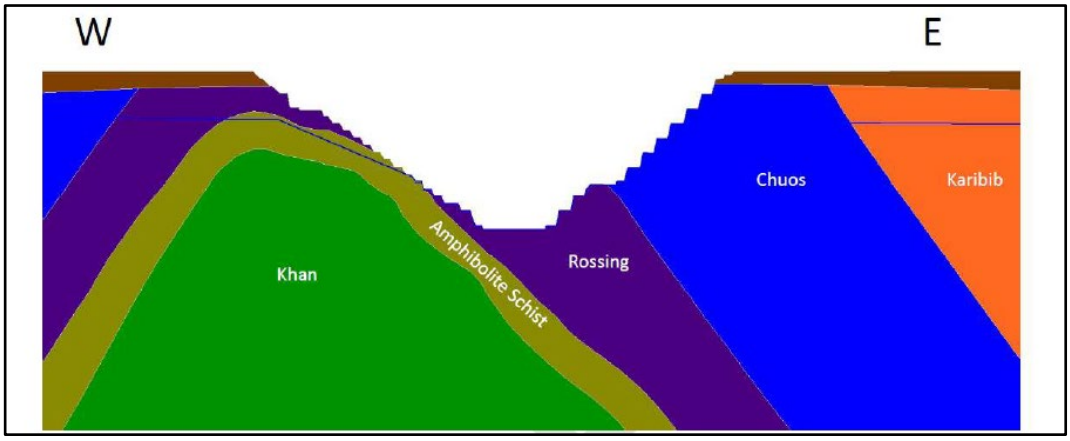


Figure 4-1: Geological Cross-section across Geotechnical Domain (Armstrong and Maduray, 2022)

Bench-scale failures have occurred where the amphibole schist unit daylight and the slope orientation is parallel to foliation planes (Armstrong and Maduray, 2022). The first failure was recorded on the 5th of August 2018. A subsequent failure occurred on the lower bench directly beneath the first failure in November 2020. A 3D photogrammetric model representing the first 2 failures is shown in Figure 4-2. The last failure occurred underneath the main ramp on the 20th of August 2021 shown in Figure 4 - 3. Overlapping photographs were taken from various angles and positions with the in-house DJI Mavic Air 2 drone. A high-resolution 3D photogrammetric model was created in Agisoft Metashape

software. Agisoft Metashape is a reliable industry software used for processing digital images for creation of 3D models (Agisoft, 2023). The Husab mine has implemented a comprehensive slope monitoring programme that includes:

- robotic total stations with prism monitoring;
- ground based radars; and
- satellite InSAR monitoring.

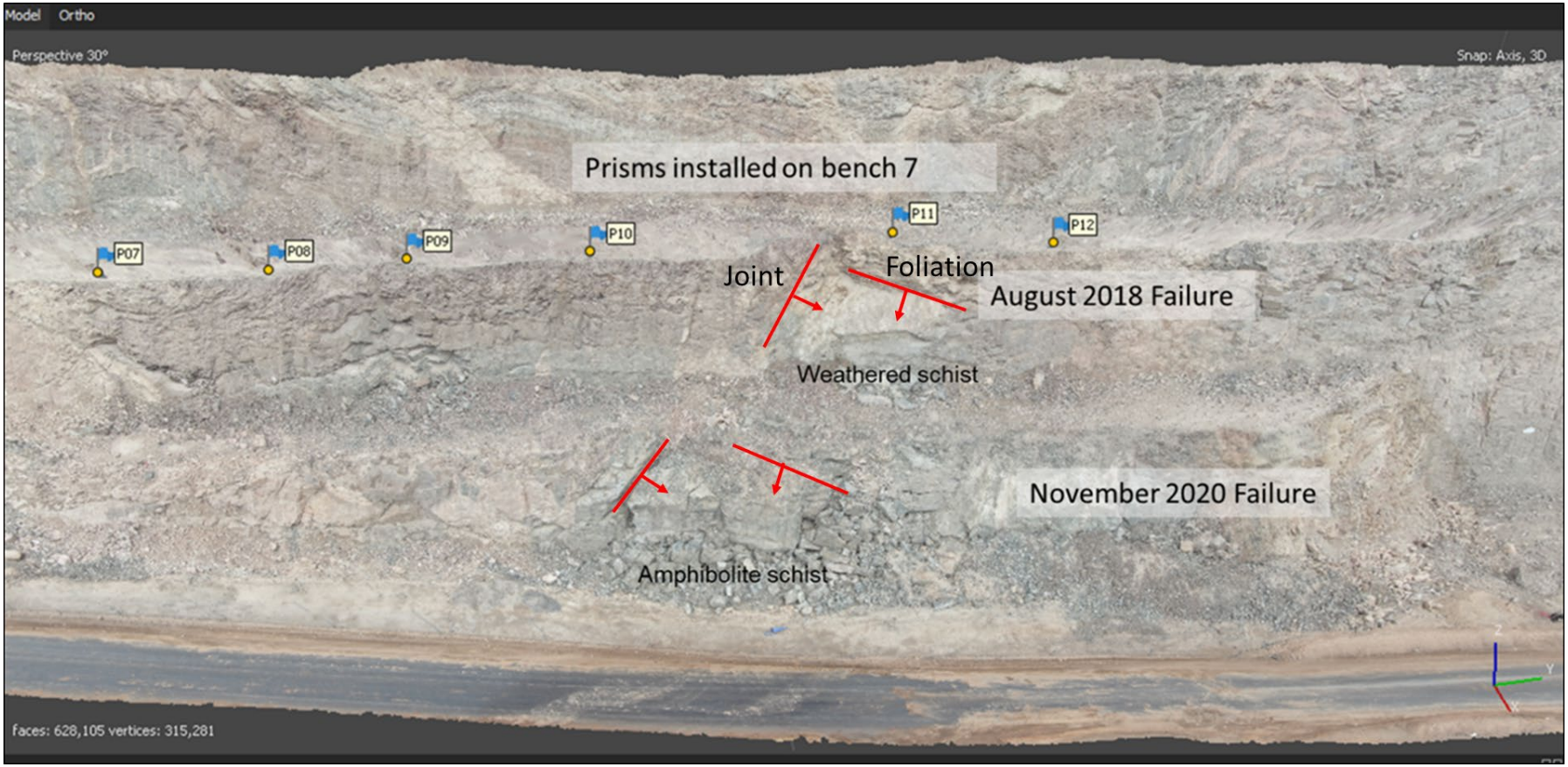


Figure 4-2: A photogrammetric 3D model created in Agisoft Metashape software, images taken with the DJI Mavic Air 2 Drone onsite (DJI, 2023)



Figure 4-3: August 2021 failure taken with the DJI Mavic Air 2 Drone

The Bieniawski RMR classification system has been applied to determine the quality of the Rock Mass. The spacing, orientation and condition of discontinuities were obtained from the scanline mapping data. The Uniaxial Compressive Strength (UCS) data was obtained from lab test data for boreholes drilled within Geotechnical Domain D during the 2017 study and feasibility study (Appendix E). The Rossing Formation is variable consisting of rock units varying from calc-silicates to marbles, biotite schist, amphibole schist, gneiss, with Intrusives, therefore the UCS values are variable. The RQD data was obtained from the onsite drill core data. The RMR calculations are presented in Table 4-1. Joint set 1 (J1) has an average spacing of 0.22 m, Joint set 2 has an average spacing of 0.23 m and Joint set 3 has an average spacing of 1.33 m. Therefore, referring to Equation 2-6, the RQD is equivalent to 83.

Table 4-1: RMR analysis

Parameter	Condition	Rating
Uniaxial Compressive Strength Test (UCS)	78 MPa	7
Rock Quality Designation (RQD)	80	17
Spacing of discontinuities	200 – 600 mm	10
Condition of discontinuities	Rough-Surfaces, separation <1mm, highly weathered walls	20
Ground Water	Dry	15
Adjustment for joint orientation	Unfavourable	-10
Total Rating	**Fair Rock**	**59**

A back-analysis was carried out for all three failures presented in Case Studies 1, 2 and 3. The neighbouring Rössing Uranium Mine's prism monitoring data is also incorporated as a case study. It is presented as Case study 4. The failure analysis approach for each Case Study is provided in the following sections.

4.1.1 Case study 1: 5 August 2018 failure

On the 5th of August 2018, a bench-scale failure occurred on bench 7 of Domain D (Figure 4 - 2). A rock mass of approximately 15.6 m in length and 15 m in height collapsed. The failure mechanism was a wedge failure. No injuries or damage to equipment were incurred. At the time of the bench failure, routine manual tension crack measurements and daily field visual inspections were being carried out by the onsite-geotechnical team. At the time of the August 2018 failure, there was no equipment to monitor full slope movements on the mine. Therefore, for the Case Study, tension crack opening data was used to determine the high wall strain. The subsequent results were plotted against the Rock Mass Rating (RMR) on the Brox and Newcomen (2004) diagram and the results were compared with published results, to assess high wall performance. Cumulative displacement of the tension crack data was plotted for the duration leading to the failure date.

Scanline mapping of discontinuities that contributed to failure was conducted by the onsite geotechnical geologists in 2018, and the data was used for the analysis. Kinematic analysis was carried out in Rocscience DIPS software for identifying critical zones and intersections for the following failure modes; planar and wedge sliding (Rocscience, 2023). The quality of the rock mass was established using the RMR system (Kundu et al., 2020).

Kinematic analysis

Figure 4-4 shows the structures as discs, mapped through scanline mapping across the Domain D area. A list of the geotechnical properties of individual discontinuities for the failure area is provided in (Appendix A). The area is comprised of shallow to moderately dipping foliation planes (approx. 20° to 60°) dipping East (approx.128°) defined as Set 1. Set 2 is comprised of steeply dipping structures (approx. 80°) dipping towards the North-East (approx. 67°) and Set 3 is comprised of moderately dipping structures (approx. 53°) dipping toward the North (300°). The discontinuity surfaces are altered and are rough undulating. Joint infilling varies in thickness from less than 1 mm to >200 mm (fault gouge material).

The orientations of the discs show the daylighting discontinuities. The orientation of structures in relation to the wall orientation indicate the likelihood of planar and wedge sliding. Kinematic stability analysis results are shown in Figure 4-5 and Figure 4-6. The discontinuities that contributed to the failure have the following orientations:

- Plane A; shallow-dipping foliation plane, daylighting and parallel to the wall orientation; with a dip angle of 39°and dip-direction of 134°; and
- Plane B, steeply dipping joint; with a dip-angle of 80°and dip-direction 63°.

The slope orientation at the site was 75/108 and a friction angle of 32° was assumed, derived from the 2022 Geotechnical drilling shear box lab test results.

Kinematic analysis results show that wedge sliding has a 100% chance of occurrence, planar sliding is 50% for both joint sets and 100% for the foliation plane which was orientated at 39/134.

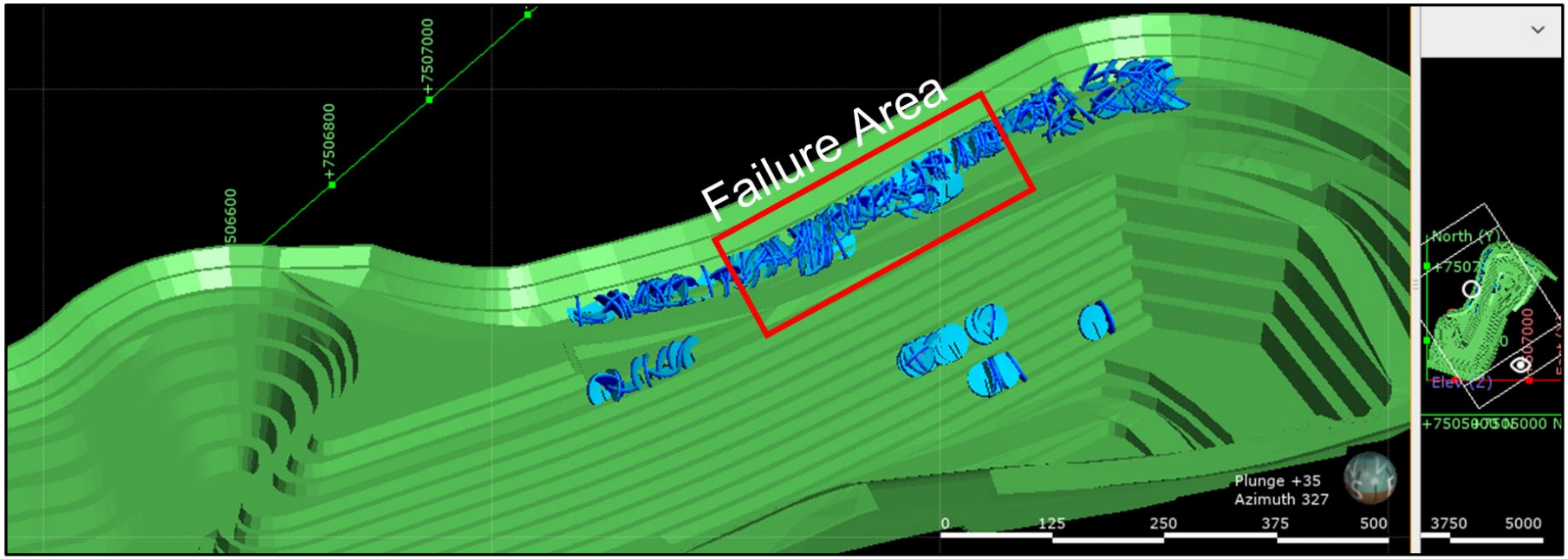
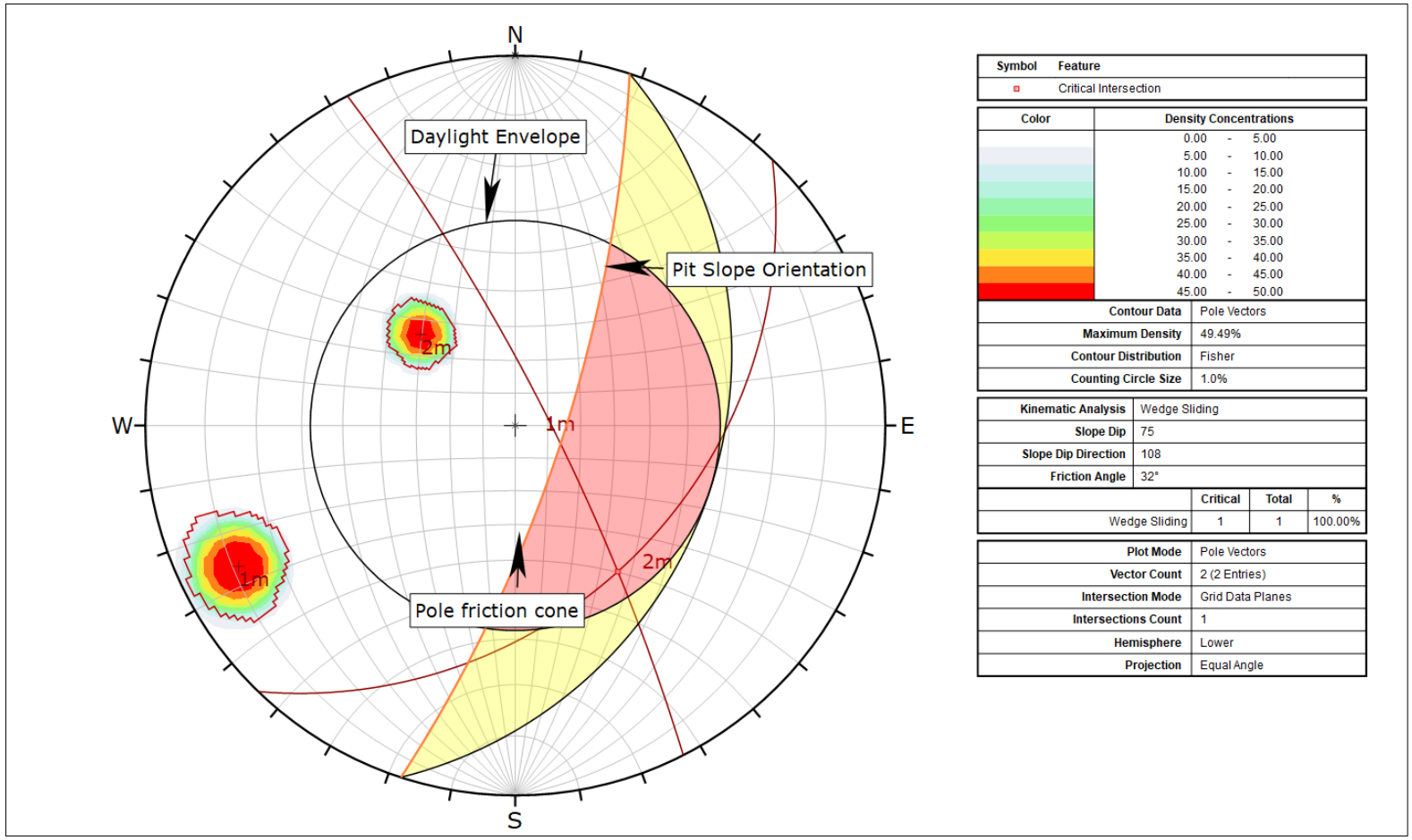


Figure 4-4: Scanline mapping data of discontinuities mapped across the Domain D area, discontinuities are represented as discs (Leapfrog, 2023)



Symbol	Feature
▫	Critical Intersection

Color	Density Concentrations
	0.00 - 5.00
	5.00 - 10.00
	10.00 - 15.00
	15.00 - 20.00
	20.00 - 25.00
	25.00 - 30.00
	30.00 - 35.00
	35.00 - 40.00
	40.00 - 45.00
	45.00 - 50.00

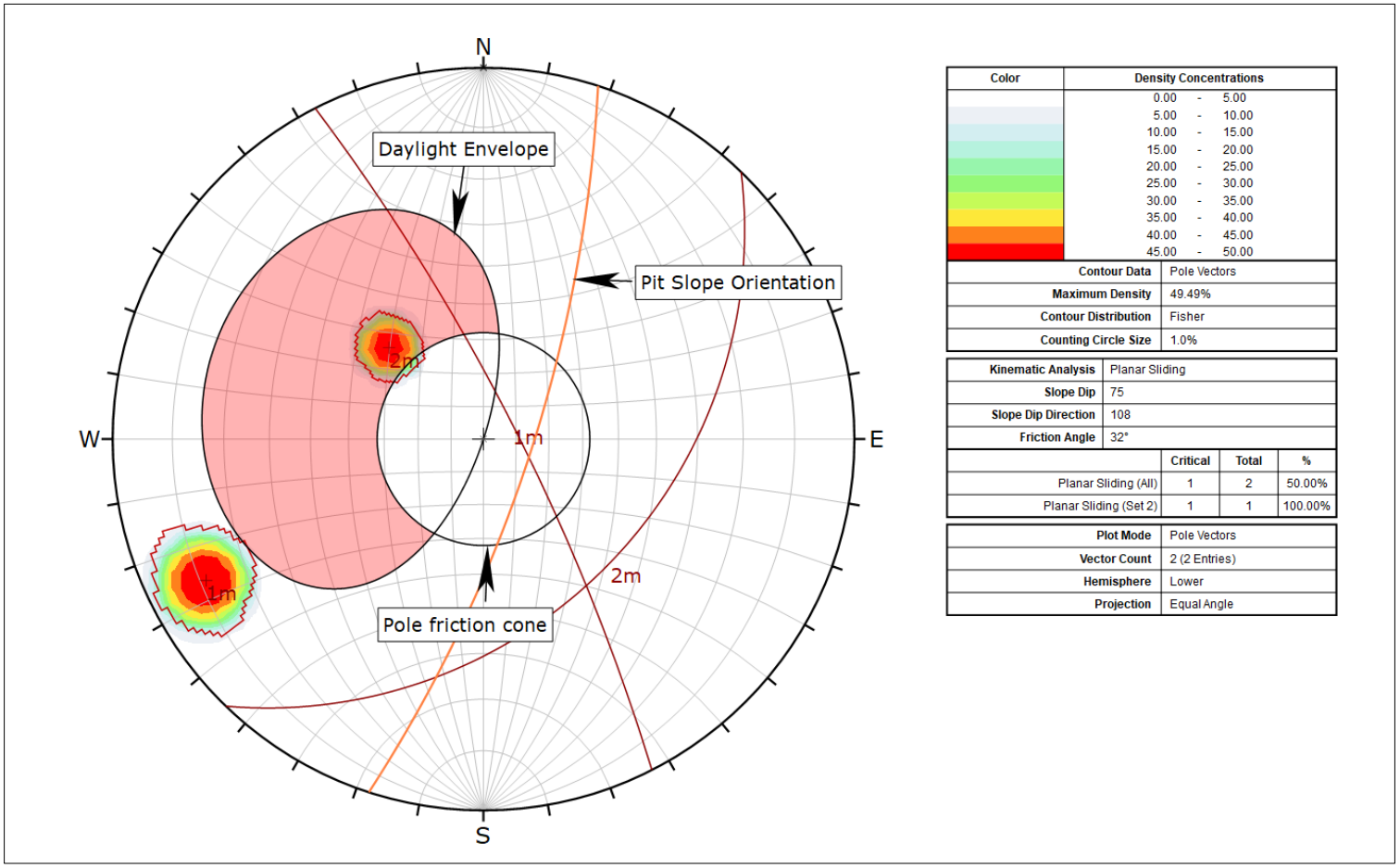
Contour Data	Pole Vectors
Maximum Density	49.49%
Contour Distribution	Fisher
Counting Circle Size	1.0%

Kinematic Analysis	Wedge Sliding
Slope Dip	75
Slope Dip Direction	108
Friction Angle	32°

	Critical	Total	%
Wedge Sliding	1	1	100.00%

Plot Mode	Pole Vectors
Vector Count	2 (2 Entries)
Intersection Mode	Grid Data Planes
Intersections Count	1
Hemisphere	Lower
Projection	Equal Angle

Figure 4-5: Kinematic analysis of discontinuities that contributed to the wedge failure



Color	Density Concentrations
	0.00 - 5.00
	5.00 - 10.00
	10.00 - 15.00
	15.00 - 20.00
	20.00 - 25.00
	25.00 - 30.00
	30.00 - 35.00
	35.00 - 40.00
	40.00 - 45.00
	45.00 - 50.00

Contour Data	Pole Vectors
Maximum Density	49.49%
Contour Distribution	Fisher
Counting Circle Size	1.0%

Kinematic Analysis	Planar Sliding
Slope Dip	75
Slope Dip Direction	108
Friction Angle	32°

	Critical	Total	%
Planar Sliding (All)	1	2	50.00%
Planar Sliding (Set 2)	1	1	100.00%

Plot Mode	Pole Vectors
Vector Count	2 (2 Entries)
Hemisphere	Lower
Projection	Equal Angle

Figure 4-6: Kinematic analysis of discontinuities that contributed to planar sliding

Swedge analysis

The wedge failure was analysed in the Rocscience Swedge software to determine the Factor of Safety (FOS) (Figure 4-7), a design acceptance criterion in engineering. FOS refers to the ratio of the shear strength of the material of a slope and the shear stress that develops along a potential failure surface (Read and Stacey, 2009). The following input parameters were used to carry out the analysis; cohesion 0 KPa, friction angle of 32°. The joints in the rock are cohesionless, as a result of blasting and opening up of foliation planes, therefore loss of shear strength along joint surfaces. Joint 1 orientation dip (39°), dip-direction (134°), Joint 2 orientation dip (80°) and dip – direction (63°), Slope orientation (Dip/Dip Direction) 75°/108°. From the analysis, the FOS is 0.772. Limit Equilibrium is achieved when the FOS is 1. A FOS of less than 1, satisfies the condition for failure (Read and Stacey, 2009).

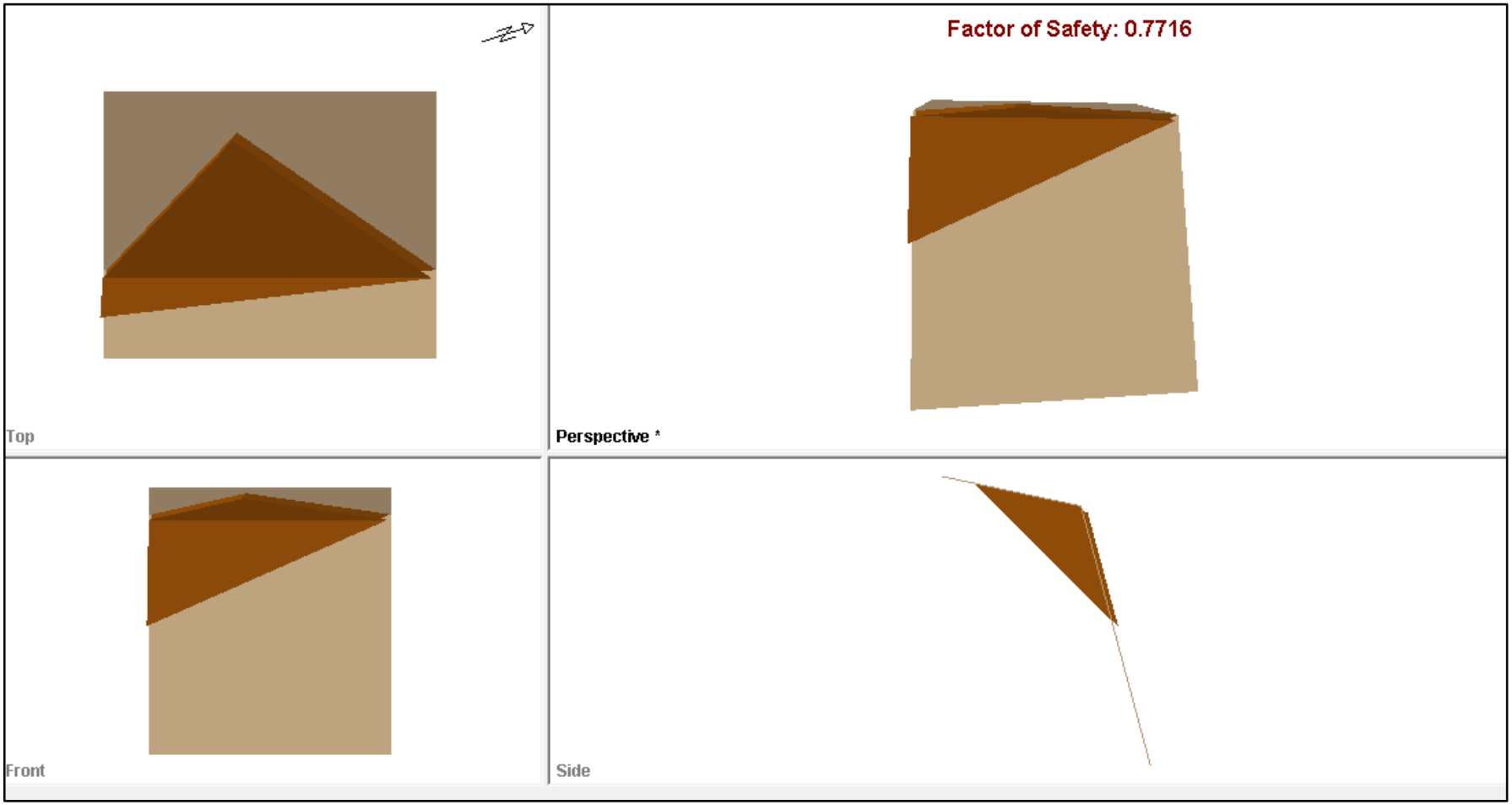


Figure 4-7: Swedge analysis carried out in Rocscience Swedge software, FOS is 0.772

Tension crack monitoring

Development of tension cracks were observed on Bench 7 above the failure area, along the bench crest. Metal crack pins were installed in the ground on either side of each crack, displacement measurements were then measured manually at least once a month. The first measurement was recorded on the 11th of July 2018, the second measurement was recorded on the 21st of July 2018 and the last measurement before failure was recorded on the 1st of August 2018. Figure 4-8 shows an example of metal pins installed in the ground that were used to measure tension crack openings back in 2018 (Husab Mine Site). The maximum horizontal displacement was 4 mm on crack 1A, followed by crack 1B with 2mm displacement. Crack 1C did not show any movement, from the initial measurement recorded. Increase in displacement was observed for cracks 1A, 1B, 2A and 2B (Figure 4-9). Unfortunately, the time period between readings was too long, and the most important deformations just preceding failure were not measured.

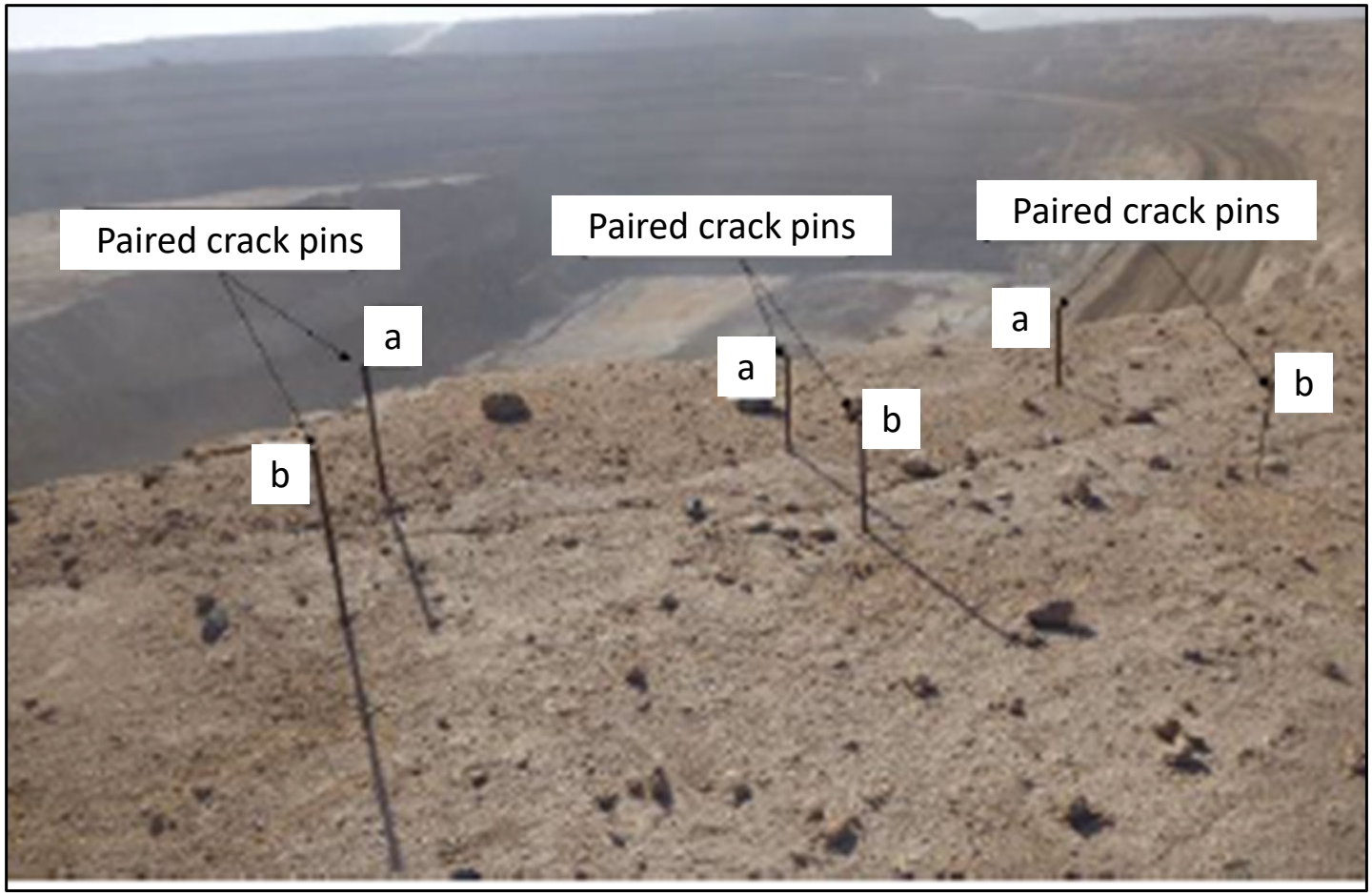
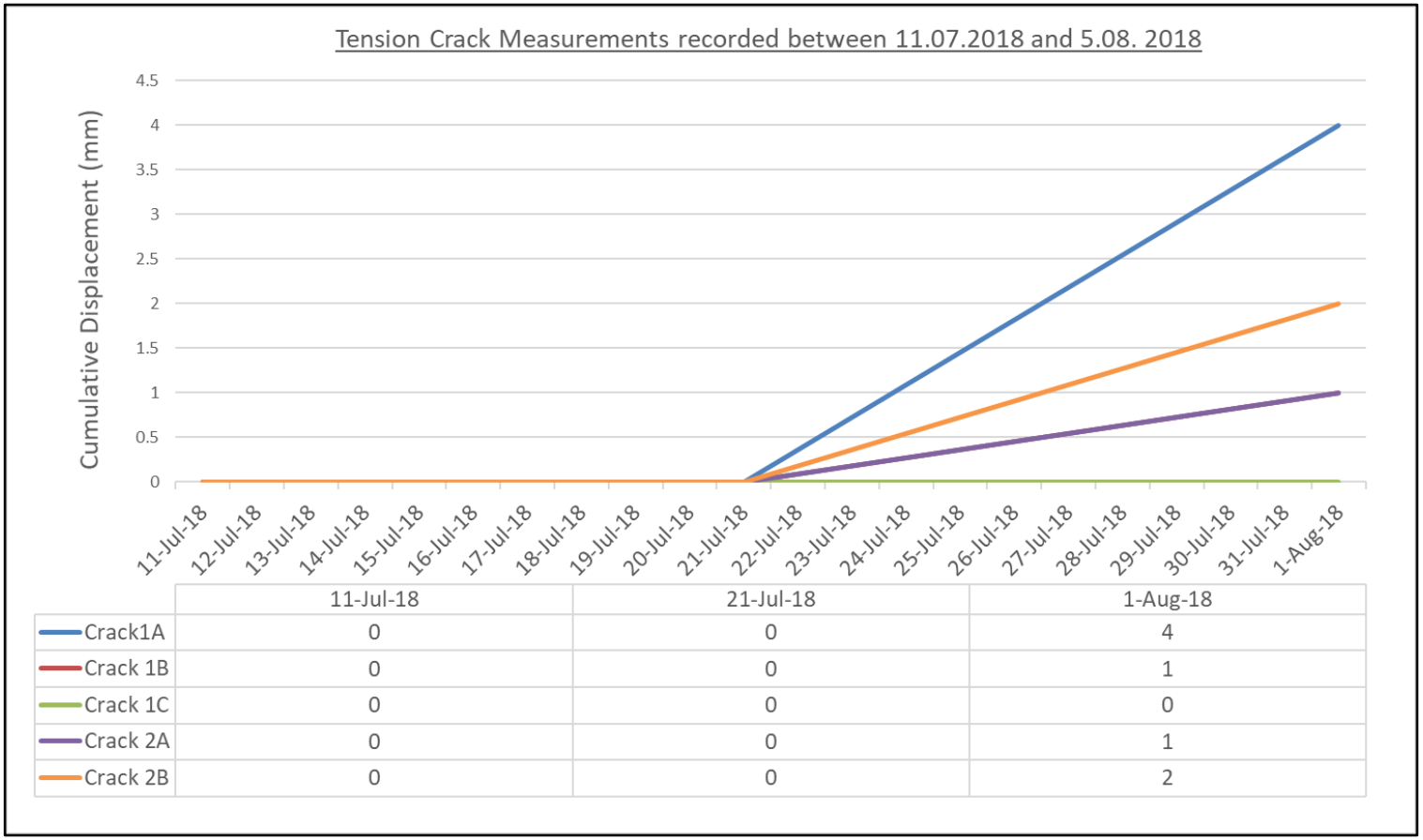


Figure 4-8: An example of metal pins installed in the ground for tension crack monitoring at the Husab Mine's Zone 2 pit-perimeter



	11-Jul-18	21-Jul-18	1-Aug-18
Crack1A	0	0	4
Crack 1B	0	0	1
Crack 1C	0	0	0
Crack 2A	0	0	1
Crack 2B	0	0	2

Figure 4-9: Tension Crack measurements taken along Bench 7 crest, measurements taken between 11 July 2018 and 1 August 2018

High wall strain criterion - Brox and Newcomen (2004)

An empirical high wall strain criterion developed by Brox and Newcomen (2004) to predict high wall stability performance was applied in this case study. The criteria makes use of the following parameters: high wall strain, rock mass quality and failure mechanism of the rock mass. The criteria is based on the understanding that highwalls being constantly exposed to blasting and excavation, undergo unloading processes, resulting in stress relaxation of the rockmass. Therefore, the rockmass deteriorates with time. High wall strain was calculated using empirical values of the high wall strain criteria indicates that strain values above 1% could have abrupt failure. Maximum tolerable strain values for a regressive slope should range between 0.6 and 1% (Brox and Newcomen, 2004). The amount of strain that can initiate failure in planar and wedge instability is relatively low, compared to toppling failure. The results of the investigation are presented in Table 4-2. Significant amounts of deformation were missed due to the long period between measurements.

Table 4-2: Strain (%) calculated for Cracks 1A and 2B, with the highest deformation

Crack-ID	Maximum Deformation of the high wall (m)	Height of the high wall (m)	Calculated Strain ε (%)
Crack 1A	0.004	15	0.02667
Crack 2B (closest to the failure)	0.002	15	0.01333

The calculated High wall strain of 0.01% and 0.02% is plotted against the RMR of 59 Figure 4 - 10. The calculated strain data plots in a stable region. The empirical high wall strain criteria was developed based on prism monitoring data, measured with automated total stations and theodolites, which are more accurate and have more data points recording slope deformation. At the time of failure in 2018, there was no slope monitoring equipment on the mine, therefore tension measurement data was applied for the back analysis. There were long periods in between measurements and the manual measurements could have introduced some bias. According to Brox and Newcomen (2004), *"high wall strains may be subjected to a maximum strain of 0.6% to 1% before moving from a regressive mode to a progressive mode of failure. Strains above 1% may lead to abrupt failure".*

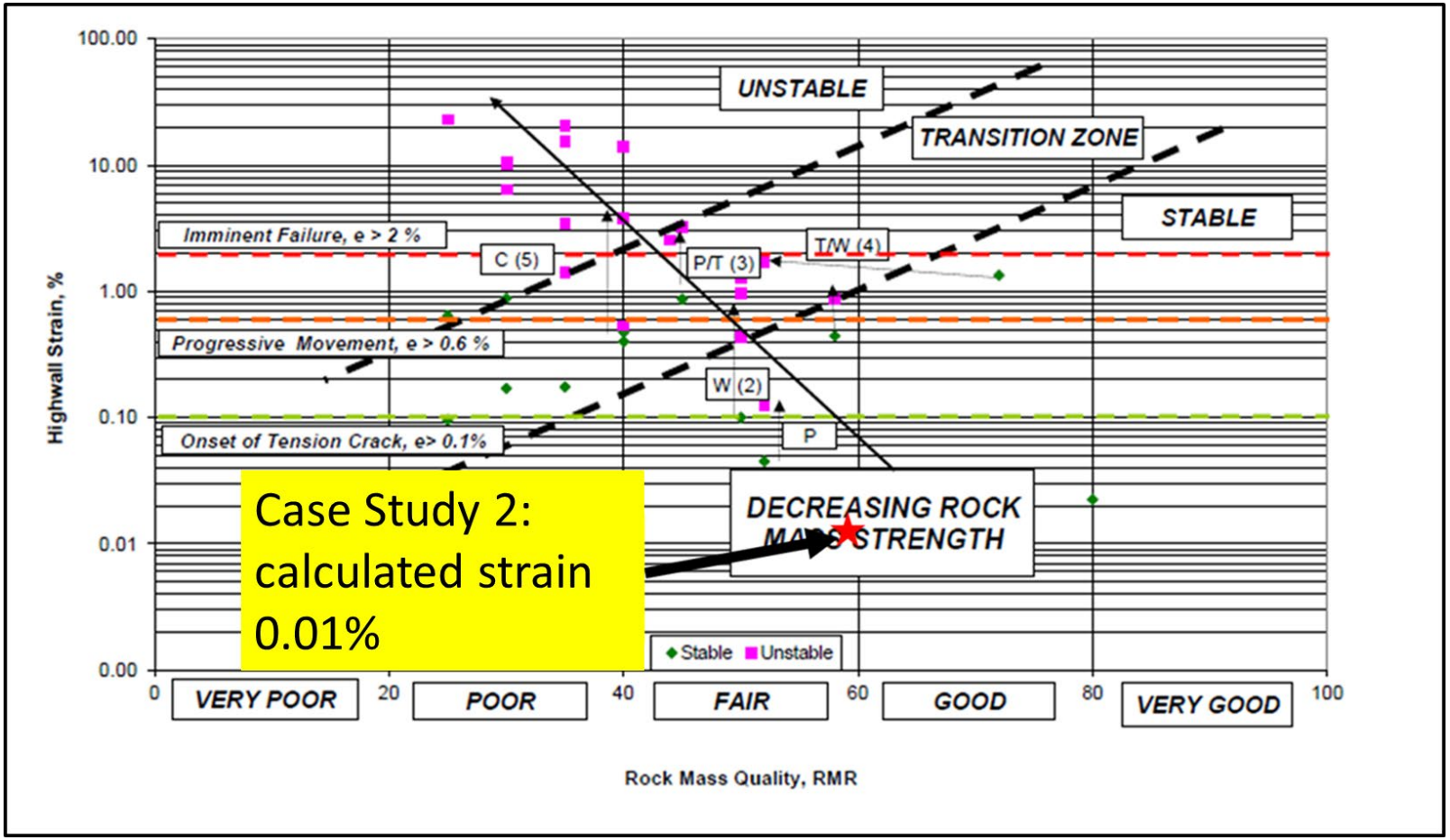


Figure 4-10: Case Study 1 High Wall Strain vs. RMR plot for the Husab Mine data (Adapted from Brox and Newcomen, 2004)

4.1.2 Case study 2: 30 November 2020 failure

On the 30th of November 2020, a bench-scale failure (15 m high wall) was recorded in the Domain D area. The failure was induced by mining activities associated with loading in the area of the failure, the preceding week. At the time of failure, a slope stability ground-based radar was stationed on the opposite end of the pit perimeter (at an approximate distance of 560 m) to monitor the Domain D slope (Figure 4-11). The failure mechanism was structurally controlled, involving a wedge. A catchment fence of 150 m in length has been installed along the failure area as a risk mitigation measure.

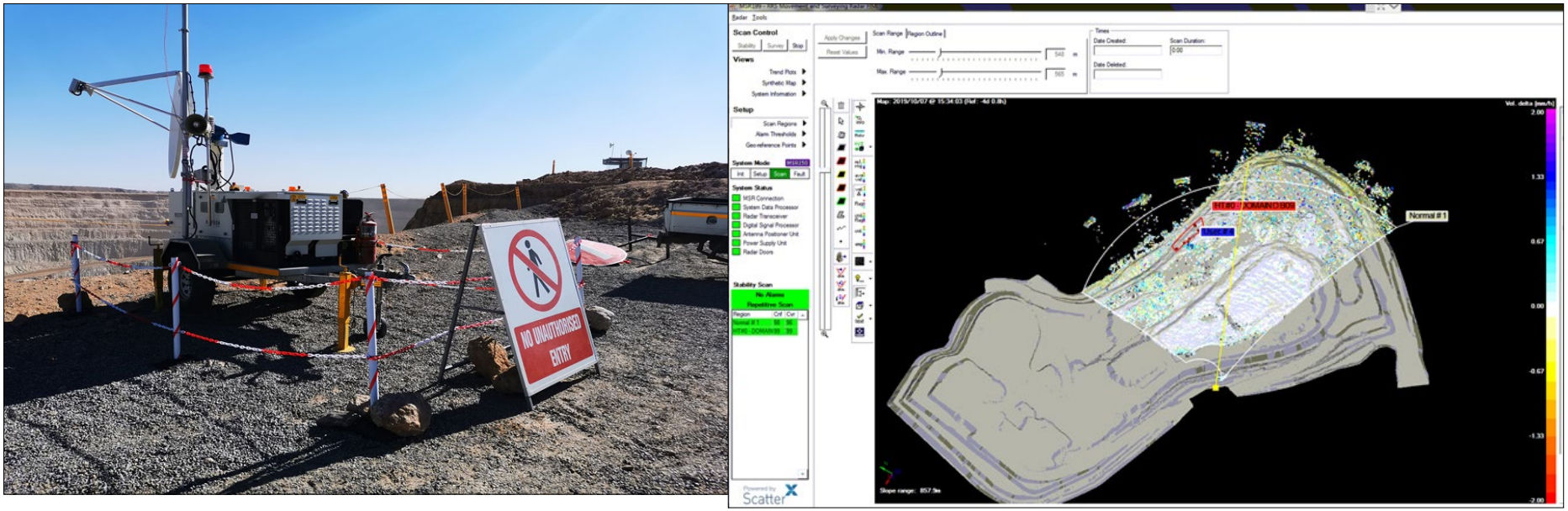


Figure 4-11: Reutech Ground-based RAR, monitoring Geotechnical Domain D (Zone 1 Husab Mine)

The available data that was obtained from the ground based radar (Reutech RAR - Radar) was for 6 days leading to the failure, from the 24th of November 2020 to the 30th of November 2020. The dataset that could be downloaded from the radar was limited as most of it had been automatically deleted from the system due to space constraints. The highwall strain was calculated to be 3.93% (Table 4-3) and is plotted in Figure 4-12 using the same RMR value calculated for the previous fall of ground (FOG). The results fit in well with the work done by Brox and Newcomen, 2004

Figure 4 - 13 shows the cumulative displacement data for the days leading to failure. An exponential increase in deformation is evident from the 27th of November 2020 leading to the day of failure. The deformation was towards the pit, indicating slope failure.

Table 4-3: Strain (%) calculated for the November 2020 failure

Deformation	Maximum Deformation of the high wall (m)	Height of the high wall (m)	Calculated Strain ε (%)
Cumulative Deformation at Failure	0.59	15	3.93

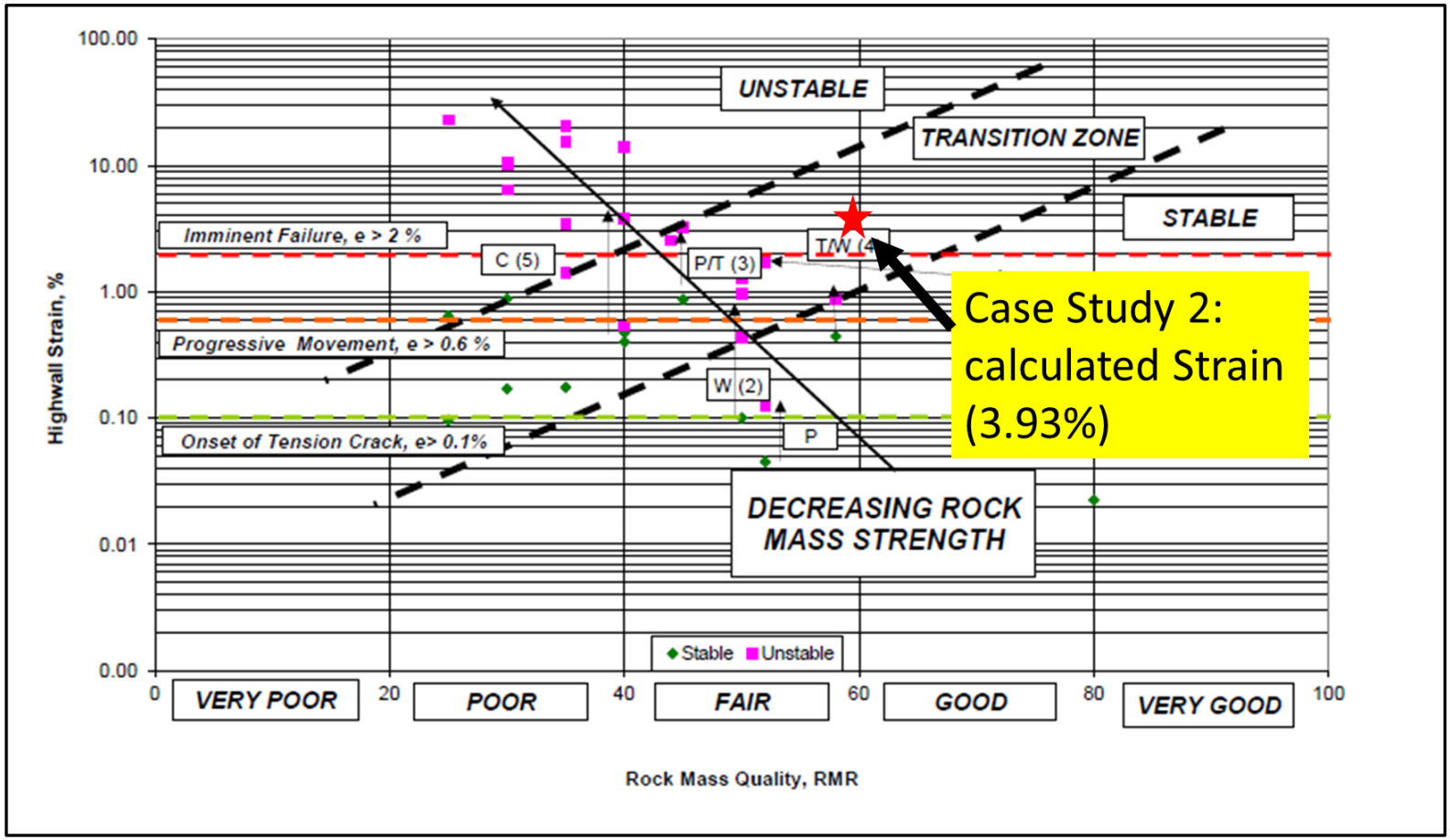


Figure 4-12: Case Study 2 High Wall Strain vs. RMR plot for the Husab Mine data (Adapted from Brox and Newcomen, 2004)

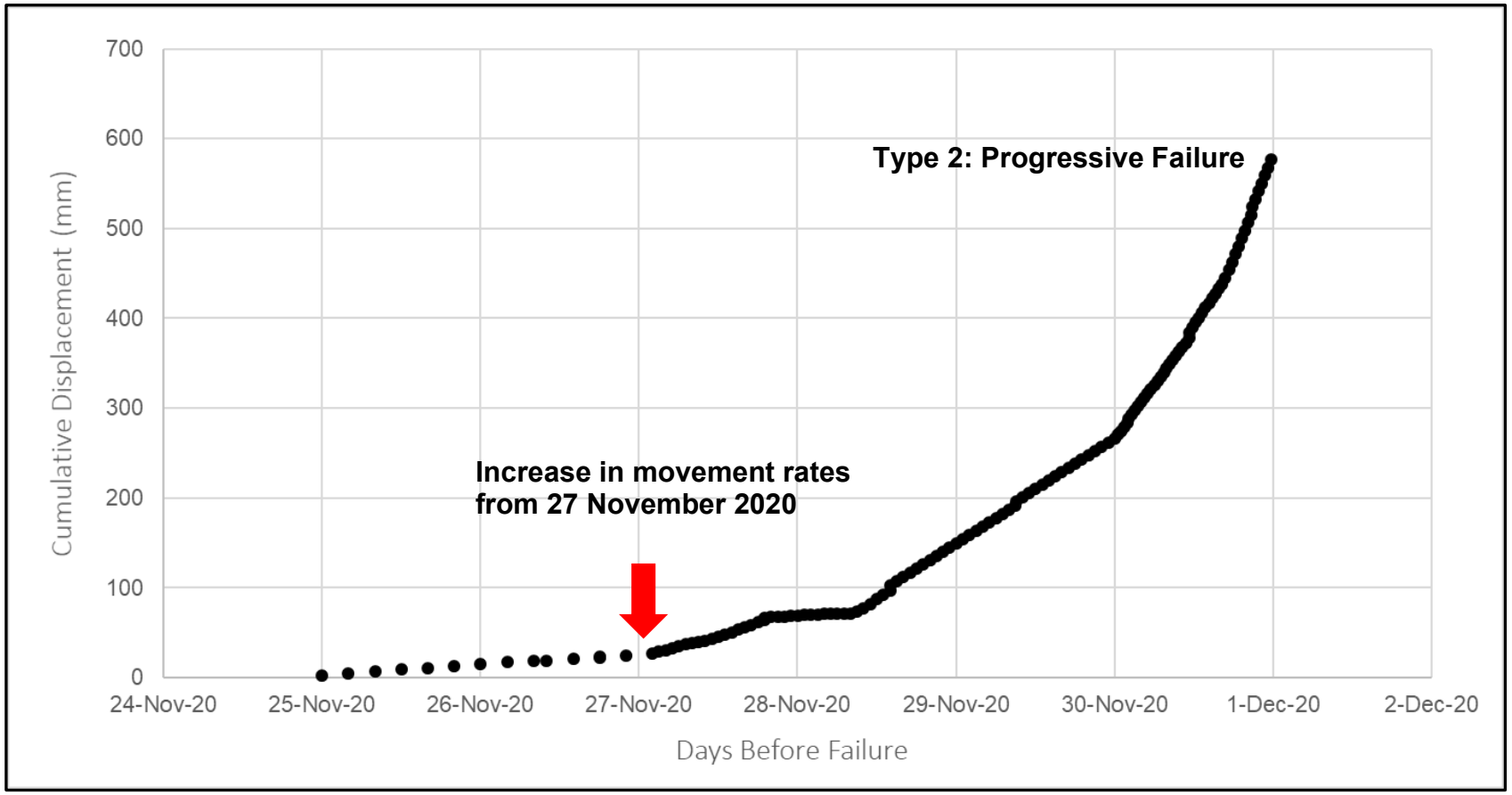


Figure 4-13: Cumulative Displacement vs. Days before failure – November 2020 failure

The following slope failure predictive tools were applied to the dataset, i.e. displacement, cumulative displacement, velocity and inverse velocity. Displacement data is measured by comparing the back-scattered microwave signals between two successive acquisitions (Carlá et al., 2017). Figure 4-14 shows the velocity data against time, it is evident in this analysis that there was an increase in velocity from the 27th of November 2020, up until the 29th of November 2020, one day before failure (as shown with the red dotted line). The velocity data is not as convincing as the cumulative displacement data. The inverse velocity data presented in Figure 4-15 shows that the failure was predicted on or before the 30th of November 2020.

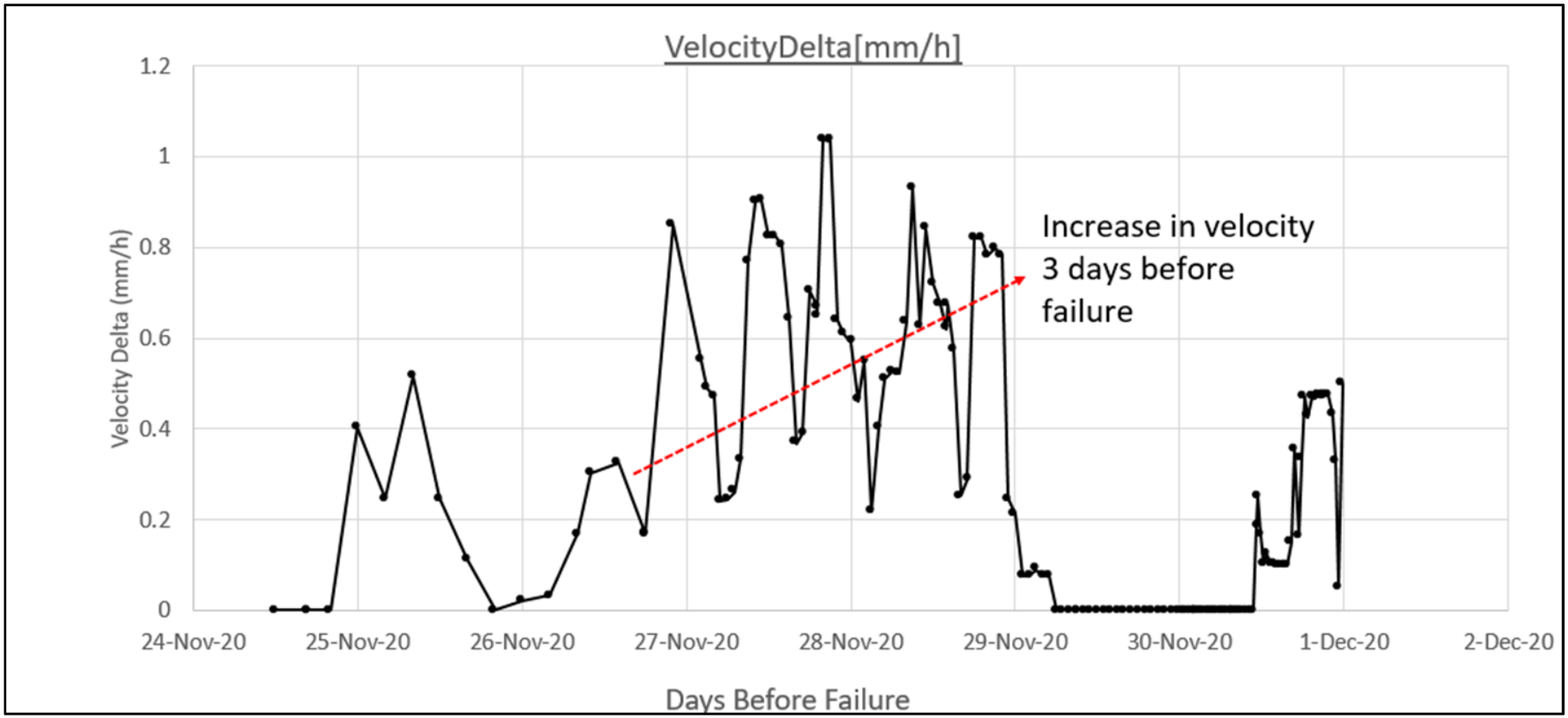


Figure 4-14: Velocity Delta vs. Time – November 2020 Failure

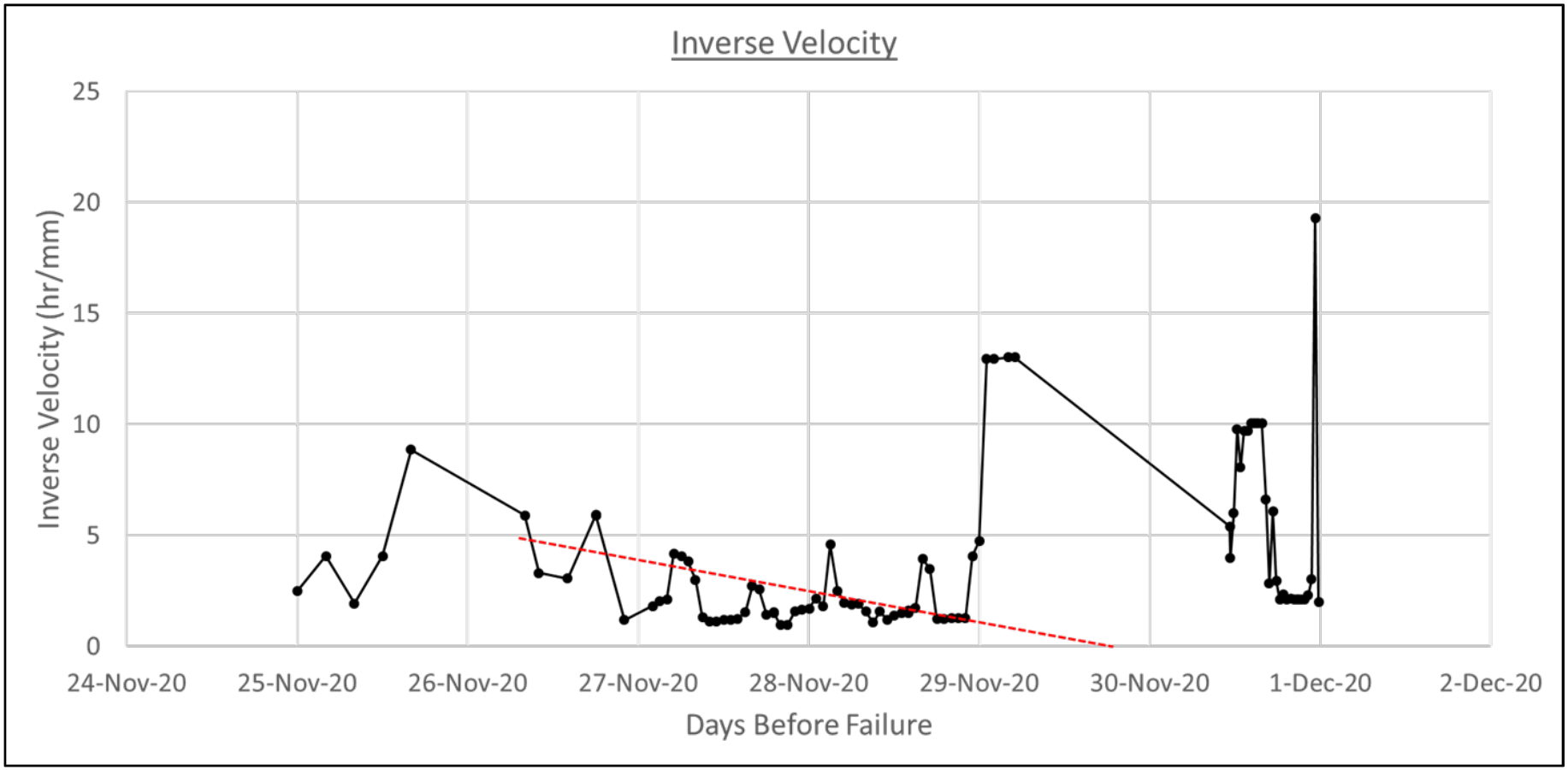


Figure 4-15: Inverse velocity vs. Time - November 2020 failure

4.1.3 Case study 3: 20 August 2021 failure

On the 25th of August 2021, a multi-bench failure (30 m high wall) occurred in the Domain D area. At the time of this failure, there were loading activities close to the area under review.

InSAR data analysis

Husab Mine has contracted (SkyGeo) for InSAR monitoring of the project area. Satellite monitoring is carried out over the two pits, dumps and tailings facility. SAR satellites orbit the earth in two trajectories; descending orbit (orbit the earth from the North to the South Pole) and Ascending orbit (orbit the earth from the South to the North Pole) (Sartorelli and Scoular, 2022).

The TerraSAR–X satellite is used for descending orbit over the Husab Mine site. One orbit is used over the site to increase sensitivity to displacement on some slopes. The TerraSAR-X satellite has precision of 1 mm (Sartorelli and Scoular, 2022). Data is measured in horizontal direction towards the pit.

The data is reported in two formats; coherence and displacement. Coherence is a measure of the local spatial correlation between two SAR acquisitions, a decrease in coherence data is an indication of phase noise. Displacement refers to movement of the ground surface, increase in displacement rate is a cause of concern and requires further investigation (Sartorelli and Scoular, 2022).

Figure 4 - 16 shows the cumulative displacement data for the time period from the 18th of August 2020 to the 18th of August 2021. The average velocity rate presented in Figure 4-17, shows increase in velocity rates towards the failure date. The inverse velocity data presented in Figure 4 -18 does not show any indication of failure prediction. The order of the magnitude of the data presented in the cumulative displacement and velocity graphs is very small compared to the results presented in Case Studies 2 and 3. Figure 4 - 19 shows the InSAR results plotted on a plan of the pit. The analysed horizontal deformation data was taken from the black dot in the centre of the highlighted rectangle.

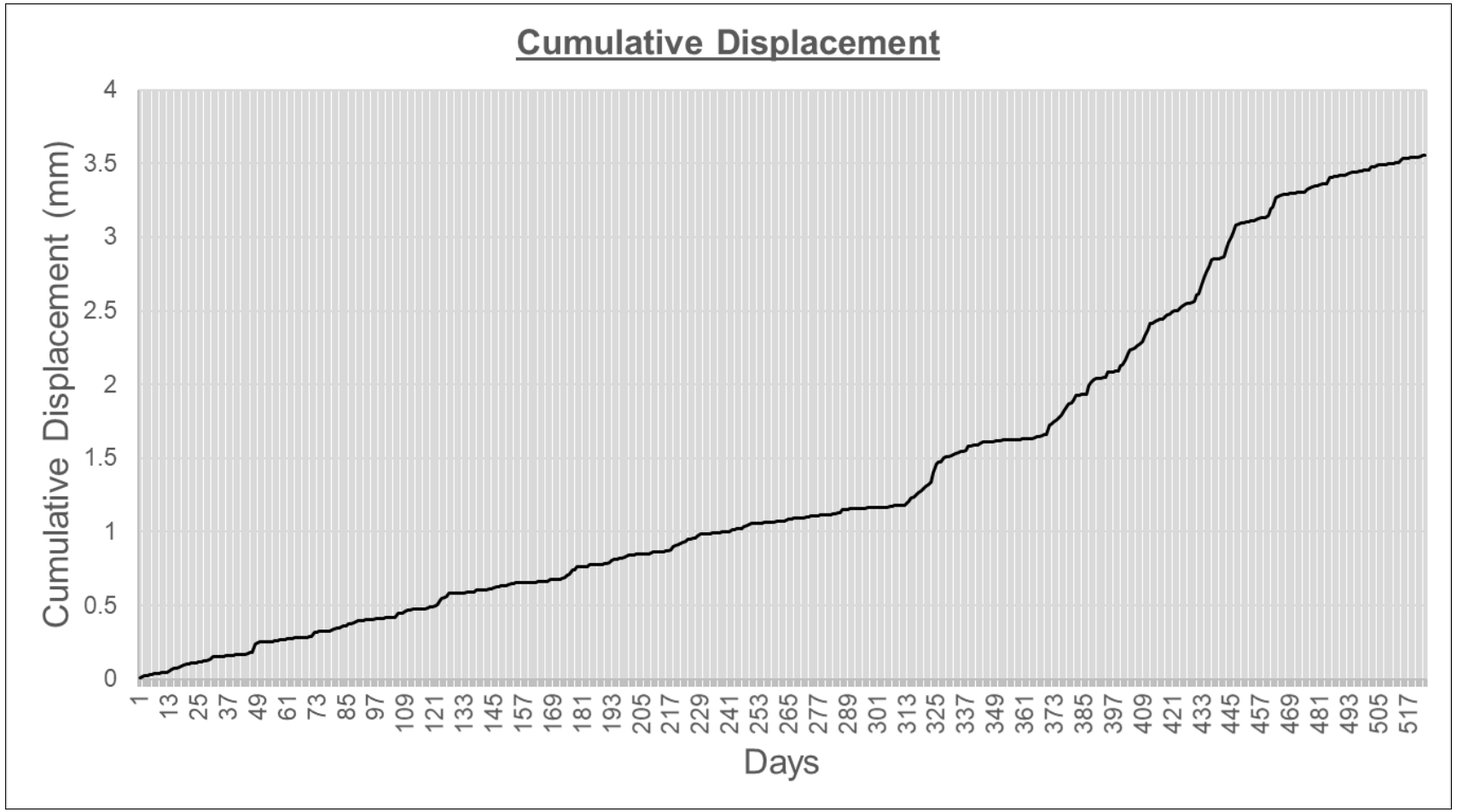


Figure 4-16: InSAR Cumulative displacement over the time period – August 2020 to August 2021

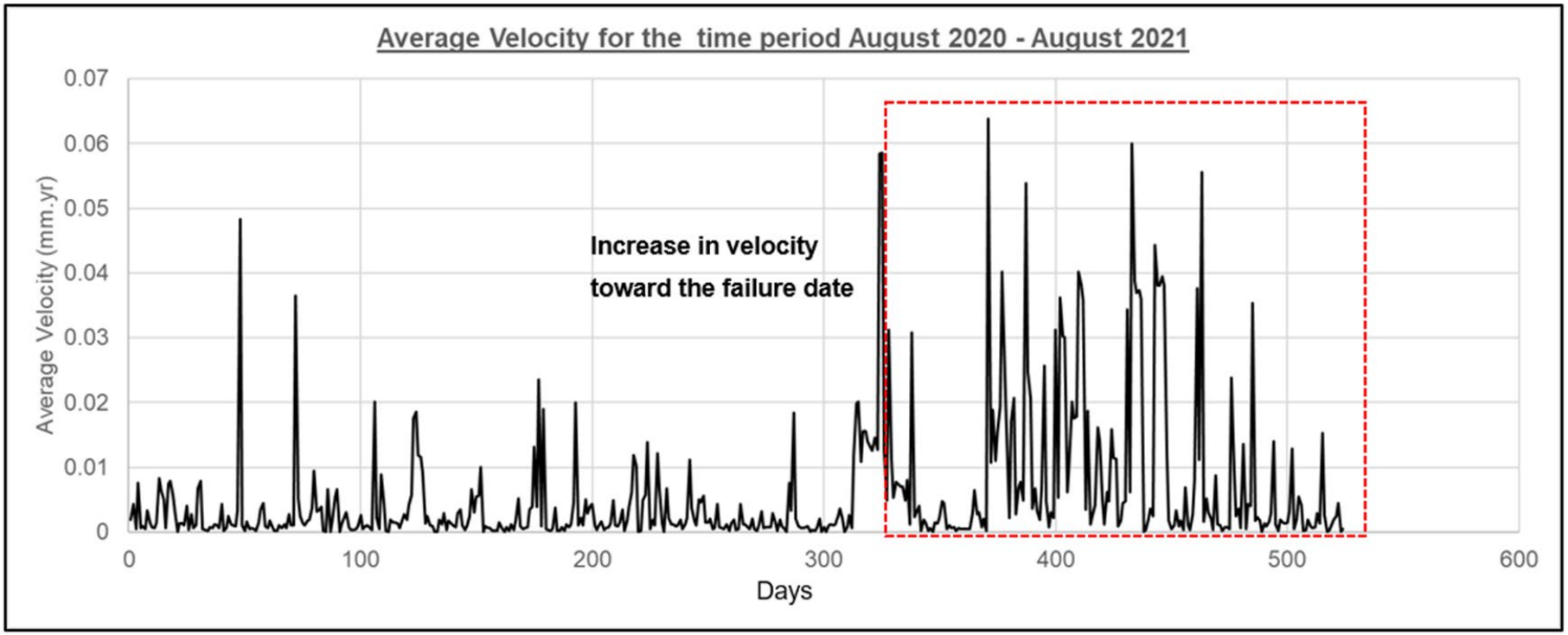


Figure 4-17: InSAR Average Velocity data before failure time – data from the time Period August 2020 to August 2021

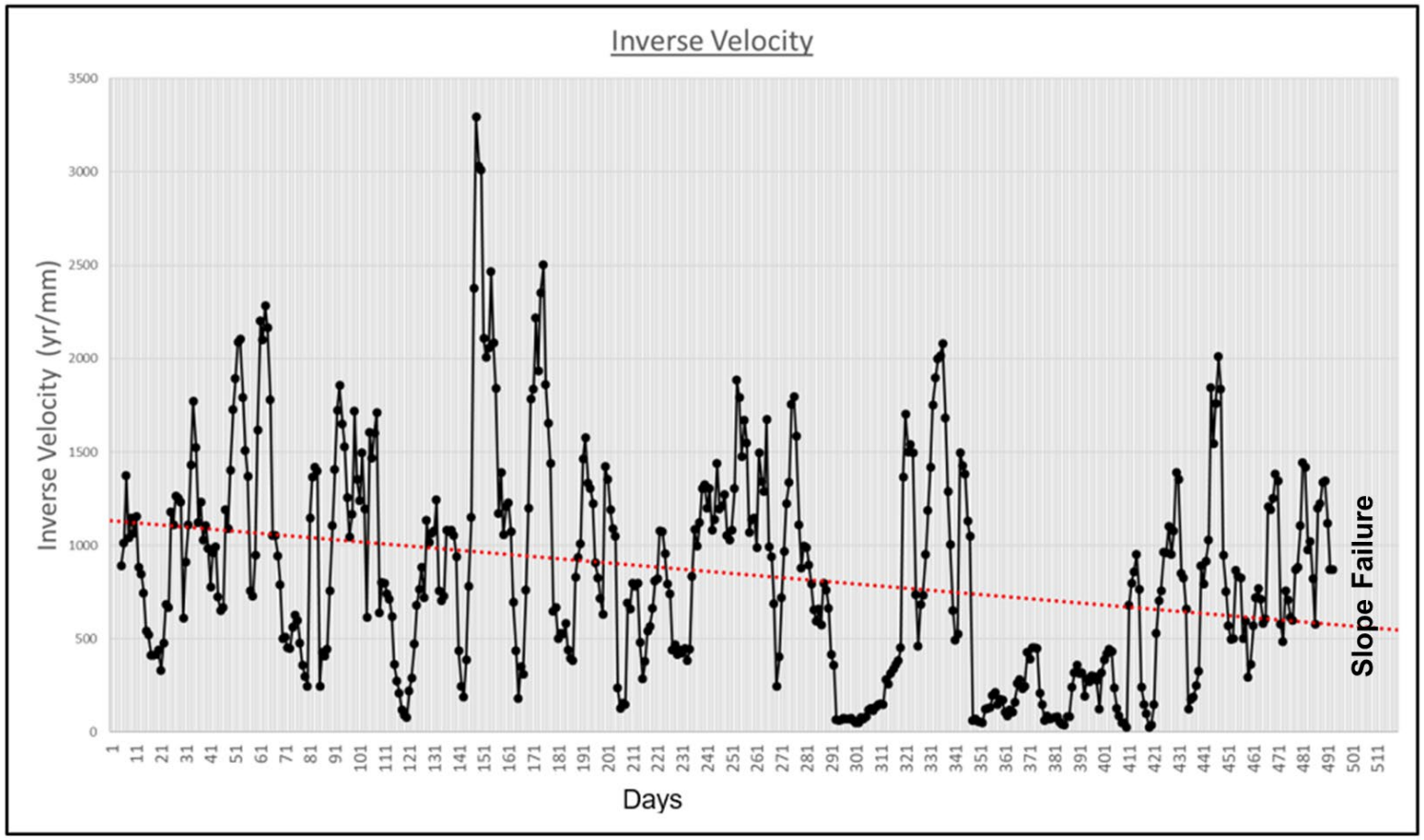


Figure 4-18: InSAR Inverse velocity data for the Time period – August 2020 to August 2021

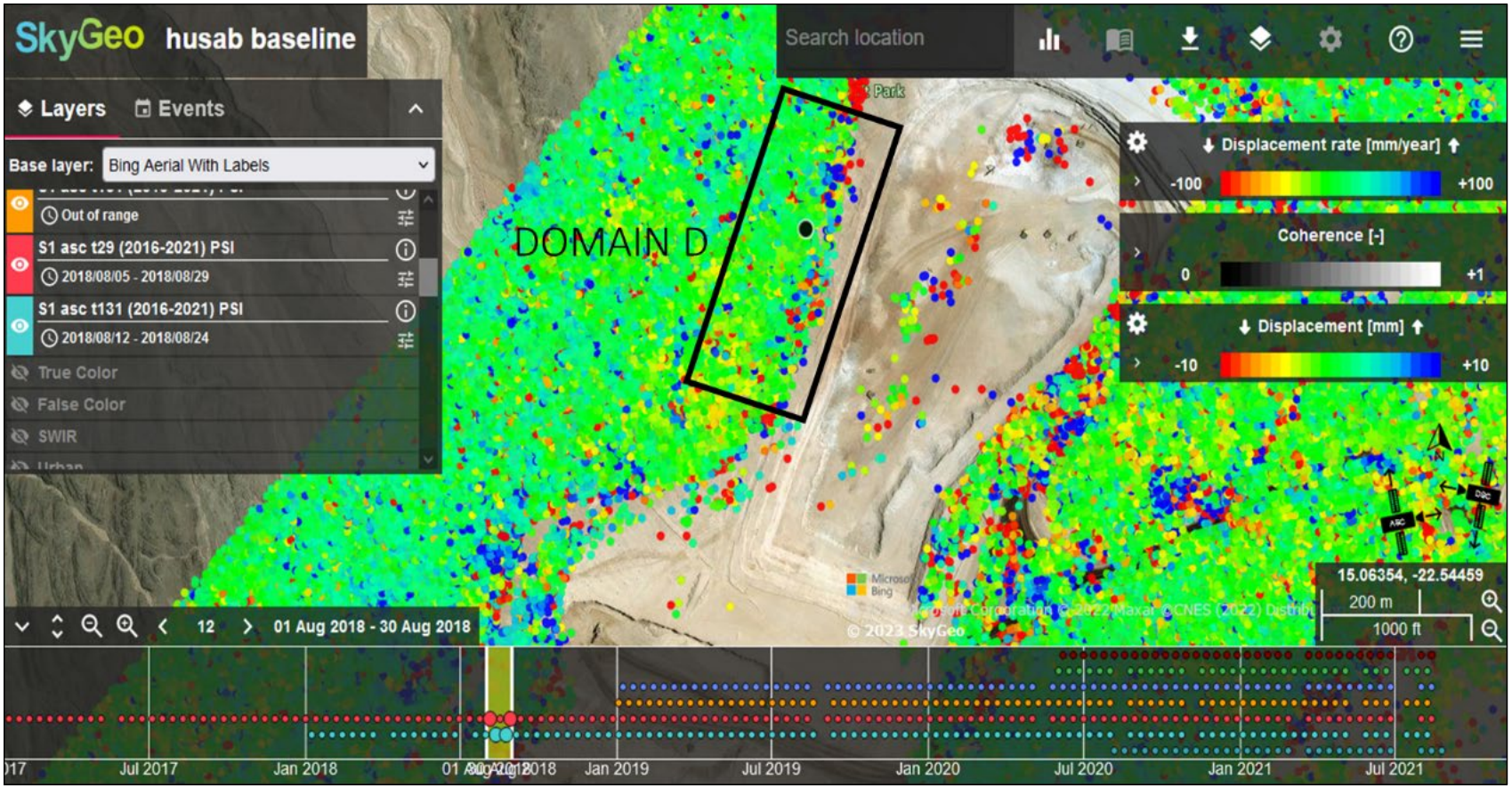


Figure 4-19: InSAR (Husab Mine Baseline Data - supported by SkyGeo). The horizontal deformation data was taken at the position of the black dot in the highlighted triangle

The highwall strain was calculated to be 0.0117% and is plotted in Figure 4-20 using the same RMR value calculated for the previous fall of ground (FOG). The results do not correlate with the work done by Brox and Newcomen, 2004.

Table 4-4: Strain (%) calculated for the August 2021 failure

Deformation	Maximum Deformation of the high wall (m)	Height of the high wall (m)	Calculated Strain ε (%)
Cumulative Deformation at Failure	0.035	30	0.0117

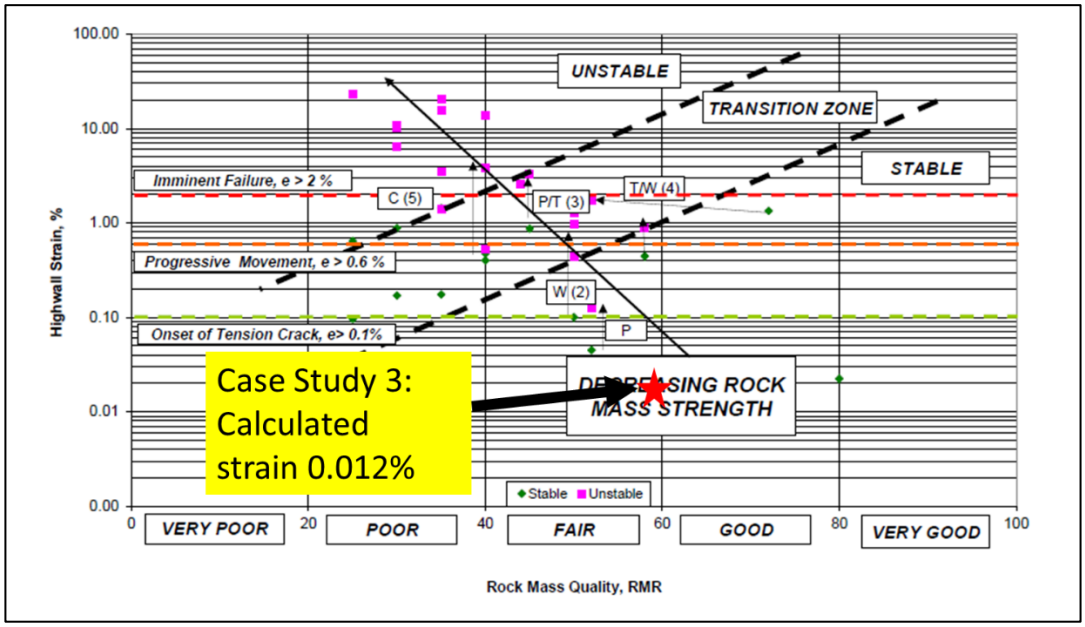


Figure 4-20: Case Study 3 High Wall Strain vs. RMR plot for the Husab Mine data (Adapted from Brox and Newcomen, 2004)

4.1.4 Case study 4: Rössing uranium mine

On the 31st of July 2020, a multiple-bench (approximately 56 m of slope height) failure occurred in the neighbouring Rössing Uranium Open pit mine (Figure 4 – 21). The failure was an eastern extension of another failure that occurred on the 21st November 2011. The failure was triggered by rainfall (11.6 mm of rainfall was received on the 20th of April 2020). Before the rainfall event on 20 April 2020, the area was moving at a steady rate of about 0.3 mm/day but accelerated to about 2.5 mm/day immediately after the rain and continued to accelerate until the day of failure. The type of failure mechanism and structures that contributed to failure were not provided in the report. The back analysis involved a review of one prism data (Horizontal displacement data) for a two-year period prior to the failure (19 July 2018 to 31 July 2020). Figure 4-22 shows the cumulative displacement data. The results of the Brox and Newcomen (2004) analysis is shown in Figure 4-23, suggest that the slope was under progressive movement as the high wall strain was 1.6% at the time of failure. It is evident from the displacement graph that the deformation shows a classical Type 2 progressive deformation. The data presented in Figure 4 - 24, shows a sharp increase in velocity from the 20th of April 2020, indicating that the 11.6 mm rainfall received on that day, triggered the failure. The inverse velocity data in Figure 4-25 shows that the failure was predicted before the 31st of July 2020.



Figure 4-21: Failure in the Rössing Uranium Mine Open Pit – 31 July 2020

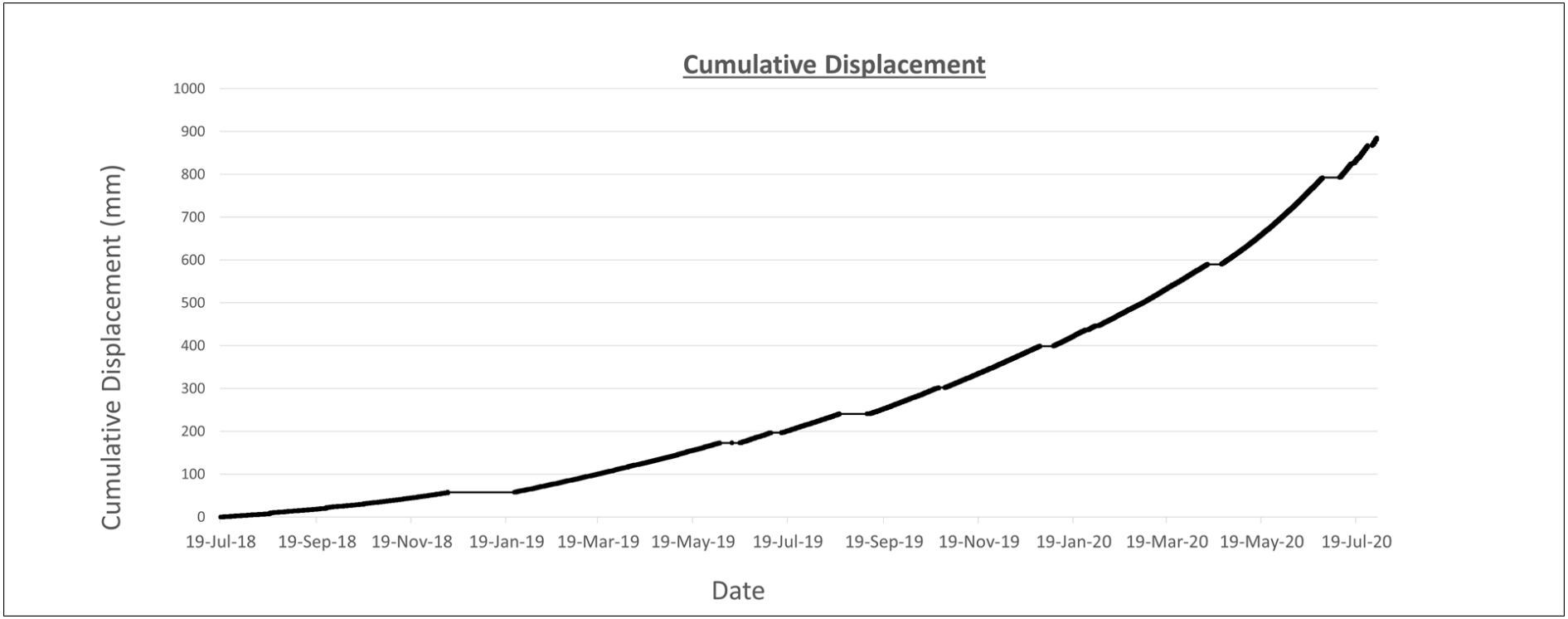


Figure 4-22: Cumulative Displacement data from 19 July 2018 to 19 July 2020 (Rössing Uranium Mine)

Table 4-5: Strain (%) calculated for the Rössing Uranium Mine failure (July 2020)

Deformation	Maximum Deformation of the high wall (m)	Height of the high wall (m)	Calculated Strain ε (%)
Cumulative Deformation at Failure	0.9	56	1.6%

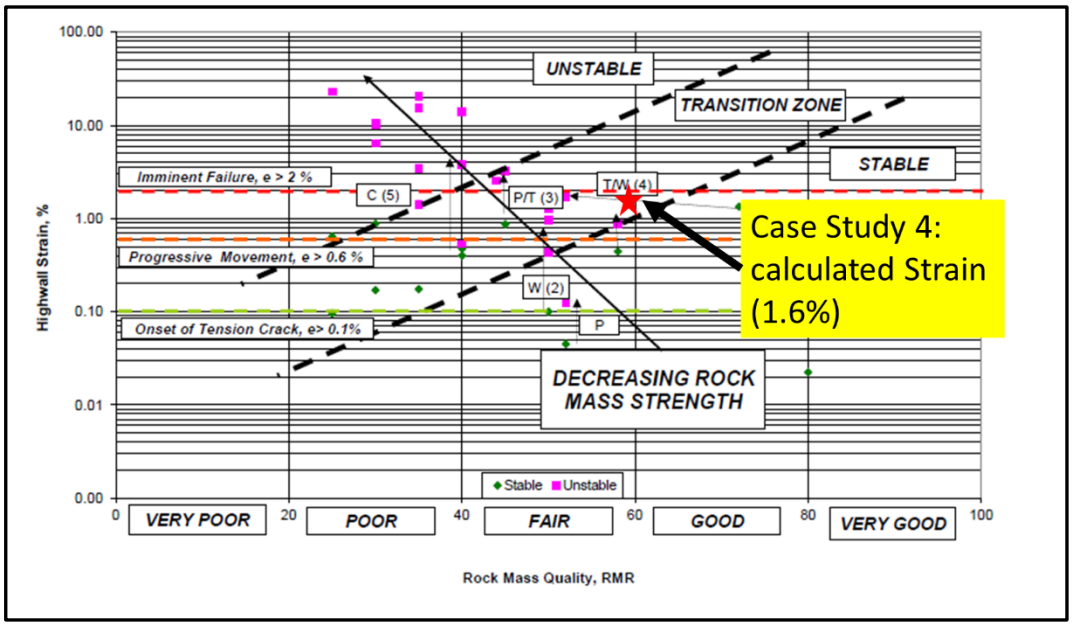


Figure 4-23: Case Study 3 High Wall Strain vs. RMR plot for the Rössing Mine data (Adapted from Brox and Newcomen, 2004)

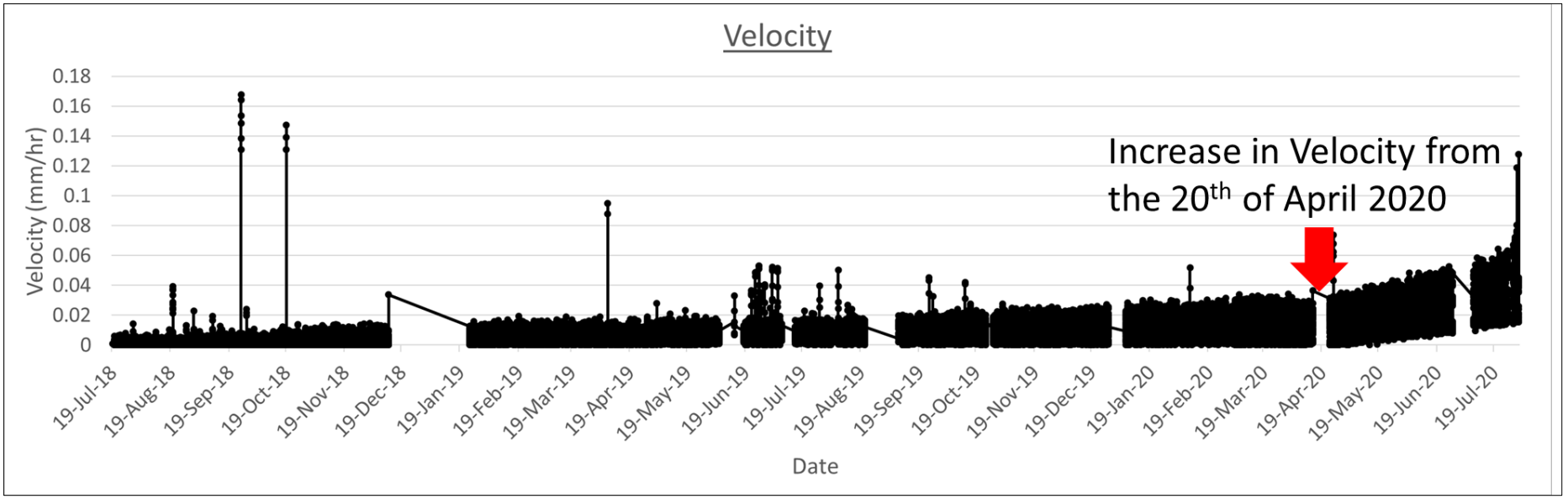


Figure 4-24: Velocity data from 19 July 2018 to 19 July 2020 (Rössing Uranium Mine)

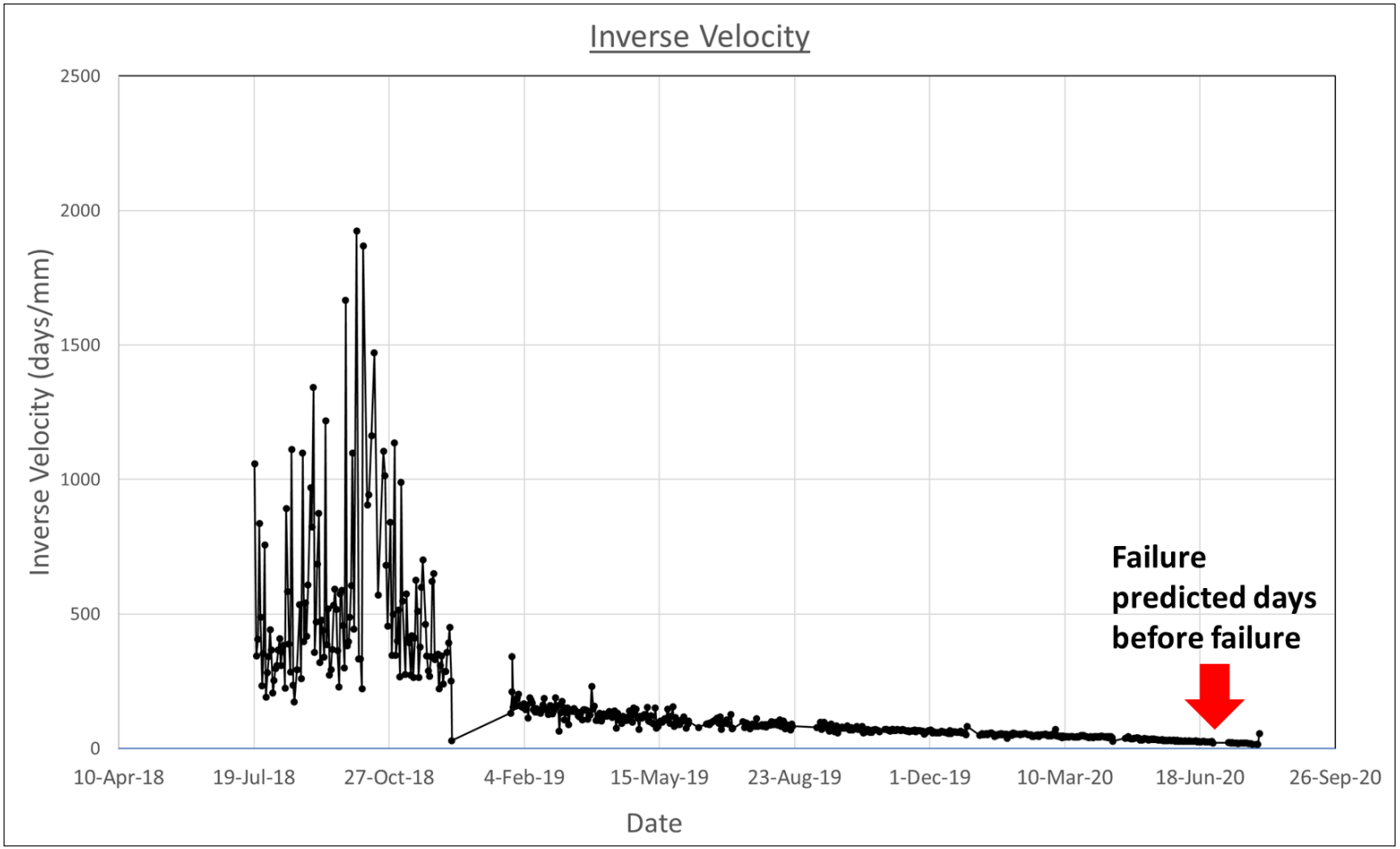


Figure 4-25: Inverse velocity data from 19 July 2018 to 19 July 2020 (Rössing Uranium Mine)

The SGM method was applied to the prism data, in an attempt to predict failure (Figure 4-26). Not all the analyzed data plotted within the safe region. Some predictions showed that failure would occur before the actual failure. It is evident from this analysis that the data is inconclusive and further trials should be considered to explore the applicability of the SGM method for slope failure prediction.

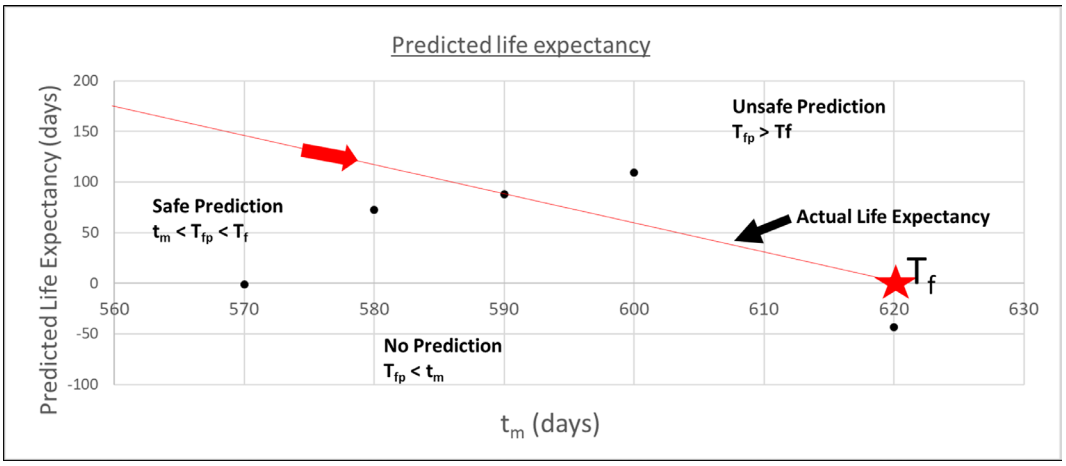


Figure 4-26: Slope gradient method applied to prism monitoring data from the Rössing Uranium Mine

4.2 Chapter Summary

4.2.1 Case study 1: August 2018 failure

Kinematic analysis work was carried out in the Rocscience Dips software. The failure mechanism based on structures that contributed to failure are as follows:

- Planar Failure (for all structures) – 50%;
- Planar failure (foliation planes) – 100%; and
- Wedge sliding – 100%.

Swedge analysis was carried using the Rocscience Swedge program to determine the FOS. The following input parameters were used Cohesion (0 KPa) and Friction angle (32°). The FOS result was 0.772, which satisfies the condition for failure to take place.

Tension crack data was utilised to determine the high wall strain at the point of failure. Two tension cracks with the highest displacement before failure of 4 mm and 2 mm were utilised. The calculated strain based on a 15 m high wall, referring to Equation 2-1 is 0.02% and 0.01%.

The quality of the rock mass was calculated based on the Bieniawski RMR classification system. Scanline mapping data was used to determine the properties of the discontinuities. Lab test data based on the feasibility tests and 2017 study was used to determine the average UCS value for the rock, considering the Rossing Formation is variable. The final calculated result for RMR is 59, which implies the rock mass is fair. The high wall strain results were plotted against the RMR, on the Brox and Newcomen diagram (2004). The final result plots within a stable region of the Brox and Newcomen diagram, which is not in agreement with the Brox and Newcomen (2004) criteria. The contributing factor to the discrepancy could be the long time periods between tension crack measurements. Deformation before failure was not measured.

4.2.2 Case study 2: November 2020 failure

Similar to the work done for Case Study 1, the high wall strain was calculated, and the result was 3.93% strain. Utilising the same RMR as the previous FOG, the strain was plotted against the RMR on the Brox and Newcomen (2004) diagram. The results are in agreement with work done by Brox and Newcomen (2004). The calculated strain of 3.93% plots above the threshold of imminent failure.

The highest strain rate before failure was just above 1 mm/hr and the maximum cumulative displacement was 590 mm. Increase in movement rates is clearly observable 3 days before failure (as demonstrated in the cumulative and inverse velocity plots).

4.2.3 Case study 3: August 2021 failure

InSAR data sourced from SkyGeo was utilised for the back-analysis. The highest cumulative displacement is 4 mm. The order of magnitude does not correspond with the ground – based radar data. For the FOG presented in Case Study 2, the highest cumulative displacement before failure is 590 mm. The highest velocity before failure is just above 0.06 mm/yr, which is not comparable to the ground - based radar data results. The high wall strain was calculated based on the deformation data and plotted against the RMR value on the Brox and Newcomen diagram (2004). The results do not support the work done by Brox and Newcomen (2004).

4.2.4 Case study 4: Rössing uranium mine

The multiple-bench failure that occurred at Rössing Uranium Mine was triggered by 11.6 mm of rainfall that was received on the 20th of April 2020. This is evident in the Velocity plot presented in Figure 4-24, where there is an increase in velocity from the 20th of April 2020. The maximum velocity before failure was just above 0.12 mm/hr. The failure was predicted days before failure (Figure 4-25). The high wall strain was calculated at 1.6%, the result was plotted on the Brox and Newcomen diagram, assuming a RMR of 59. The result plots within the progressive movement region, which agrees with the work done by Brox and

Newcomen (2004). The results presented in this case study, are in agreement with the Case Study 3 (November 2020 Husab mine Domain D failure) (deformation data was captured by the ground-based RAR).

4.3 Discussion

A good correlation exists between the November 2020 failure (Ground – based radar data) and the Rössing Uranium mine data. Based on the Inverse velocity and velocity data (shown in Figure 4-14, Figure 4-15, Figure 4-24 and Figure 4-25), 2 to 3 days of consecutive acceleration is safe warning before failure can take place.

The cumulative displacement data shown in Figure 4-13 and Figure 4-22, show that both failures i.e., November 2020 failure and the Rössing Mine failure were progressive. This type of failure allows enough time for geotechnical engineers and operations management to be proactive in implementing remedial actions to minimise economic losses and potential injuries to mine personnel. The onset of failure for the November 2020 failure was 3 days before failure as shown in Figure 4-13. However, the onset of failure for the Rössing Uranium mine failure is not very clear from the cumulative displacement plot. Figure 4-27 is a plot of the strain versus time behaviour of rock. The November 2020 failure has the highest strain rate of 3.96%, followed by the Rössing Mine failure with a strain rate of 1.6% and finally the August 2018 failure has a calculated strain rate of 0.02%.

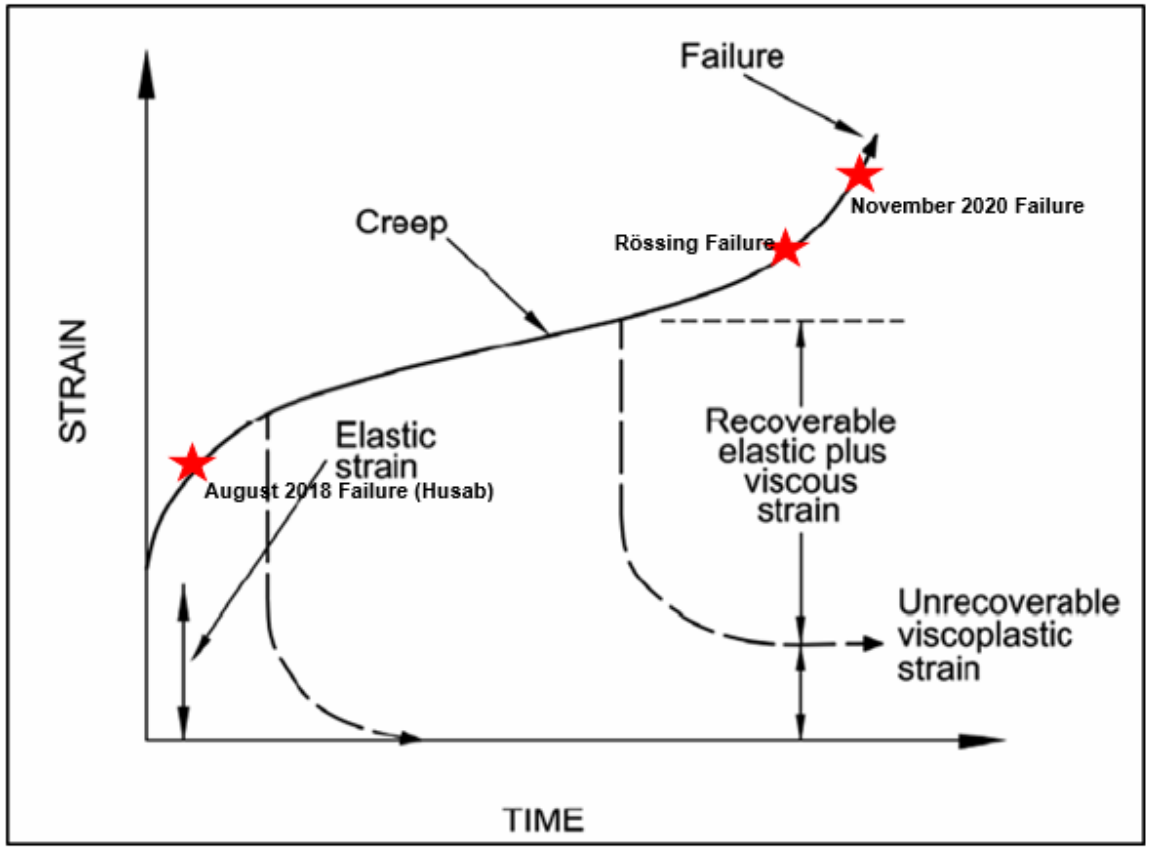


Figure 4-27: Strain versus Time graph behaviour of rock, the November 2020 failure, Rössing mine failure and August 2018 failure are plotted based on their strain values at failure (Adapted from Sullivan, 2007)

5 CONCLUSIONS AND RECOMMENDATIONS

5.1 Introduction

The unfavourable orientations of foliation planes relative to the pit geometry have been a main contributor to recurring planar and wedge bench-scale failures in geotechnical Domain D. The primary objective of the research was to determine if there is a warning period before slope failure at the Husab mine.

5.2 Research Contributions

The research has provided a better understanding of slope movements at the mine. From the results, which includes data from an adjacent mine, it appears that failure prediction may be possible in the future, if more comprehensive data can be collected. However, the available data was insufficient to make conclusive findings. Algorithms may also be established to provide automated warnings. Such warnings will reduce the risk of unexpected failures and thus improve uncertainty. Unknown failure-behavioural patterns or insufficient data leads to excessive waiting time periods to cater for the undefined behaviour. A neighbouring Mine provided data for one prism that was used to carry out a back-analysis on a failure that occurred in 2020 on that mine. The quality of the data provided was good and consistent over a two-year period. This data was clearly able to predict failure. In conclusion, it appears that failure could have been predicted at least 2 to 3 days before the slope-failure occurred with the application of the following predictive methods:

- cumulative displacement;
- velocity and;
- inverse velocity.

5.3 Research Limitations

5.3.1 Case study 1: 5 October 2018 failure

At the time of failure, there were no slope monitoring systems in place. The only means of monitoring was through manual tension crack measurements. Insufficient data was collected, particularly towards the date of failure. The period between data points was too long and data was lost.

5.3.2 Case study 2: 30 November 2020 failure

Due to limited storage space on the radar, insufficient data was available to determine the long-term deformations. Although the data collected just prior to failure was sufficient, the long-term data was missing.

5.3.3 Case study 3: August 2021 failure

InSAR data was used for the back-analysis work. The failure was clearly observable, but the deformations appear to be wrong. Although data was provided for a whole year (August 2020 to August 2021), no dates were provided.

5.3.4 Recommendations for future research work

The following recommendations came from the research project:

- More work should be carried out on any future FOGs at the site. For this purpose, bigger data-storage facilities are recommended.
- Algorithms should be developed from the findings of this and future research to enable automated warnings, based on monitoring data.
- The acquisition of comprehensive backup systems for all monitoring data is very useful for back analysis work.

REFERENCE LIST

Agisoft, 2023. Available at: *www.agisoft.com.* [Accessed 23 October 2023].

Amini, M., Majdi, A. and Veshadi, M.A. 2012. Stability Analysis of Rock Slopes against Block – Flexure toppling failure. *Rock Mech Rock Eng,* Volume 45. pp. 519 – 532.

Armstrong, R. and Maduray, C. 2018. Husab Mine – Geotechnical Design Review. SRK Consulting Report Number: 469305/07.

Armstrong, R. and Maduray, C. 2022. Husab Mine – Geotechnical Design Review. SRK Consulting Report number: 585456/01.

Barton, N. 2002. Some new Q-value correlations to assist in site characterization and tunnel design. *International Journal of Rock Mechanics and Mining Sciences,* Volume 39. pp. 185 – 216.

Brox, D. and Newcomen, W. 2004. "Utilizing strain criteria to predict highwall stability performance", *Canadian Institute of Mining and Metallurgy and Petroleum,* pp. 1 – 8. Available at: One Mine portal: One Mine Digital Library. [Accessed 21 October 2023].

Carlá, T., Farina, P., Intrieri, E., Botsialas, K. and Casagli, N. 2017. On the monitoring and early warning of brittle slope failures in hard rock masses: Examples from an open pit mine. *Engineering geology*, Volume 228. pp. 71 – 81.

Carlá, T., Farina, P., Intrieri, E., Ketizmen., H. and Casagli, N. 2018. Integration of ground- based radar and satellite InSar data for the analysis of an unexpected slope failure in an open pit mine. *Engineering geology*, Volume 235. pp. 39 – 52.

Dey, J., Roy, S. and Matin, A. 2021. "Drone Photogrammetry: Structural data gathering tool for open pit mining geotechnics", *SSIM,* pp. 135 – 148. Available at: Australian Centre for Geomechanics. [Accessed 23 October 2023].

Dick, G.J. 2013. *Development of an early warning Time-of-Failure analysis methodology for open pit mine slopes utilizing the spatial distribution of ground-based radar monitoring data*. PhD thesis, The University of British Columbia (Vancouver). Available at: Canadian Science Publishing. [Accessed 21 October 2023].

DJI, 2023. Available at: https://www.dji.com. [Accessed 23 October 2023].

Farina, P., Leoni, L., Coppi, F., Babboni, F., Mayer, L., Coli, N., Helbawi, A., Weaver, A. and Preston, C. 2009. "Monitoring Open Pit Slopes through Slope Monitoring Radar Based on Synthetic Aperture Radar". *Canadian Rock Mechanics Symposium,* pp. 337 – 343. Available at: One Mine portal: One Mine Digital Library. [Accessed 21 October 2023].

Farina, P., Bardi, F., Lombardi, L. and Gigli, G. 2020. "Combining Structural data with monitoring data in open pit mines to interpret the failure mechanism and calibrate radar alarms", *Proceedings of the 2020*

International Symposium on Slope Stability in Open Pit Mining and Civil Engineering, pp. 524 – 534. Available at: Australian Centre for Geomechanics Portal. [Accessed 21 October 2023].

Federico, A., Popescu, M., Elia, G., Fidelibus, C., Internò, G. and Murianni, A. 2012. Prediction of time to slope failure: a general framework. *Environ Earth Sci,* Volume 66. pp. 245 – 256.

Gibson, W.H., de Bruyn, I.A. and Walker, D.J.H. 2006. "Consideration in the optimisation of Bench Face Angle and Berm Width Geometries for open pit mines", *International Symposium on Stability of Rock Slopes in Open pit mining and Civil Engineering.* pp. 557 – 578. Available at: One Mine portal: One Mine Digital Library. [Accessed 21 October 2023].

Gigli, G., Lombardi, L., Carlá, T, Beni, T. and Casagli, N. 2022. A method for full three-dimensional kinematic analysis of steep rock walls based on high-resolution point cloud data*. International Journal of Rock Mechanics and Mining Sciences.* Volume 157*.* pp. 1 – 14. Available at: Science Direct portal: Science Direct Digital Library. [Accessed 21 October 2023].

Golder Associates Africa, 2010. Report Number: 12751 – 9890 – 2. Rossing South Bankable Feasibility Open Pit Design.

Google Earth., 2023. Available at: https://earth.google.com/web/. [Accessed 23 October 2023].

Gottlander, J. 2019. *Evaluation of methods for rock mass characterization and design of rock slopes in crystalline rocks.* MSc thesis, Royal Institute of Technology School of Architecture and the Built Environment. Available at: https://kth.diva-portal.org. [Accessed 21 October 2023].

Gui, J.Y., González-Fernández, M.A, Estévez-Ventosa, X., Song, F. and Alejano, L.R. 2023. Toppling susceptibility of a single rock block resting on a regularly rough *base*. *Engineering Geology,* Volume 313. pp. 1 – 24.

Harries, N. and Pritchett, H. 2009. “Application of Slope Stability Radar for improved safety and productivity in the global mining industry”, *SME Annual Meeting,* pp. 1 – 3. Available at: One Mine portal: One Mine Digital Library. [Accessed 21 October 2023].

Henschel, M.D., Sato, S., Ahola, R. and McFarland, M.A. 2014. “Designing Interferometric Synthetic Aperture Radar Surveys for Mine Monitoring with Accuracy Assessment”, *AUSRock 2014: Third Australasian Ground Control in Mining Conference / Sydney, NSW,* pp 233 – 237. Available at: One Mine portal: One Mine Digital Library. [Accessed 21 October 2023].

IDS GeoRadar. 2022. IBIS – FL. [online]. Available at: <https://idsgeoradar.com/products/interferometric-radar/ibis-fl> [Accessed 18 January 2022].

Inwood, N., Le Brun, S., Craig, S., Cheyne, R., Valenta, M., Browner, H. and Amos, S. 2011. National Instrument 43-101 Technical Report. Report number: MineWPER00713AE.

Jakubec, J. and Laubscher, D.H. 2000. “The MRMR Rock Mass Rating Classification System in Mining Practice”, *MassMin,* pp. 413 - 421. Available at: One Mine portal: One Mine Digital Library. [Accessed 23 October 2023].

Johari, A. and Lari, M. 2016. System reliability analysis of rock wedge considering correlated failure modes using sequential compounding method. *International Journal of Rock Mechanics and Mining Sciences*, Volume 82. pp. 62 – 70.

Kardani, N., Zhou, A., Nazem, M. and Shen, S.L. 2021. Improved prediction of slope stability using a hybrid stacking ensemble method based on finite element analysis and field data. *Journal of Rock Mechanics and Geotechnical Engineering*, Volume 13. pp. 188 – 201.

Kayesa, G. 2005. “Prediction of slope failure at Letlhakane Mine with the Geomos Monitoring System”, *International Symposium on Stability of Rock Slopes in Open Pit Mining and Civil Engineering,* pp. 605 – 622. Available at: One Mine portal: One Mine Digital Library. [Accessed 21 October 2023].

Kolapo, P., Oniyide, G.M., Said, K.O., Lawal, A.I., Onifade, M. and Munemo, P. 2022. An overview of slope failure in mining operations. *Mining, 2.* pp.

350 – 384. Available at: https://www.mdpi.com/journal/mining. [Accessed 21 October 2023].

Kundu, J., Sarkar, K., Singh, A.K. and Singh, T.N. 2020. Continuous functions and a computer application for Rock Mass Rating. *International Journal of Rock Mechanics and Mining Sciences*, Volume 129. pp. 1 – 12.

Leapfrog, 2023. Available at: https://www.seequent.com/products-solutions/leapfrog-geo/. [Accessed 23 October 2023].

Leoni, L., Coli., N., Farina, P., Coppi, F., Michelini, A., Costa, T.A., Costa, T.A.V. and Costa, F. 2015. "The use of ground-based synthetic aperture radar for long-term slope monitoring to support the mine geotechnical team", *FMGM*, pp. 789 – 797. Available at: Australian Centre for Geomechanics. [Accessed 21 October 2023].

Little, M.J. 2005. "Slope monitoring strategy at PPRUST open pit operation", *South African Institute of Mining and Metallurgy. International Symposium on Stability of Rock Slopes in Open Pit Mining and Civil engineering,* pp. 211 – 230. Available at: One Mine portal: One Mine Digital Library. [Accessed 21 October 2023].

Mohtarami, E., Jafari, A. and Amini, M. 2014. Stability analysis of slopes against combined circular – toppling failure. *International Journal of Rock Mechanics and Mining Sciences,* Volume 67. pp. 43 – 56.

Mufundirwa, A., Fujii, Y. and Kodama, J. 2010. A new practical method for prediction of geomechanical failure-time. *International Journal of Rock Mechanics and Mining Sciences,* Volume 47. pp. 1079 – 1090.

Newcomen, W. and Dick, G. 2016. An update to the strain-based approach to pit wall failure prediction, and a justification for slope monitoring. *The Journal of the South African Institute of Mining and Metallurgy,* Volume 116. pp. 379 – 385.

Ockhuizen, G. 2020. Husab Mine Geotechnical Internal report.

Orr, C.M 1992. "Assessment of rock slope stability using the Rock Mass Rating (RMR) system", *The AusIMM Proceedings,* 25 – 29. [online] Available at: <https://www.scribd.com/document/138290897/Assessment-of-Rock-Slope-Stability-Using-the-Rock-Mass-Rating-RMR-System/> [Accessed 21 October 2023].

Ortega, I., Booth, P.W. and Darras, J. 2013. "Stability analysis and remedial design of two road cuttings in North Queensland based on remote geotechnical mapping using digital photogrammetry", *Slope Stability*, pp. 1033 – 1044. Available at: Australian Centre for Geomechanics. [Accessed 21 October 2023].

Osasan, K.S. and Stacey, T.R. 2014. Automatic prediction of time to failure of open pit mine slopes based on radar monitoring and inverse velocity method. *International Journal of Mining Science and Technology,* Volume 24. pp. 275 – 280.

Palmström, A. 1982. “The volumetric joint count – a useful and simple measure of the degree of rock mass jointing”, *Proceedings of the 4th Congress of International Association of Engineering Geology,* pp. 221 – 228.

Park, H. and West, T.R. 2001. Development of a probabilistic approach for rock wedge failure. *Engineering Geology*, Volume 59. pp. 233 – 251.

Raghuvanshi, T.K. 2019. Plane failure in rock slopes – A review on stability techniques. *Journal of King Saud University – Science*, Volume 31. pp. 101 – 109.

Read, J. and Stacey, P. 2009. Guidelines for Open Pit Slope Design. CSIRO Publishing, Collinwood, VIC, Australia, pp. 221.

Rocscience, 2010. Available at: https://www.rocscience.com. [Accessed 23 October 2023].

Rocscience, 2018. Available at: https://www.rocscience.com. [Accessed 23 October 2023].

Rocscience, 2023. Available at: https://www.rocscience.com. [Accessed 23 October 2023].

Sartorelli, L. and Scoular, J. 2022. SkyGeo – InSAR Monitoring Husab Project report.

Shellam, R. and Coggan, J. 2020. “Analysis of velocity and acceleration trends using slope stability radar to identify failure ‘signatures’ to better inform deformation trigger action response plans”, *Slope Stability Symposium*,

pp. 227 – 240. Available at: Australian Centre for Geomechanics. [Accessed 22 October 2023].

Smith, J.V. 2016. A method for assessing discontinuity poles for potential wedge sliding. *Engineering Geology,* Volume 202. pp. 55 – 61.

Sullivan, T.D. 2007. “Hydromechanical Coupling and Pit Slope Movements”, *Slope Stability Symposium,* pp. 1 - 43. Available at*:* Australian Centre for Geomechanics*.* [Accessed 22 October 2023].

Tavakoli, M. and Porter, I. 1994. “Analysis of Rock Mass Classification Systems for Crown Pillar Design”, *AusIMM Student Conference,* pp. 55 – 60. Available at: One Mine portal: One Mine Digital Library. [Accessed 22 October 2023].

Taylor, K., Ghuman, P. and McCardle, K. 2016. “Operational Mine Monitoring with InSAR”, *APSSIM,* pp. 695 – 706. Available at*:* Australian Centre for Geomechanics*.* [Accessed 22 October 2023].

USGS. 2022. Available at: <https://www.usgs.gov/> [Accessed 23 January 2023].

Venter, J., Kuzmanovic, A. and Wessels, S.D.N. 2013. “An evaluation of the CUSUM and inverse velocity methods of failure prediction based on two open pit instabilities in the Pilbara”, *Slope Stability,* pp. 1061 – 1077. Available at: One Mine portal: One Mine Digital Library. [Accessed 22 October 2023].

Zavodni, Z.M. and Broadbent, C.D. 1980. “Slope Failure Kinematics”, *CIM Bulletin,* pp. 69 – 74. Available at: One Mine portal: One Mine Digital Library. [Accessed 22 October 2023].

Zhang, L. 2016. Determination and applications of rock quality designation. *Journal of rock mechanics and geotechnical engineering,* Volume 8. pp. 389 – 397.

Zhang, J., Wang, J.P., Zhang, G.D. and Xue, Y.D. 2020. Probabilistic prediction of slope failure time. *Engineering geology,* Volume 271. pp. 1 – 9.

Zhou, X., Liu, L. and Xu, C. 2020. A modified inverse velocity method for predicting the failure time of landslides. *Engineering Geology*, Volume 268. pp. 1 – 12

APPENDIX A: Scanline Mapping Data

Appendix A: Scanline Mapping Data

Structure	Set number	Dip	Dip-direction	Infill Thickness	Infill Type	Alteration	Micro Roughness	Macro Roughness	Persistence	Min. Spacing	Max. Spacing
Foliation	S1	20	146			Joint surface not altered	Rough undulating	Undulating	>10m	3cm	10cm
Foliation	S2	25	82	<1mm	Non-softenin material - fine	Joint surface altered	Rough undulating	Undulating	50cm	3cm	16cm
Joint	S2	80	59	5mm	Non-softenin material - coarse	Joint surface altered	Rough undulating	Undulating	7m	20cm	30cm
Foliation	S1	40	145	<1mm	Non-softenin material - fine	Joint surface altered	Rough undulating	Undulating	20cm	10cm	25cm
Fault	S2	10	90	20cm	Gouge thickness > greater than amplitude of irregularities	Joint surface altered	Rough undulating	Undulating	14cm		
Joint	S3	82	310	2mm	Non-softening material - medium	Joint surface altered	Rough undulating	Undulating	>10m	40cm	70cm
Joint	S3	75	306	2mm	Non-softening material - medium	Joint surface altered	Rough undulating	Undulating	>10m		
Fault	Random	35	170	10cm	Gouge thickness > greater than amplitude of irregularities	Joint surface altered	Rough undulating	Undulating	5m		
Fault	Random	40	205	5cm	Gouge thickness > greater than amplitude of irregularities	Joint surface altered	Rough undulating	Undulating	7m		
Fault	S2	35	35	20cm	Gouge thickness > greater than amplitude of irregularities	Joint surface altered	Rough undulating	Undulating	>10m		
Joint	S3	20	300	10cm	Gouge thickness > greater than amplitude of irregularities	Joint surface altered	Rough undulating	Undulating	5m	60cm	300cm
Joint	S1	85	108	2mm	Non-softening material - medium	Joint surface altered	Rough undulating	Undulating	1m	7cm	35cm
Fault	S1	65	120	<1mm	Gouge thickness > greater than amplitude of irregularities	Joint surface altered	Rough undulating	Undulating	3m		
Fault	S2	30	70	20cm	Gouge thickness > greater than amplitude of irregularities	Joint surface altered	Rough undulating	Undulating	>10m		
Foliation	S1	55	125			Joint surface altered	Rough undulating	Undulating	30cm	8cm	20cm
Joint	S3	35	300	<1mm	Non-softening material - medium	Joint surface altered	Rough undulating	Undulating	40cm	3cm	30cm

APPENDIX B: Shear Box Test Results

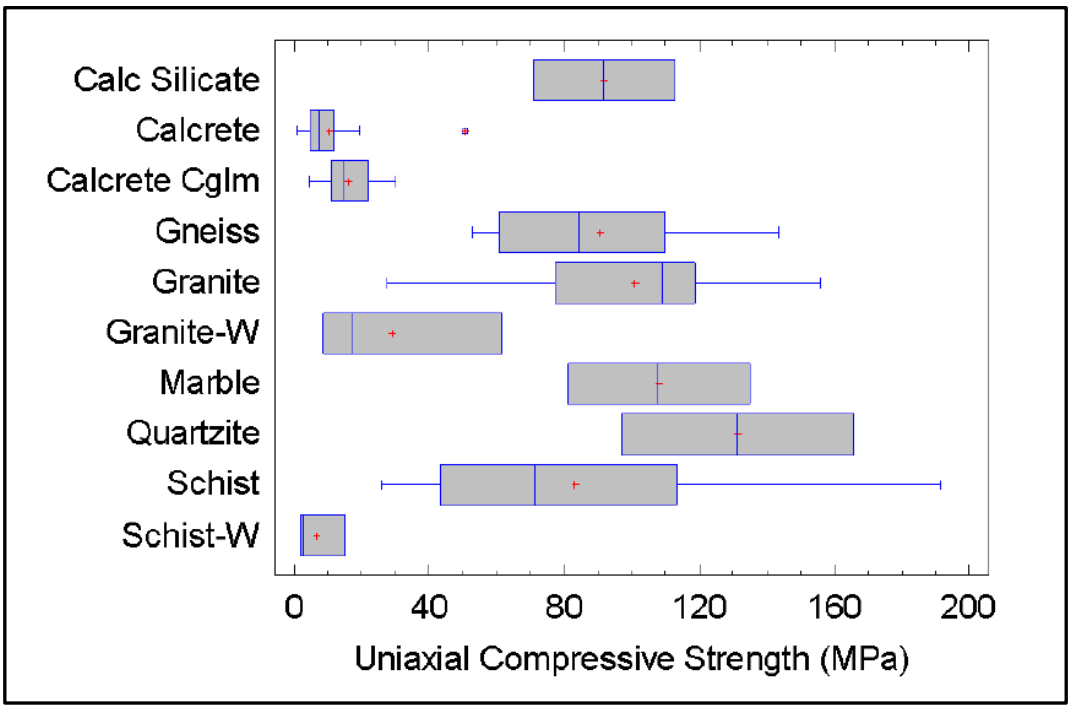
Appendix B: Shear Box Test Results

Client: Swakop Uranium, Namibia — Sampling Site: — 14-07-2022

ROCKLAB Specimen No	Sample ID	Sample Description	Depth From.. m	Depth To.. m	Rock Type	Shear Cycle No	Contact Area mm^2	Shear Force (kN)	Vert. Force (kN)	Dil. Angle (°)	Normal Stress (MPa)	Shear Stress (MPa)	Angle or App Angle (°)	Peak /Residual Friction Angle (°)	Peak /Residual Cohesion (MPa)	Correlation Coefficient	Note
8843-																	
						P1	3544	1.82	1.0	12.6	0.39	0.44	48.5				
						P2	3570	1.94	2.0	8.1	0.63	0.46	36.0	32.0	0.15	0.84	1
SHJO-06	SJM2012	SJM2012_GTDD21-004_41.11m-41.44m_	41.11	41.44	Biotite Schist	P3	3383	2.72	3.0	2.8	0.93	0.76	39.4				
						P1	2106	1.02	1.00	3.8	0.5	0.45	41.8				
						P2	2108	1.47	2.00	2.6	1.0	0.65	33.6	24.0	0.21	1.00	1
SHJO-07	SJM2013	SJM2013_GTDD21-005_85.11m-85.65m	85.11	85.65	Cordierite Schist	P3	1936	1.87	3.00	1.4	1.6	0.93	30.5				
		SJO MULTISTAGE				R1	2069	0.97	1.00	3.3	0.5	0.44	40.7				
						R2	2076	1.42	1.99	2.0	1.0	0.65	33.4	25.0	0.20	1.00	
						R3	1920	1.84	3.00	0.8	1.6	0.94	30.7				
						P1	2869	1.50	1.0	6.3	0.41	0.48	49.9				
						P2	2650	1.52	2.0	-0.2	0.75	0.58	37.4	26.0	0.26	0.96	1
SHJO-08	SJM2014	SJM2014_GTDD21-007_47.49m-47.86m	47.49	47.86	Amphibole Schist	P3	2613	2.16	3.0	0.0	1.15	0.83	35.7				
		SJO MULTISTAGE				R1	2618	0.92	1.0	0.4	0.38	0.35	42.3				
						R2	2638	1.49	2.0	0.3	0.76	0.56	36.5	30.0	0.13	1.00	
						R3	2629	2.08	3.0	-0.1	1.14	0.79	34.9				
						P1	2339	1.36	1.0	-0.7	0.42	0.59	54.4				
						P2	2030	1.75	2.0	2.1	1.02	0.82	39.0	20.0	0.44	1.00	1
SHJO-09	SJM2015	SJM2015_GTDD21-009_21.61m-21.96m	21.61	21.96	Cordierite Gneiss	P3	2017	2.39	3.0	6.2	1.61	1.02	32.4				
		SJO MULTISTAGE				R1	2030	1.01	1.0	1.5	0.51	0.48	43.8				
						R2	2009	1.72	2.0	2.0	1.02	0.82	38.7	26.0	0.27	0.96	
						R3	2012	2.33	3.0	5.4	1.59	1.01	32.5				
						P1	1952	1.57	1.0	-1.8	0.49	0.82	58.9				
						P2	1864	0.98	2.0	-0.4	1.07	0.54	26.6				1
SHJO-14	SJM2020	SJM2020_GTDD21-011_53.57m-55.9_	53.57	55.90	Skarn/calc-silicate	P3	1898	1.81	3.0	-2.6	1.53	1.02	33.7				
		SJO MULTISTAGE				R1	1776	0.80	1.0	0.9	0.57	0.44	37.8				
						R2	1782	1.31	2.0	-2.8	1.09	0.79	36.1	30.0	0.12	0.99	
						R3	1836	1.74	3.0	-3.1	1.58	1.03	33.2				
SHJO-92	SBT4001	SBT4001_GTDD21-001_100.14m-100.33m_STBT	100.14	100.33	Biotite Schist												2
						P1	3086	1.86	1.00	18.0	0.5	0.47	43.8				
						P2	2774	2.70	2.00	16.0	1.0	0.74	37.4	32.0	0.16	1.00	1
SHJO-93	SBT4002	SBT4002_GTDD21-001_102.46m-102.67m_STBT	102.46	102.67	Biotite Schist	P3	2805	3.65	3.00	13.8	1.4	1.01	36.8				
						R1	2747	1.41	1.00	18.9	0.5	0.37	35.6				
						R2	2752	2.64	2.00	13.5	0.9	0.76	39.4	39.0	0.00	0.99	
						R3	2759	3.65	3.00	11.9	1.3	1.04	38.0				
						P1	1738	1.27	1.0	6.7	0.66	0.66	45.1				
						P2	1686	1.38	2.0	0.1	1.19	0.81	34.5	21.0	0.40	0.98	1
SHJO-98	SBT4007	SBT4007_GTDD21-001_110.77m-110.89m_STBT	110.77	110.89	Biotite Schist	P3	1722	1.80	3.0	-0.5	1.73	1.06	31.4				
						R1	1673	1.08	1.0	3.5	0.64	0.61	43.8				
						R2	1680	1.36	2.0	-0.1	1.19	0.81	34.3	25.0	0.30	0.99	
						R3	1703	1.74	3.0	-2.6	1.71	1.10	32.8				
						P1	2916	2.29	1.0	21.3	0.60	0.61	45.2				
						P2	2881	2.97	2.0	16.7	0.96	0.79	39.4	27.0	0.30	1.00	1
SHJO-100	SBT4009	SBT4009_GTDD21-002_92.42m-92.77m_STBT	92.42	92.77	Amphibole Schist	P3	2855	3.62	3.0	13.7	1.32	0.98	36.7				
						R1	2560	1.48	1.0	-6.8	0.32	0.62	62.6				
						R2	2545	2.26	2.0	1.3	0.81	0.87	47.3	29.0	0.43	1.00	
						R3	2552	3.10	3.0	3.8	1.25	1.14	42.2				

APPENDIX C: Fresh Rock Geotechnical Parameters Part A

Appendix C: Fresh Rock Geotechnical Parameters Part A



APPENDIX D: Fresh Rock Geotechnical Parameters Part B

Appendix D: Fresh Rock Geotechnical Parameters Part B

Table 22: Fresh Rock Geotechnical Parameters used for Slope Stability

Parameter	Std. Dev.	Mean	Lower Bound	Upper Bound
UCS (MPa)	40	93	26	191
Elastic Modulus for Intact Rock (MPa)	55430			
Poisson's Ratio	0.3			
GSI	9	75	36	94
m_i	11	23	10	32
Unit Weight (kN/m^3)	26.7			
JRC	5.4	9.6	1.5	20
Base Friction Angle (from field data)	2.47	37.6	34	45

APPENDIX E: 2017 study and Feasibility UCS lab test results (SRK Part A)

Appendix E: 2017 study and Feasibility UCS lab test results (SRK Part A)

	No	Lithology	Rock Type	Depth	UCS (Mpa	
Feasibility Study	62	Rossing	Granite	188.2	101.4	
	63		Granite	258.6	127.9	
	64		Marble	124.9	81	
	65		Calc Silicate	155.2	112.9	
	66		Schist	144.6	113.2	
	67		Granite	62.8	63.4	
	68		Marble	57.4	134.9	
	69		Granite (weathered)	53.6	17.2	
	70		Schist	108.7	38.6	
	71		Gneiss	82.2	84.4	
	72		Schist	78.0	71.4	
	73		Granite	126.0	68.7	
	74		Weathered Schist	98.3	15	
	75		Quartzite	122.2	166	
	76		Weathered Granite	138.1	61.5	
	77		Gneiss	162.2	125.5	
	78		Schist	183.7	38.7	
	79		Granite	198.9	82	
	80		Schist	202.5	25.6	
	81		Schist	203.8		
	82		Gneiss	206.6	56.4	
	83		Granite	280.8	86.9	
2017 Study	1	Rossing	Schist	160.0	129.8	
	2		Weathered Schist	22.8	34.8	
	3		Marble	57.8	90.5	
	4		Calc Silicate	342.6	172.0	
	5		Leucogranite	297.1	148.5	
	6		Cordierite Gneiss	136.2	153.5	
	7		Calc Silicate	149.2	21.8	
	8		Marble	260.2	140.4	
	9		Mottled Gneiss	310.7	54.9	
	10		Mottled Gneiss	311.1	70.8	
	11		Schist	195.0	200.1	Biotite Sch
	12		Leucogranite	190.5	276.6	
	13		Marble	271.7	123.4	
	14		Schist	117.8	170.0	Biotite sch
	15		Calc Silicate	168.2	72.8	
	16		Marble	234.6	22.4	
	17		Marble	235.2	73.8	
	18		Gneiss	240.6	129.0	
	19		Gneiss	55.2	18.2	
	20		Calc Silicate	126.3	190.1	
	21		Gneiss	76.2	12.7	
	22		Cordierite Gneiss	93.6	150.6	
	23		Cordierite Gneiss	94.6	140.0	
	24		Schist	203.8	123.7	Biotite Sch

APPENDIX F: 2017 study and Feasibility UCS lab test results (SRK Part B)

Appendix F: 2017 study and Feasibility UCS lab test results (SRK Part B)

	No	Lithology	Rock Type	Depth	UCS (Mpa)
Feasibility Study	62	Rossing	Granite	188.2	101.4
	63		Granite	258.6	127.9
	64		Marble	124.9	81
	65		Calc Silicate	155.2	112.9
	66		Schist	144.6	113.2
	67		Granite	62.8	63.4
	68		Marble	57.4	134.9
	69		Granite (weathered)	53.6	17.2
	70		Schist	108.7	38.6
	71		Gneiss	82.2	84.4
	72		Schist	78.0	71.4
	73		Granite	126.0	68.7
	74		Weathered Schist	98.3	15
	75		Quartzite	122.2	166
	76		Weathered Granite	138.1	61.5
	77		Gneiss	162.2	125.5
	78		Schist	183.7	38.7
	79		Granite	198.9	82
	80		Schist	202.5	25.6
	81		Schist	203.8	
	82		Gneiss	206.6	56.4
	83		Granite	280.8	86.9
2017 Study	1	Rossing	Schist	160.0	129.8
	2		Weathered Schist	22.8	34.8

APPENDIX G: 2017 study and Feasibility UCS lab test results (SRK Part C)

Appendix G: 2017 study and Feasibility UCS lab test results (SRK Part C)

	3		Marble	57.8	90.5	
	4		Calc Silicate	342.6	172.0	
	5		Leucogranite	297.1	148.5	
	6		Cordierite Gneiss	136.2	153.5	
	7		Calc Silicate	149.2	21.8	
	8		Marble	260.2	140.4	
	9		Mottled Gneiss	310.7	54.9	
	10		Mottled Gneiss	311.1	70.8	
	11		Schist	195.0	200.1	Biotite Schist
	12		Leucogranite	190.5	276.6	
	13		Marble	271.7	123.4	
	14		Schist	117.8	170.0	Biotite schist-Chuos Diamictite
	15		Calc Silicate	168.2	72.8	
	16		Marble	234.6	22.4	
	17		Marble	235.2	73.8	
	18		Gneiss	240.6	129.0	
	19		Gneiss	55.2	18.2	
	20		Calc Silicate	126.3	190.1	
	21		Gneiss	76.2	12.7	
	22		Cordierite Gneiss	93.6	150.6	
	23		Cordierite Gneiss	94.6	140.0	
	24		Schist	203.8	123.7	Biotite Schist

Appendix H: InSAR Monitoring Data (November 2020 Failure)

pnt_id	pnt_flags	Velocity
L00002928P00014001	11	0.00196
L00002928P00014002	11	0.00428
L00002928P00014011	11	0.00051
L00002928P00014012	11	0.00761
L00002929P00013992	101	0.00062
L00002929P00013999	11	0.00089
L00002929P00014000	11	0.00049
L00002929P00014001	11	0.00332
L00002929P00014002	11	0.00151
L00002929P00014003	11	0.00083
L00002929P00014004	11	0.00064
L00002929P00014005	11	0.00147
L00002929P00014010	101	0.00831
L00002929P00014011	11	0.00651
L00002929P00014015	101	0.00504
L00002930P00014004	11	0.00069
L00002930P00014009	101	0.00742
L00002930P00014010	101	0.00784
L00002930P00014016	101	0.00567
L00002926P00013981	11	0.00323
L00002926P00013985	11	0.0001
L00002926P00013986	11	0.00142
L00002926P00013987	11	0.00138
L00002926P00013988	11	0.001
L00002926P00013989	11	0.00401
L00002926P00013991	11	0.00031
L00002926P00013994	11	0.00281
L00002926P00013995	11	0.00067
L00002926P00013996	11	0.00107
L00002926P00014003	11	0.00677
L00002927P00013975	11	0.00796
L00002927P00013978	11	0.00054
L00002927P00013979	11	0.0004
L00002927P00013980	11	0.00014
L00002927P00013981	11	0.0008
L00002927P00013982	11	0.00067
L00002927P00013983	11	0.00116